Computational Mechanics /

Transfer Moulding of Reactive Materials: Application to Encapsulation of Integrated Circuits

A.B. Spoelstra

Transfer Moulding of Reactive Materials:

Application to Encapsulation of

Integrated Circuits

A.B. Spoelstra

Computational Mechanics /

Department of Engineering Fundamentals

Centre for Polymers and Composites

Eindhoven University of Technology

August 1992

(WFW 92.098)

This work was supervised by:
Prof.Dr.Ir. H.E.H. Meijer
Dr.Ir. G.W.M. Peters

Content

Summary

The reactive flow of a highly filled epoxy moulding compound has been studied using a combination of experiments and numerical analyses. This study serves the development of a technology that allows for IC-packaging with two or more components, in order to obtain a multilayer encapsulation. The predictive capacity of the numerical model is tested by comparing calculated and measured deformation patterns in a piston driven flow. Experimental visualisation of the deformation patterns was realised by using different coloured slices of the same material. For the numerical simulation the finite element method is used that includes a particle tracking algorithm, enabling a direct confrontation of numerical results with the visualisation experiments. Since an adequate description of the chemorheological behaviour of the encapsulant proves to be of the utmost importance with respect to the predictive capability of the numerical simulations, a considerable part of this study is dedicated to material characterization.

The reaction kinetics of epoxy compounds is studied with Differential Scanning Calorimetry. It appears that the kinetics can be described with a simple autocatalytic equation.
Since it is impossible to measure steady state viscosities on these compounds, the dynamic viscosity is measured with a Dynamic Mechanical Thermal Analyzer at different frequencies, strains and heating rates. Using the kinetic equation, the conversion during the rheological measurements is obtained. It is shown that at a constant value of the effective shear rate, i.e. the product of frequency and strain, the dynamic viscosity is identical over a wide range of values for the strain and frequency. The effective shear rate dependence can be described by a powerlaw with an exponent that depends on the conversion. The effect of temperature on the dynamic viscosity is of an Arrhenius-type with conversion dependent parameters. The steady state viscosity used in the numerical analyses is assumed to be equal to the dynamic viscosity for shear rates equal to the effective shear rates.
The gel point is determined through extraction experiments, and could not be detected in dynamic rheological analyses.

Numerical simulations of the piston driven flow, in which the material parameters obtained in this study are used, are in qualitative agreement with the visualisation experiments. It appears that the shearthinning behaviour, determined by dynamic rheological experiments, is too strong. The definition of a rheological gel point, lower than the chemically determined gel point, lead to a more quantitative

description of the flow. Finally, visualisation experiments of a practical two cavity encapsulation process show an asymmetric filling of the cavities. An improved geometry for a better controlled process is designed and evaluated.

1 The Encapsulation of Integrated Circuits

1.1 Introduction

This study serves the development of a technology that allows for IC-packaging with two components, in order to obtain a multilayer encapsulation. An integrated circuit (IC), also called chip, is a collection of transistors, diodes, resistors and capacitors. They are all fabricated within silicon material on micron scale. To accomplish this feat of miniaturization, rigorous regimens of cleanliness must be maintained in the IC fabrication areas. Each chip must be interconnected with other components and be allowed to communicate with the outside world. To accomplish this the fabricated integrated circuit is packaged[1]. First the chip is attached to a carrier, generally a leadframe stamped from a metal sheet. Then the bonding pads on the chip are connected with contact points on the leadframe with thin, generally gold wires. The final step in the packaging process is the encapsulation of the electronic device. In *Figure 1.1* a schematic side view is given of a packaged chip.
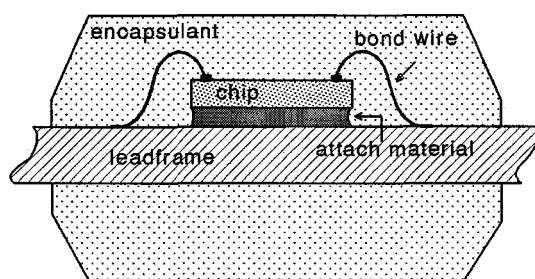
Figure 1.1   Schematic side view of a packaged chip.

The encapsulant is for the protection of the integrated circuit and wire bonds from contamination and moisture penetration. It has to provide a balanced combination of properties in the areas of mechanical strength, chemical resistance, electric and dielectric insulating performance, thermal conductivity, and thermal and moisture stability in the general temperature range of -65 to 200 °C. In special industrial applications and in military uses, ceramics or metal cans are applied, since high performance and hermeticity are required and cost is of minor importance. Although the moisture permeation properties of plastics are poor, they have the

advantage of low cost, low weight and cheap manufacture costs (transfer moulding). About 90% of all integrated circuits produced are encapsulated in a plastic enclosure.[2, 3] This study will be focused on the plastic encapsulation of integrated circuits.

Trends in the IC-technology towards larger IC's encapsulated in smaller packages increase the risk of mechanical failures during processing, testing and use. Especially failures caused by the severe mismatch in the thermal expansion coefficients between the silicon chip/leadframe and the encapsulation material become more frequent. Furthermore interfacial adhesion is critical, as delamination at the material interface creates additional moisture penetration pathways.[3, 4, 5] A lot of research has been aimed at the improvement of these properties of the encapsulating material.[1, 3, 6] Since it proves difficult to combine all properties required in one material, it would be convenient to encapsulate the chip with two or more different materials. For example a chip surrounded by a low modulus material could reduce stresses, while a second material on the outside could provide mechanical strength. Another interesting possibility is to use an inner material with excellent adhesion properties[5], while the outside material still releases from the mould. Since the number of chip handling steps during packaging should be minimized, a one step multilayer transfer moulding process would be the best solution.

In this chapter, a brief description of the composition of a common encapsulation material is given (section 1.2), the transfer moulding process is explained (section 1.3) and the scope of this study will be outlined (section 1.4).

1.2 Encapsulant Materials

Evaluating various types of polymers for use as an encapsulant, epoxy resins satisfy the requirements best and are therefore almost universal accepted as the preferred plastic encapsulation material. The epoxy moulding compounds are usually composed of more than ten kinds of raw materials[6], each of which has its own special functions. Important characteristics to consider are mouldability, mechanical and electrical properties, and humidity and heat resistance. These depend significantly on the characteristics of the epoxy resin used. In addition to the resin and the hardener, the epoxy moulding compound usually contains a catalyst, fillers, flame retardants, colorants and a mould release agent. For specific applications other additives may be added.

Epoxies can be classified by their cure-mechanism. Amine-cured epoxies are fast curing and have a superior shelf-life, but unfortunately have very poor moisture performance and poor electrical characteristics. Anhydride-cured epoxies have, due to their ester linkages a good thermal stability, but are hydrolysed easily, resulting in a poor storage stability. Ether linkages are formed using a novolac hardener. They show less temperature stability than the ester linkages, but have superior moisture resistance. Furthermore the residual ionic contamination level is lower for systems using a phenolic curing agent than for anhydride or amine cured systems. These resins are therefore applied most in encapsulant materials.
The catalyst system has to meet the contradictory requirements of long shelf life and fast curing at moulding[6].

Fillers are added in the range of 60 to 75 wt% not only to reduce cost but mainly to improve physical and mechanical properties. Major properties influenced by the amount and type of filler are the thermal expansion coefficient, thermal conductivity and the elastic modulus. Crystalline silica powders or quartz (fused silica) powders are most widely used.
To improve the flame-retarding characteristics of the encapsulant, a combination of antimony oxide with a halogen-containing ingredient is added. Usually a antimony oxide / brominated epoxy resin is used as a flame-retardant[3, 6]. A colorant, generally carbon black, is added to prevent light transmission since many electronic devices are photosensitive. The amount and type of mould release agents has to be carefully chosen since they affect the adhesion between the encapsulation material and leadframe / IC as well. Other additives may include coupling agents to improve adhesion between the filler system and the resin, rubber particles to improve toughness and special additives for an application-specific reason.

1.3 The Transfer Moulding Process

The most common method of large scale encapsulation of electronic devices is transfer moulding. Transfer moulding is a variant of compression moulding in which the plastic material is first melted in a heated cylinder or "pot" and then transferred to a mould cavity and compressed in the desired shape. The process differs from compression moulding, since the molten material is forced into a closed mould. This improved flow makes the moulding of complex and fragile parts possible and reduces cycle times. Furthermore by preheating the material in a separate chamber the pins and inserts in the mould are not subjected to the direct pressure of the press ram[7].

The transfer moulding process of integrated circuits can be described as follows[8,9]. First the moulding compound is pressed into a preform, that in some cases is preheated in a dielectric heater. Accordingly the preform is loaded into the cylindrical chamber, or "pot", and the leadframe carrying the integrated circuit is placed in the mould. The load is then forced through the runners and gates into the cavities of the mould by means of a plunger. *Figure 1.2* shows a schematic diagram of a transfer press (side view). Mould temperatures are usually in the order of 160 to 180°C. Due to the high temperature in the mould, the compound will react and crosslink. After the mould is filled, the pressure is increased and the moulding compound is packed and further polymerized. Discharging the moulded article in a fully automatic process is commonly supported by ejector pins. Typical moulding times are on the order of 5 or 6 minutes. After the parts are demoulded they are postcured for about 4 hours at around 170 °C.
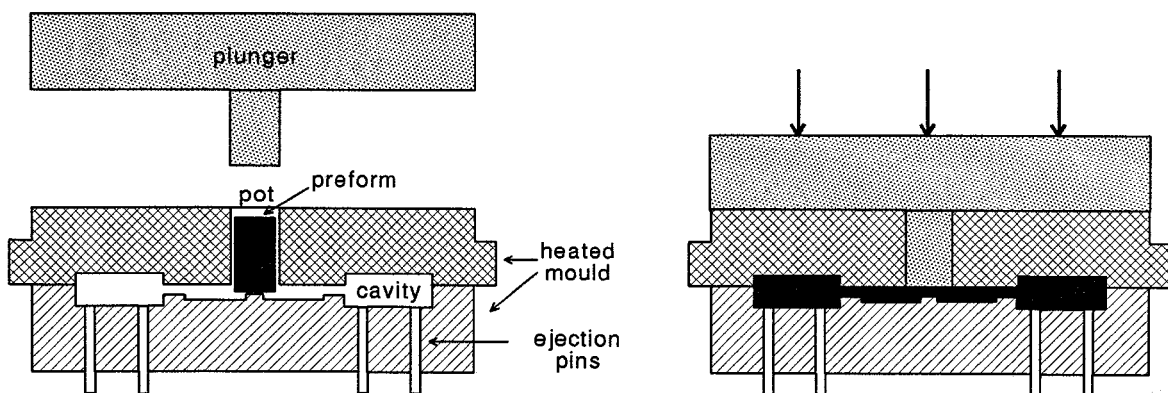
Figure 1.2   Schematic diagram of the transfer moulding press (side view).

The conventional moulds for the encapsulation of integrated circuits use a multicavity concept. One large transfer pot is used to supply the material for more than typically 50 cavities. This geometry results in a filling profile that is not uniform (Figure 1.3) since the pressure gradients are higher closer to the transfer pot.

More recently the multiplunger concept is designed in which one mould is equipped with several pots served by the corresponding number of plunger (Figure 1.4). Eliminating the long conventional runners, a more uniform filling pattern can be achieved while reducing cycle times [10]. Since in this concept each transfer pot is supplied by a relative small amount of material, dielectric preheating is no longer needed, thus eliminating an extra step in the encapsulation process.

Typical moulding problems encountered during the IC encapsulation moulding process are [9]: incomplete mould filling (short shots), leadframe movement during cavity filling and wire sweep. These three moulding problems are directly related to processing conditions and the chemorheological characteristics of the moulding compound used for encapsulation. The case of incomplete mould filling is caused by too fast an increase in viscosity relative to the filling speed, leading to gelation of the moulding compound before the mould is filled. In a multicavity mould this problem is more difficult to overcome since long runners are applied. The second problem, leadframe movement during cavity filling, is due to forces on the leads caused by unequal fluid fronts above and below the leadframe and is capable of causing damage. A proper design of the mould and especially the leadframe can balance the flows.

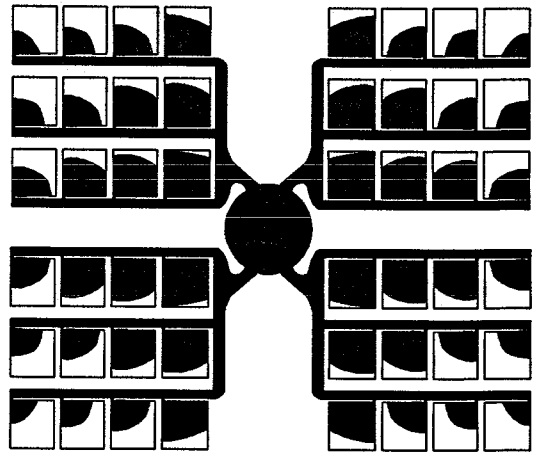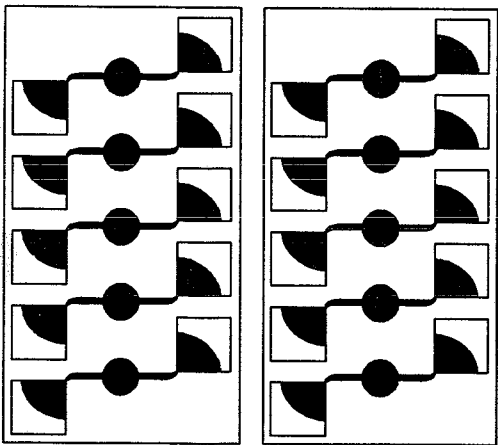Figure 1.3. A partially filled multicavity mould.

Figure 1.4. A partially filled multiplunger mould.

Movement of the fine wires electrically connecting the integrated circuit to the leadframe is commonly referred to as wire sweep. During the filling stage, the flow front of the resin entering the mould cavity possesses sufficient momentum to displace the wires and can cause adjacent wires to contact and short the device[10]. Close control of the transfer ram speed is crucial to avoid wire sweep and jetting. On the one hand slow filling translates into pushing a resin in advanced state of cure into the cavity causing wire sweep. On the other hand high filling speeds can damage the wires as well.

All these defects can be minimized with the proper mould, leadframe and wire design, moulding resin and process parameters.

Failure of encapsulated devices can also occur after the moulding process. A main failure mechanism is corrosion due to ingress of moisture[1]. Moisture can reach the die surface by permeation through bulk, by penetration along the compound / leadframe interface or through cracks in the package.

Internal stresses are also an important failure in encapsulated devices, not only through direct mechanical damage, but also by promoting corrosion by moisture[4,5,11]. Stresses are created mainly during cooling from the curing temperature to room temperature and due to the mismatch between thermal expansion coefficients during use at different temperature of the surroundings. Compared to these stresses, stresses formed during curing at the mould temperature due to shrinkage are unimportant[4]. The main variables that affect the stresses are: differential thermal expansion coefficients of the moulding compound and the integrated circuit, difference in their moduli, difference between use temperature and curing temperature, and size of the chip.

Since the difference in the coefficients of thermal expansion of the encapsulant, the leadframe and the chip is the most important source of internal stresses, a lot of effort has been devoted to lower the expansion coefficient of the moulding compound[3, 6] in order to make it closer to that of the chip and the leadframe. On the other hand, simulations of the internal stress situation during e.g. temperature cycle tests, indicate that a shear stress at the interface between chip or leadframe and encapsulant can decrease the absolute level of the maximum stresses considerably[5,12]. Improved adhesion is easily obtained by removing of the release agent, however the demoulding will be more cumbersome.

In summary, the processing parameters have little influence on the failures occurring after moulding. To minimize these failures, the encapsulation materials have to be improved by making them less permeable to moisture, by improving the adhesion to the leadframe, and by matching the thermal expansion coefficient and the modulus of the moulding compound to those of the chip and leadframe. As

mentioned in section 1.1, the design of a multilayer transfer moulding process in which different materials can be used to encapsulate the integrated circuit could be a development to conquer these problems. For such a process it is necessary to be able to predict how these materials should be distributed in the transfer pot in order to obtain the defined configuration in the mould.

1.4 Scope of this Study

The aim of this work is to examine the predictive capability of numerical tools for the simulation of reactive flow of a epoxy moulding compound used in the encapsulation of integrated circuits, by using a combination of experiments and numerical analyses. This study serves the development of a technology that allows. for IC-packaging with two or more components, in order to obtain a multilayer encapsulation.

Since an adequate description of the chemorheological behaviour of the encapsulant proves to be of the utmost importance, chapter 2 is dedicated to the characterization of the material. The reaction kinetics are studied and a description is obtained for the viscosity as a function of temperature, shear rate and conversion.

In chapter 3 the reactive flow of this material is studied in different geometries. First a piston driven flow is considered by experiments as well as numerical analyses. Experimental visualisation was done using different coloured slices of the same material. The predictive capacity of the numerical model is tested by comparing calculated and measured deformation patterns. For the numerical simulation the finite element method is used which includes a particle tracking algorithm, enabling a direct confrontation with the visualisation experiments.
Furthermore, in order to trace unforseen problems and find out if a reproducible and controllable flow is possible, the reactive flow is studied in a practical two cavity mould by visualisation experiments. From this an improved design is suggested and evaluated.

Finally, conclusions and suggestions for further research on this subject are summarized in chapter 4.

Figure 2.1   The chemical structures of the resins and the hardener.
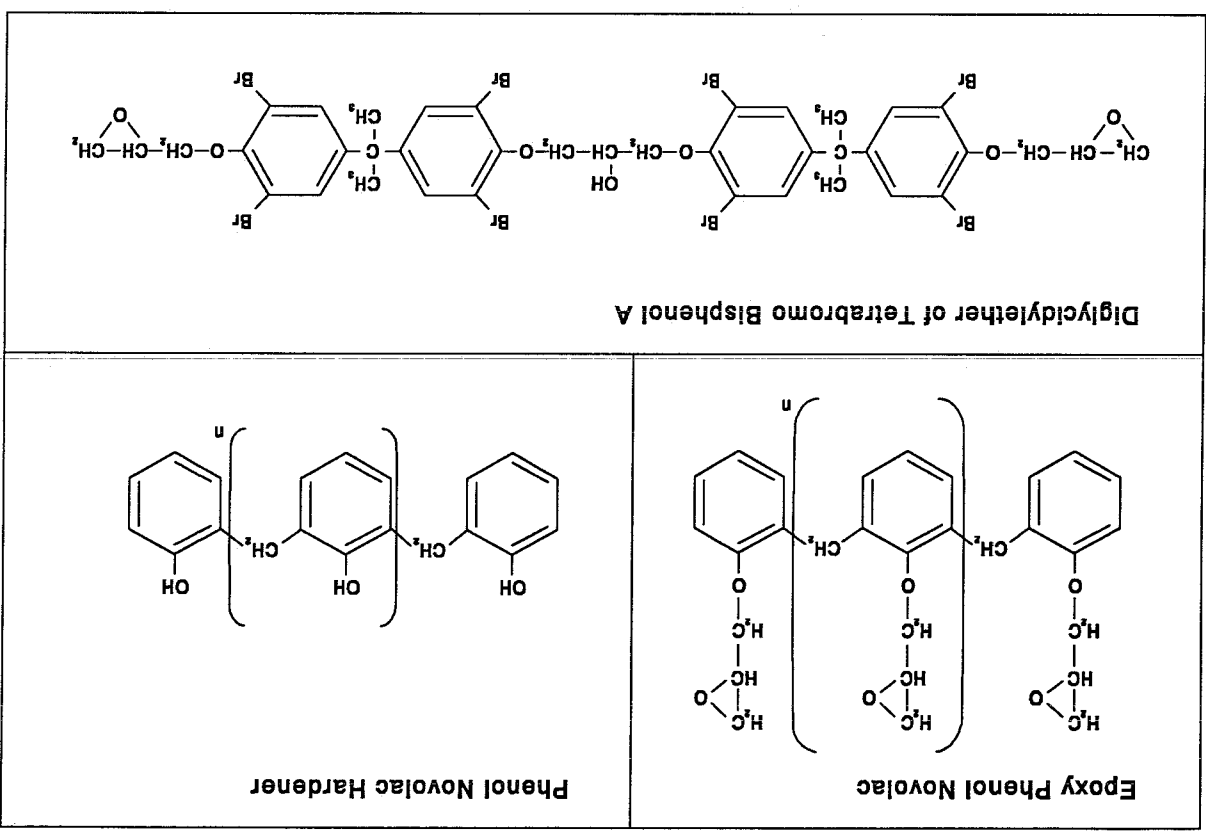
2 Material Characterization

In this chapter the most important material properties with respect to reactive flow modelling are characterized. After a description of the materials used (section 2.1), an outline is given how the parameters of the kinetic equation for the curing reaction is obtained, by means of Differential Scanning Calorimetry (DSC) in section 2.2. From these experiments also the heat of reaction is obtained, necessary in the modelling as the reaction provides an extra heat source in the energy equation.

Dynamic Mechanical Thermal Analysis (DMTA) experiments are discussed in section 2.3. Combination of these experiments with the DSC results leads to a description of the dynamic viscosity as a function of temperature, frequency, strain and conversion. These results are transformed into a description of the steady state viscosity as a function of temperature, shear rate and conversion. In section 2.4 the gel point is studied through extraction of samples with a different degree of cure and by examining the viscoelastic properties during cure. In section 2.5 the thermal conductivity and the heat capacity of the compound are examined.

2.1 Materials

The epoxy compound chosen for this study is a fast-curing compound, supplied by Synres-Almoco, based on a phenol novolac epoxy and hardener. A diglycidylether of tetra bromo bisphenol A is added to improve the fire-resistance properties. In *Figure 2.1* the chemical structures of these resins are given. The compound is filled with a combination of crushed silica and quartz for 69 wt%, resulting in a solid volume content of ± 50 %. Further it contains release agents, carbon black and other common additives. From the supplier a second compound is obtained with an identical composition of the first, except no carbon black is added. Thus, a black and a white compound are available, to be used in the visualisation experiments.

2.2 Reaction Kinetics

2.2.1 Strategy

For the cure reaction of thermosets, various rate expressions have been proposed in literature . To account for the autocatalytic curing of thermosets[13, 14, 15] , Kamal and Sourour[16] suggested the following expression:

$$\dot{\alpha} = \frac{d\alpha}{dt} = (K_1 + K_2 \alpha^m)(1-\alpha)^n \qquad (2\text{-}1)$$

in which n and m represent reaction orders. The rate constants K_1 and K_2 depend on the temperature according to the Arrhenius equation:

$$K_1 = k_1 \exp(\frac{-\Delta E_1}{RT}) \quad , \quad K_2 = k_2 \exp(\frac{-\Delta E_2}{RT}) \qquad (2\text{-}2)$$

where k_1 and k_2 are the pre-exponential factors, ΔE_1 and ΔE_2 are the activation energies, R is the gas constant and T is the temperature in K.

For kinetic studies by means of Differential Scanning Calorimetry (DSC), it is usually assumed that the heat of reaction is proportional to the conversion of the reactants, which implies that the total heat produced at total cure is constant. The reaction rate can easily be calculated from calorimetry measurements with:

$$\dot{\alpha} = \frac{d\alpha}{dt} = \frac{1}{\Delta H} \frac{dH}{dt} \qquad (2\text{-}3)$$

where $\dot{\alpha}$ is the rate of reaction, α is the conversion, ΔH is the total heat production at complete cure and dH/dt is the differential heat flow during cure.

To study the cure kinetics by means of DSC, measurements can be conducted under isothermal (time-sweep) or dynamic (temperature-scan) modes[17]. For fast curing thermosets isothermal experiments are inadequate. Therefore, in this study dynamic experiments are performed at different heating rates. By integration of *Equation 3* over the total cure-time, the heat of reaction (ΔH) is determined. The fractional conversion $\alpha(\tau)$ is likewise calculated by integrating from t=0 to t=τ. In our analysis the trapezium-rule is used for numerical integration. For each heating rate a set of data is obtained, containing T, α and $\dot{\alpha}$.

The kinetic parameters k_1, k_2, ΔE_1, ΔE_2, n and m can be determined by fitting $\dot{\alpha}$ to

the autocatalytic function *(Eq. 1)* of α and T by a non-linear least squares program. All results of the dynamic experiments are fitted simultaneously. First the data are fitted to a simple n^{th}-order reaction ($k_2 = 0$). Accordingly, the results are used to initiate the program to fit to the autocatalytic expression.

With the kinetic equation obtained, it is possible to predict reaction rate and conversion for any temperature-history by numerical integration. In our analysis a 2nd-order Runge-Kutta integration method is used.

2.2.2   Experimental

DSC-measurements are carried out in a Perkin-Elmer DSC-7. Calibration of the calorimeter is conducted for each run, using indium (temperature, enthalpy) and zinc (temperature). Each sample contained 5-7 mg of compound sealed in a sample pan. Measurements at constant heating rate are performed at 5, 10, 20 and 40 °C/min, in a temperature range of 50 to 250 °C.

2.1.3   Results and Discussion

The heat of reaction for the black compound is directly determined by integration of the exothermal peaks from the DSC-measurements shown in *Figure 2.2* and is found to be 60 J/g.

The conversion, calculated according to the method discussed above, is shown in *Figure 2.3*. For each heating rate, a reduced dataset is used to fit the kinetic equation. In *Table I* the final results of the fit are summarised. Since m and n are no integers it is very likely that all variables represent an average of a number of different reactions.

With the kinetic variables obtained, the kinetic data are recalculated to check the fit, with satisfactory results *(Figure 2.4)*. In *Figure 2.5* the reaction rate measured on the white compound is compared to recalculations, based on measurements performed on the black compound, showing that despite the absence of carbon black, the reaction kinetics can be considered equal.

Table I. Kinetic parameters.

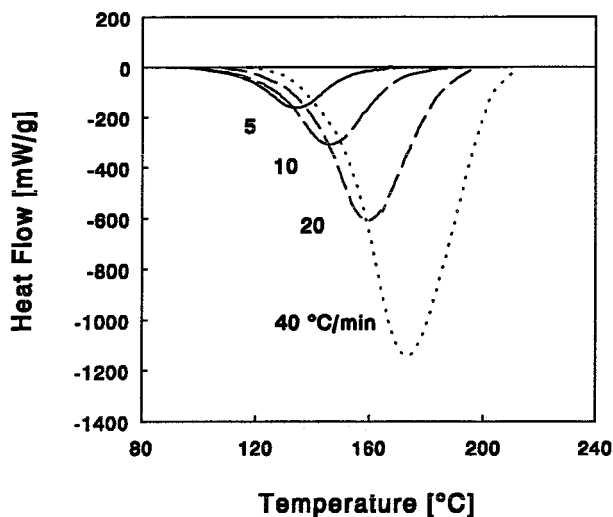| k_1 $= 6.84*10^5$ s^{-1}	k_2 $= 1.60*10^7$ s^{-1}
ΔE_1 $= 102$ kJ/mol	ΔE_2 $= 72.4$ kJ/mol
n $= 1.09$	m $= 0.45$

2-3

Figure 2.2 Heat flow measured by DSC during cure at constant heating rate: 5, 10, 20 and 40°C/min.
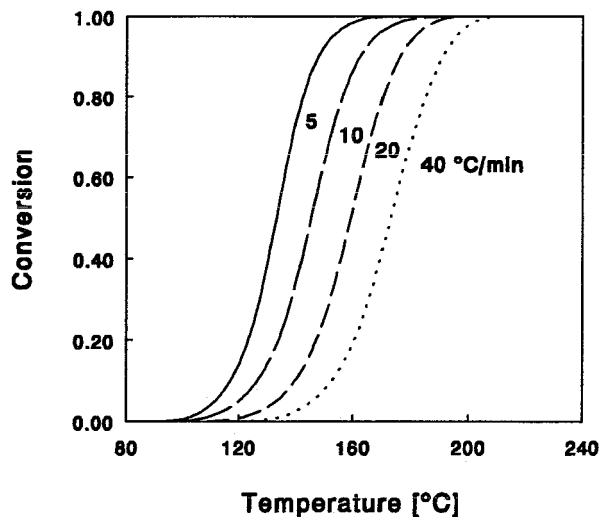
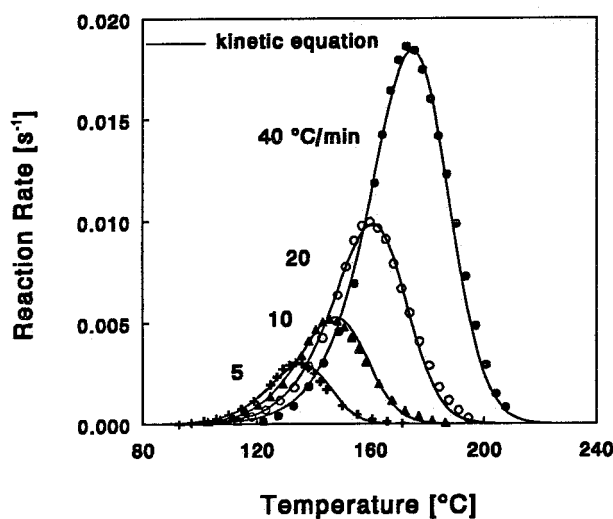*Figure 2.3* Calculated conversion at constant heating rate: 5, 10, 20 and 40 °C/min.

Figure 2.4 Experimental data (symbols) and recalculated reaction rate (full line); heating rates: 5, 10, 20 and 40 °C/min.
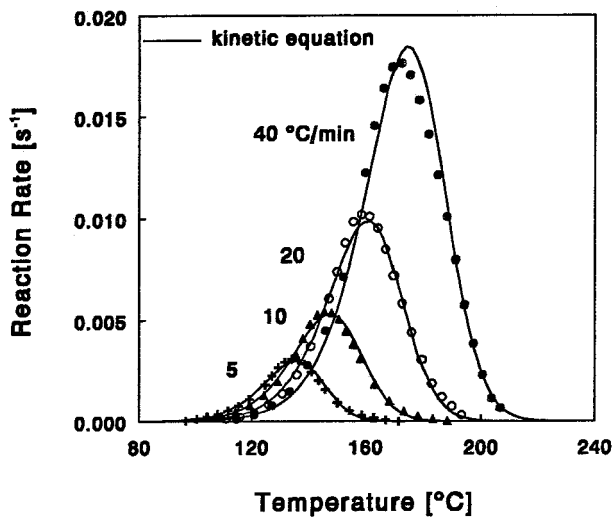
Figure 2.5 Experimental data of the compound without carbon black compared to recalculated reaction rate obtained from experiments performed on the compound with carbon black (full line); heating rates: 5, 10, 20 and 40°C/min.

2-4

2.3 Rheology

For mathematical modelling of thermoset processing one needs, apart from the reaction kinetics and the heat of reaction a constitutive equation for the description of the flow behaviour. The epoxy compound is modelled as a generalized Newtonian fluid and therefore an expression for the viscosity during cure must be determined. In the literature only limited information can be found concerning the effect of curing on viscosity of highly filled epoxy compounds. In this section a strategy is proposed to find an expression relating viscosity to temperature, shear rate and degree of reaction.

2.3.1 Strategy

A problem with highly filled, fast curing compounds, is the difficulty to measure steady state viscosities. Capillary viscometry is not possible for different reasons. The most important one is that this method requires the same material all over the capillary tube which is not fulfilled due to time and place dependent cure. For rotational viscometers, due to the paste-like behaviour of highly filled compounds, the sample will curl up during a steady state experiment. As a consequence, in this study the dynamic viscosity (η_d), with deformations restricted to small amplitude oscillations, is measured instead of the steady state viscosity (η_s).
To develop a proper viscosity model for flow simulations it is necessary to translate the measured dynamic viscosities to steady state viscosities.

For some unfilled thermosets the Cox-Merz rule[18] is reported to apply for conversions below the gel point[19]:

$$\eta_d(\omega) = \eta_s(\dot{\gamma} = \omega) \qquad (2\text{-}4)$$

In the literature a lot of research has been aimed at the validation of this law for filled systems. Kitano[20] observed however, that for polyethylene and polypropylene melts filled with various solid particles, Cox-Merz failed when solid volume fractions were greater than 0.1 to 0.2. The dynamic viscosity measured at frequency ω is lower than the steady state viscosity measured at a shear rate $\dot{\gamma} = \omega$. Applying Cox-Merz would result in a more shearthinning behaviour. This result is supported by Bigg[21] who reported that even at low strains dense suspensions exhibit a large strain dependency.
A constitutive relation for highly filled dispersions, a model with a yield stress

described by Hookean behaviour below, and by a Herschel-Bulkley relation above the critical stress, was reported by Doraiswamy[22] who studied a 70 vol% suspension of silicon in polyethylene. Independently, van den Brule[23] proposed three similar but more general constitutive relations with a yield stress in it. One of the results of this type of constitutive models is that the dynamic viscosity at different strain levels may be made to superimpose if plotted against an effective shear rate defined as the product of frequency (ω) and maximum strain (γ_0). Furthermore, an equivalence between the steady state viscosity and the dynamic viscosity is predicted as follows:

$$\eta_s(\dot{\gamma}) = \eta_d(\omega\gamma_0) \qquad (2\text{-}5)$$

Experimental results which support this prediction are only available at low shear rates[22]. In this study it is however assumed that *Equation 2.5* can be applied, in the region of interest for process modelling, i.e. the region between melting and gelation of the epoxy compound, and therefore the dynamic viscosity will be modelled as a function of effective shear rate, temperature and conversion.

Early chemorheological models, reported in the literature, related viscosity (η) to time (t) and temperature (T), but could only predict viscosity under isothermal conditions[19]. Later models[24, 25] transformed these equations into an integral formulation, allowing the whole temperature history to be taken into account. No knowledge about, or control over, the conversion (α) as a function of time (t) is assumed. Using independently measured kinetic data, $\eta(t)$ can be converted into $\eta(\alpha)$. Macosko and coworkers[26, 27, 28] reported a molecular model, using the branching theory, which relates the conversion to the molecular weight (M_w). These molecular models can only be used when sufficient information is available about the actual reactions which occur during cure.

Unfortunately, commercial moulding compounds contain several epoxies and hardeners, and a high content of various additives that might affect the reactions. Therefore, a model based on a molecular analyses is often found to be impossible.

Another class of models relates viscosity directly to epoxy conversion[28, 29, 30]. In these models an Arrhenius temperature dependency is assumed with two adjustable parameters. They differ in their treatment of the curing dependency but all assume that this dependency can be separated from the temperature dependency. Furthermore these models do not include a shear rate dependency. For filled systems however, pronounced shearthinning has been observed[27].

The non-linear behaviour of the viscosity as a function of the shear rate is often described by means of a powerlaw. We used an identical expression to model the effective shear rate dependence. Temperature dependence is often described by an Arrhenius-equation. Therefore the following expression for the dynamic viscosity is adopted:

$$\eta(T, \omega\gamma_0) = \eta_0 \; e^{E_\eta/RT} * (\omega\gamma_0)^n \qquad (2\text{-}6)$$

The material parameters, η_0, E_η and n, represent respectively the pre-exponential factor, the flow activation energy and the powerlaw exponent. In case of reacting materials, these material parameters will be, in general, a function of the conversion. Thus, expression (6) is written as:

$$\eta(\alpha, T, \omega\gamma_0) = \eta_0(\alpha) * e^{E_\eta(\alpha)/RT} * (\omega\gamma_0)^{n(\alpha)} \qquad (2\text{-}7)$$

The dynamic viscosity is measured at different heating rates and various frequencies and strains, producing a set of data containing viscosity, temperature, frequency, strain and time. Using the kinetic equation, obtained from the dynamic DSC-experiments, the conversion at each time can be calculated. Accordingly, the material parameters as a function of conversion are determined by analyzing the data at equal conversion. Through fitting, the material parameters as a function of conversion are determined.

2.3.2   Experimental

Dynamic viscosity measurements are performed on a Rheometrics Mechanical Spectrometer (RDS II), using a 25 mm diameter plate-plate geometry. The pellets of the compound are grinded to a fine powder, and then pressed into a 25 mm diameter disc with a height of 1.2 mm. Care is taken not to heat the sample during milling. The pressure used is such that a specific weight of 1.7 g/cm^3 is obtained, equal to the density of the preforms used in the encapsulation process. This is important since the density proved to have a great impact on the values measured for the dynamic viscosity (Figure 2.6).

The dynamic viscosity of the black compound is measured at constant heating rate are carried out at 2, 5, 10 and 20 °C/min at various frequencies and strains. Some experiments on the white compound (without carbon black) are performed as well, to validate the assumption that the rheological behaviour of the two compounds is identical.
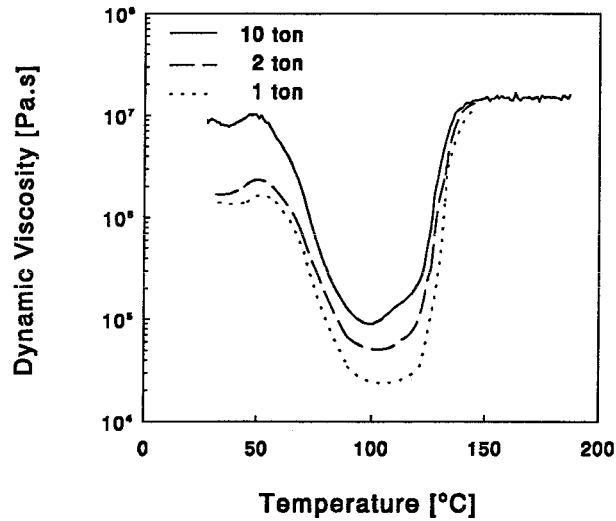
Figure 2.6   Dynamic viscosity measured at a heating rate of 2°C/min for samples of a highly filled epoxy compound prepared at different pressures.

2.3.3   Results and Discussion

In *Figure 2.7* the dynamic viscosity measured at a heating rate of 2 °C/min, a maximum strain of 0.25% and frequencies of 1, 10 and 100 rad/s. This plot also shows measurements performed on the white compound, showing that no major difference in rheological behaviour can be found. In *Figure 2.8* the dynamic viscosity at 20 °C/min, 100 rad/s and strains of 0.25 and 1% is plotted. It is clear that the material not only shows a frequency dependence but also a large strain dependency. At a heating rate of 5 °C/min and various frequencies and strains, experiments are performed to determine whether the material follows the predictions of the model of Doraiswamy[22], that curves with the same effective shear rate superimpose. In *Figure 2.9* the dynamic viscosity is plotted against temperature for constant effective shear rate ($\omega\gamma_0$). As predicted by the model, the data for each effective shear rate form a single master curve.

It is important to notice that other predictions of the constitutive model as proposed by Doraiswamy are not fulfilled. For example, the phase drift δ should be a function of the imposed strain: $\delta = \cos^{-1}[1 - (2\gamma_c /\gamma_0)]$, where γ_c is the strain at yielding. This is not found for the material under consideration.
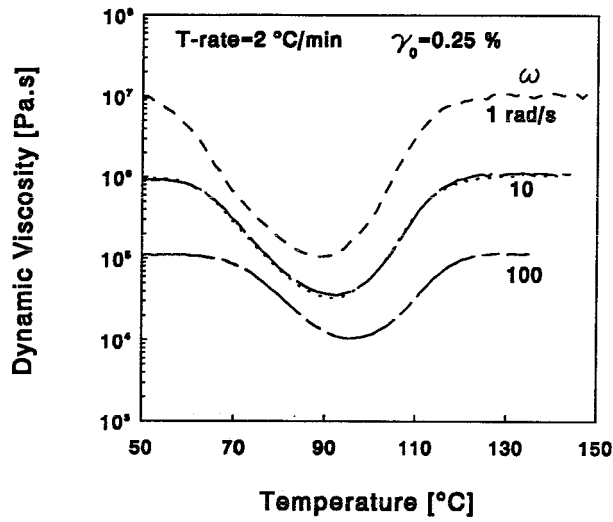
2-8

Figure 2.7 Dynamic viscosity measured at a heating rate of 2°C/min, γ_0 = 0.25% and ω = 1, 10 and 100 rad/s. Comparison with compound without carbon black (..).
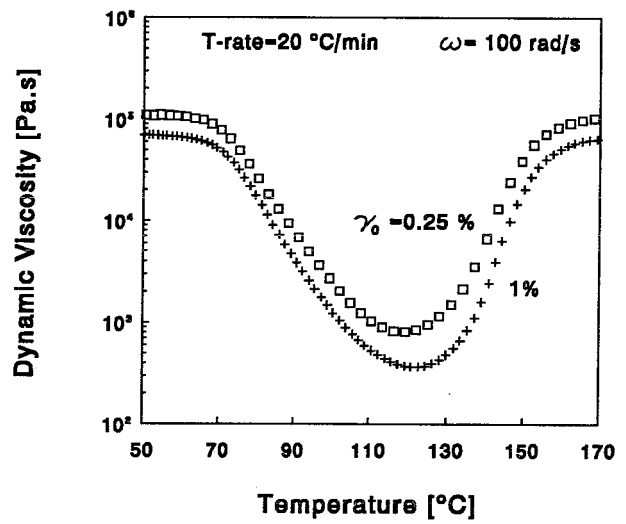
Figure 2.8 Dynamic viscosity measured at a heating rate of 20°C/min, ω = 100 rad/s and γ_0 = 0.25 (□) and 1% (+).
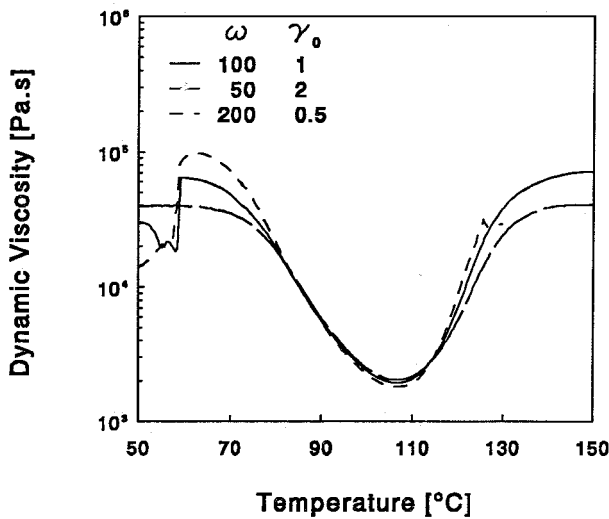
Figure 2.9 Dynamic viscosity plotted against temperature for constant effective shear rate ($\omega\gamma_0$ = 100 s^{-1}) at a heating rate of 5 °C/min.
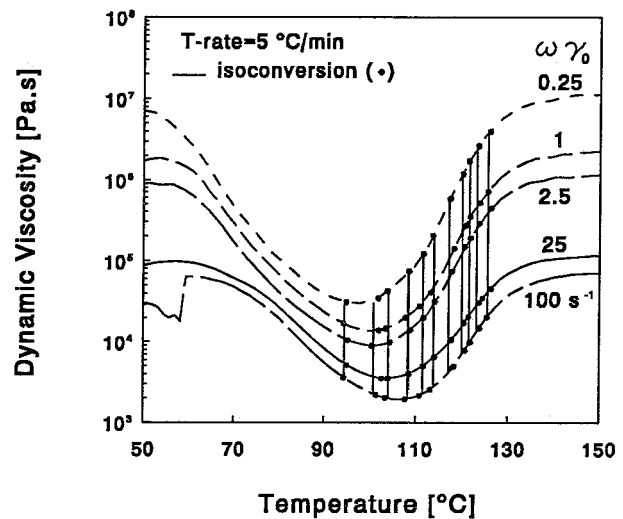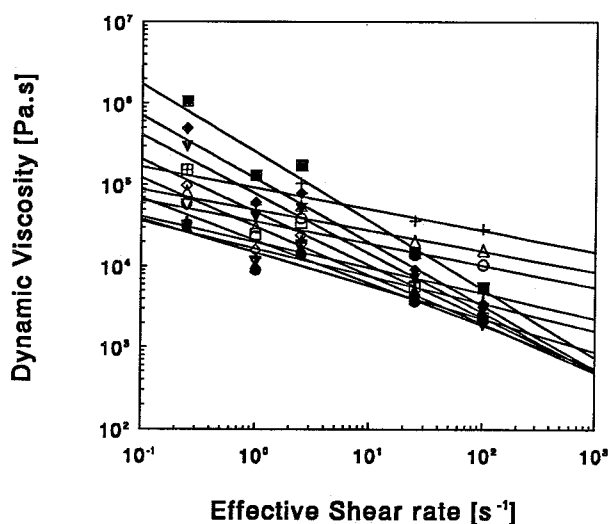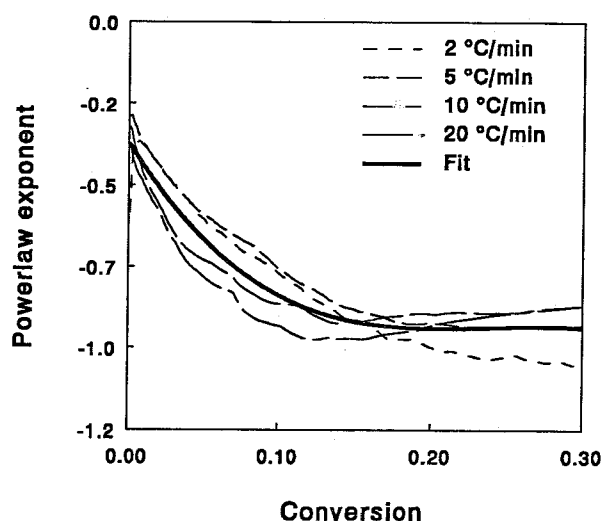
Figure 2.10 Dynamic viscosity plotted against the temperature for experiments performed at a heating rate of 5 °C/min and different effective shear rates; Full lines: lines of equal conversion (0.001 < α < 0.3).

2-9

Experiments are performed at heating rates of 2, 5, 10 and 20 °C/min at various combinations of strains and frequencies, thus at various effective shear rates. For each heating rate the dynamic viscosity is plotted against temperature. Using the kinetic equation obtained in section 2.2, at each point in these curves the conversion can be calculated, and points of equal conversion can be determined. In *Figure 2.10* the results are shown for the experiments performed at a heating rate of 5°C/min. The curves for the other heating rates are submitted to *Appendix I*. Over a range of conversions, the dynamic viscosity is plotted against the effective shear rate *(Figure 2.11)*. The slope of the isoconversion lines in the double logarithmic plot provides the value of the powerlaw exponent in *Equation 2.7*. It is clear that the exponent is not a constant, and that the exponent decreases with the conversion. The powerlaw exponent as a function of the conversion is determined at each heating rate *(Figure 2.12)*. It is assumed that the differences can be neglected and a third order polynomial is fitted on the average values to obtain a description of the powerlaw exponent as a function of the conversion *(Appendix II)*.

For different values of the effective shear rate the dynamic viscosity is measured at different heating rates (2, 5, 10 and 20 °C/min).
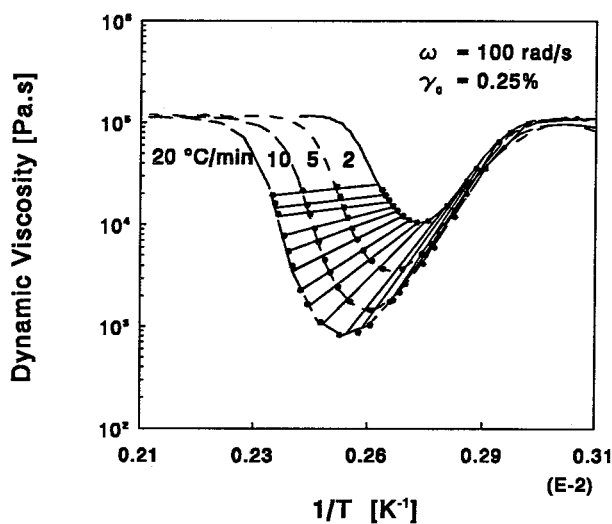
Figure 2.11 Dynamic viscosity plotted against the effective shear rate for various conversions: 0.001 (+); 0.002 (▲); 0.003 (O); 0.01 (+); 0.02 (▲); 0.04 (●); 0.06 (▽); 0.08 (◊); 0.10 (□); 0.12 (▼); 0.14 (◆); 0.18 (■) Full lines: isoconversion.
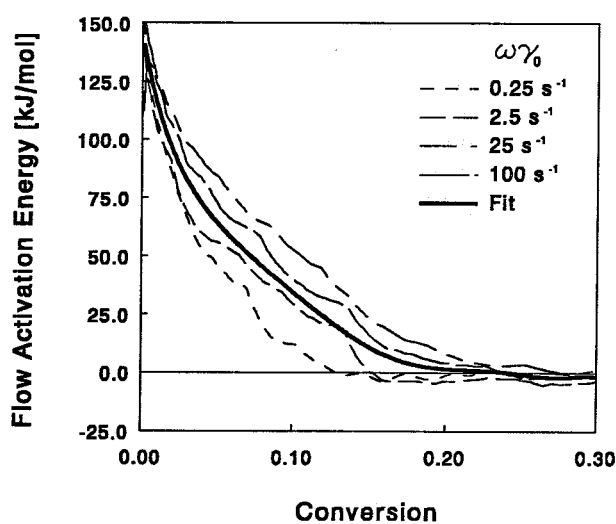
Figure 2.12 Powerlaw exponent (n) obtained from experiments performed at different heating rates plotted against the conversion. Full line: third order polynomial fit on the average values.

In *Figure 2.13* the dynamic viscosity is plotted against the reciprocal temperature for experiments performed at an effective shear rate of 25 s^{-1}. The curves at values of 0.25, 2.5 and 100 s^{-1} for the effective shear rates are submitted to *Appendix I*. Lines of equal conversion were determined, using the kinetic equation and the given temperature-history, and plotted in *Figure 2.13* as well. The slope of these lines (E_η/R) appears to depend on the conversion. Consequently the temperature and conversion dependencies cannot be separated. The conversion dependent flow activation energy *(Eq. 2.7)*, is determined by fitting a ninth order polynomial to the average values of the curves shown in *Figure 2.14*. Since the powerlaw exponent can be calculated over a range of conversions the pre-exponential factor (η_0) can be determined as well using an identical procedure *(Figure 2.15)*. The coefficients of the polynomials obtained by fitting for the conversion dependent factors can be found in *Appendix II*.

Combining effective shear rate dependence as described with the powerlaw, with the temperature and conversion dependence, described with the Arrhenius equation *(Eq.2.7)*, a complete description of the dynamic viscosity as a function of effective shear rate, temperature and conversion is found.
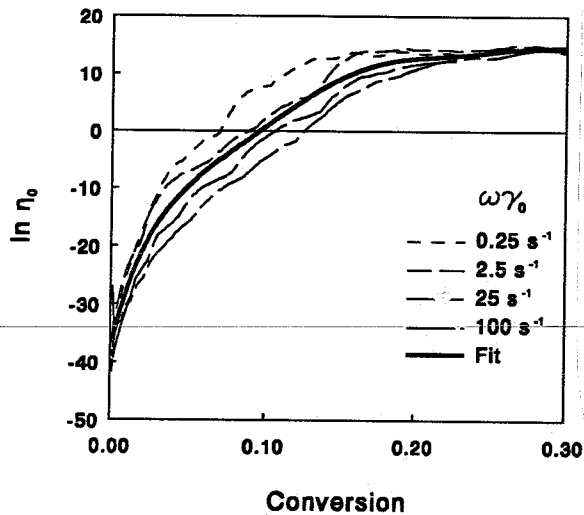

Figure 2.13 Dynamic viscosity plotted against the reciprocal temperature for experiments performed at γ_0 = 0.25%, and ω = 100 rad/s and different heating rates (2, 5, 10, 20 °C/min); --- : lines of equal conversion.

Figure 2.14 Flow activation energy obtained from experiments performed at different effective shear rates plotted against the conversion. Full line: ninth order polynomial fit on the average values.

To study the predictive capabilities of the description obtained, the dynamic viscosity of various experiments are calculated. Using the temperature history of the experiments, the conversion at each time is calculated with the kinetic equation obtained. The calculation of the dynamic viscosity is started after melting and before gelling of the material (α_{gel} = 0.18, see section 2.4). The measured viscosity is compared with the calculated viscosity Figure 2.16, and agrees well.

Figure 2.15 Pre-exponential factor obtained from experiments performed at different effective shear rates plotted against the conversion. Full line: ninth order polynomial fit on the average values.
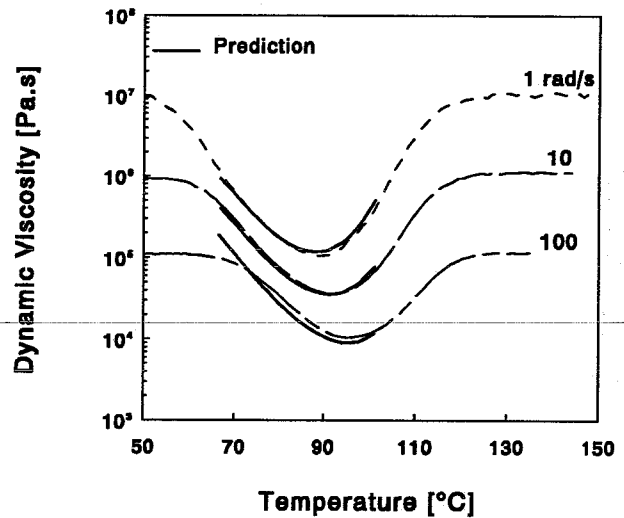
Figure 2.16 Dynamic viscosity plotted against temperature for a heating rate of 2 °C/min, γ_0 = 0.25%, and ω = 1, 10 and 100 rad/s; (--): measured, (-): calculated.

2.4 Gel Point

2.4.1 Theory

Gelation is of critical importance in the processing of thermosets, since the polymer does not flow and is no longer processible beyond this point. Gelation does not inhibit the curing kinetics and therefore cannot be detected by techniques only sensitive to the chemical reaction, such as DSC. The gel point is defined by the conversion at which an infinite molecular network is formed. Prior to gelation, the polymer is soluble, but after gelation both soluble (sol fraction) and insoluble (gel fraction) materials are present[31].

Due to the infinite molecular network formed the steady state viscosity would become infinite at the gel point. The dynamic viscosity however does not become infinite even after gelation due to its definition. In literature various methods have been described to determine the gel point from these measurements. Tung and Dynes[32] suggested that the G'-G" crossover point corresponds to the gel point. Winter[33, 34] however argues that the correspondence is only valid for a limited class of network polymers. Different classes are distinguished by their stress relaxation behaviour near the gel point. As a consequence Winter proposed a general method for detecting gelation from dynamic experiments[35]. Since, according to this theory tan(δ) is independent of frequency at gelation, the gel point may be determined by performing experiments at different frequencies.

Another method for detecting the gel point from dynamic experiments is proposed by Harran et al[36]. They found that gelation may be detected by the appearance of a shoulder in the G" curve. Furthermore they observed that the position of this shoulder is not influenced by frequency or strain, supporting the statement of Winter.

In the following section the gel point is determined first by measuring the soluble fraction of samples with a different degree of cure. The conversion of these samples are determined by measuring the heat of reaction left, using DSC. In section 2.4.3 the theories proposed in literature to determine the gel point from rheological measurements are examined.

2.4.2   Soxhlet Extraction

The amount of sol fraction can be determined through extraction. When the sample is merged into a suitable solvent, all finite molecules will dissolve and diffuse out of the sample. By applying Soxhlet extraction, the solvent is exchanged continuously and eventually no sol fraction will remain.

Samples are prepared by curing small amounts of compound on a metal plate in an oven at 90 °C for various times. The reaction is stopped by quenching in an ice bath. A small amount of these samples are fully cured in the DSC to determine the degree of reaction.

Cellulose thimbles are extracted for 72 hours in tetrahydrofuran and then dried under vacuum. The samples with various curing times are placed in a pre-extracted thimble and extracted in tetrahydrofuran for 96 hours and dried under vacuum until no further weight loss can be detected.

The weight fraction of soluble (W_s) is calculated as follows:

$$W_s = \frac{W_{before\ extraction} - W_{after\ extraction}}{W_{before\ extraction}} \qquad (2\text{-}8)$$

In *Figure 2.17* the soluble fraction of the samples cured for different times are shown as a function of the conversion, as determined with DSC-experiments.

In the pre-gel region, all molecules are finite and will dissolve during extraction. The value for the soluble fraction of ± 33 wt% measured in this region is in reasonable agreement with the fact that according to the specifications of the compound 69%
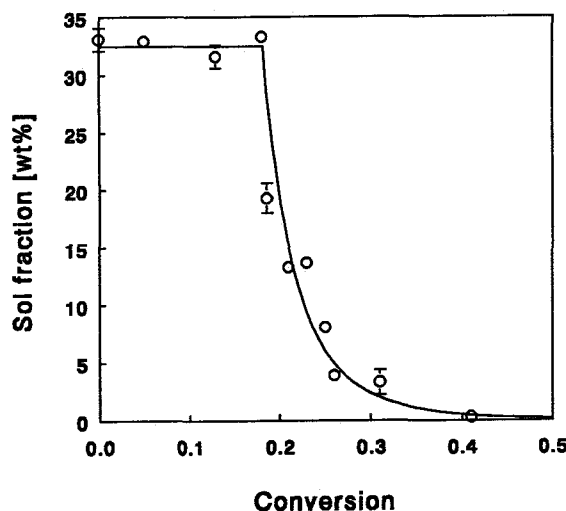

Figure 2.17   Soluble fraction of samples cured for different times plotted against the conversion.

of the compound consists of insoluble silica. In the post-gel stage the soluble fraction decreases with the conversion until no more solubles are present. Samples are prepared with a conversion around the point of gelation until the difference in conversion of the last pre-gel sample and the first post-gel sample is less than 5%. The gel point is then defined as the average of the conversion of these two samples and is found to be 0.18.

2.4.3 Viscoelastic Properties near the Gel Point

To examine the theories proposed in literature to detect the gel point from dynamic experiments, the measurements used to model the dynamic viscosity (section 2.3) are further studied. Tung and Dynes[32] suggested that the G'-G" crossover corresponds to the gel point. In *Figure 2.18* G' and G" are plotted against temperature for measurements performed at a heating rate of 2 °C/min, 0.25% strain and frequencies of 1, 10 and 100 rad/s. It is shown that despite the identical temperature histories of the experiments, the G'-G" crossover does not occur at the same temperature and, since the temperature histories are similar, not at the same level of cure.
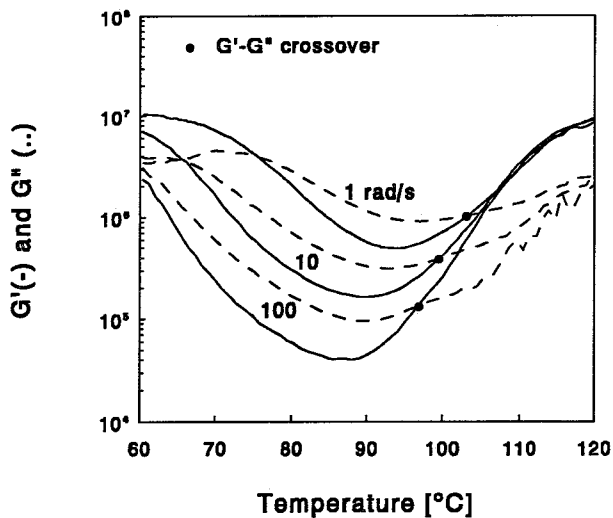
Figure 2.18 G'(..) and G"(-) measured at a heating rate of 2 °C/min plotted against temperature; γ_0 = 0.25%, and ω = 1, 10 and 100 rad/s; (●): G'-G" crossover.
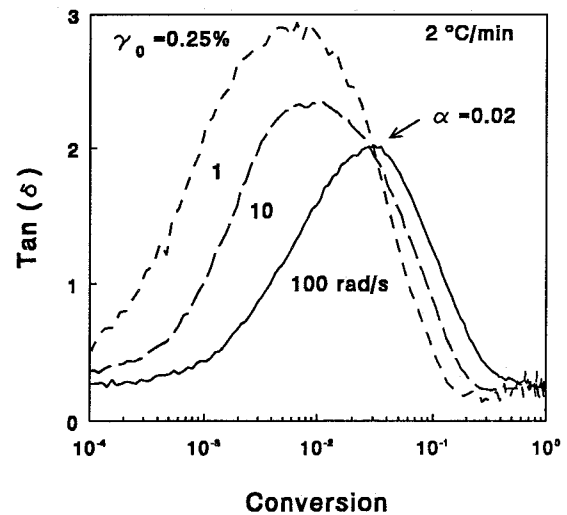
Figure 2.19 Tan (δ) plotted against conversion; heating rate of 2°C/min, γ_0 = 0.25%, and ω = 1, 10 and 100 rad/s.

In *Table II* the conversions at the G'-G" crossover, calculated with the kinetic equation, are listed for all experiments performed. Since gelation should only depend on temperature history, it is clear that the gel point does not correspond with the G'-G" crossover.

According to Winter's findings tan(δ) is independent of frequency at the gel point. In *Figure 2.19* tan(δ) is plotted against the conversion for the same experiments at 2°C/min.

Table II.   Conversion at the G'-G" crossover for the rheological measurements performed at various heating rates, frequencies and maximum strains.

T-rate [°C/min]	ω [rad/s]	γ_0 [%]	$\omega\gamma_0$ [s^{-1}]	$\alpha_{crossover}$
2	1	0.25	0.25	0.061
2	10	0.25	2.5	0.088
2	100	0.25	25	0.134
5	1	0.25	0.25	0.046
5	1	1	1	0.074
5	4	0.25	1	0.057
5	10	0.25	2.5	0.049
5	50	2	100	0.132
5	100	0.25	25	0.087
5	100	1	100	0.131
5	200	0.5	100	0.131
10	1	0.25	0.25	0.045
10	10	0.25	2.5	0.039
10	50	2	100	0.103
10	100	0.25	25	0.074
10	100	1	100	0.094
20	1	0.25	0.25	0.047
20	10	0.25	2.5	0.036
20	50	2	100	0.094
20	100	0.25	25	0.053
20	100	1	100	0.085

At a conversion of 0.03 the curves cross and thus in that point tan(δ) is found to be independent of the frequency. For other series of experiments, such
point could not be detected unambiguously. The plots for the experiments for heating rates of 5, 10 and 20 °C/min and various frequencies are submitted to *Appendix III*. It seems that for a conversion of ± 0.18, the gel point as detected by extraction experiments (section 2.4.2), some tan(δ) curves do crossover. Winter's approach seems however not consistent for the whole range of experiments performed on this type of materials.

It appears that none of the methods proposed in literature are capable to detect the gel point from dynamic experiments for the system used in our study. Probably the high level of additives, especially the 70 wt% of solid particles, cause the models to fail for the epoxy compound studied.

However, evaluating the dynamic results, it was found that above a certain degree of reaction the storage modulus, G', is no longer a function of frequency or temperature. This is shown in *Figure 2.20*, where G' is plotted against the conversion for dynamic experiments conducted at a maximum strain of 0.25% with various heating rates and frequencies. All G' curves converge after a defined level of cure is reached.
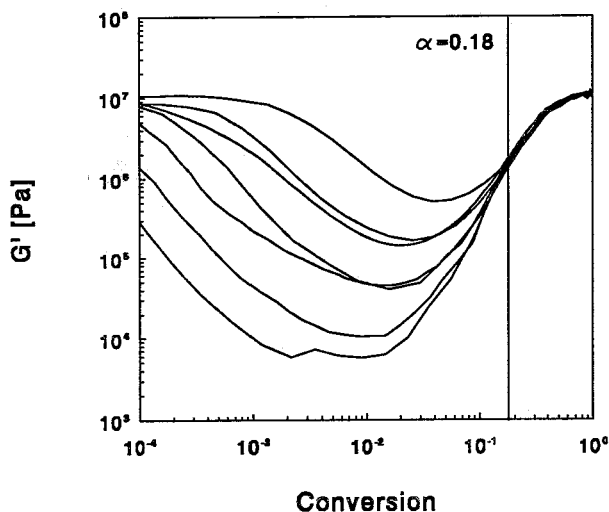
Figure 2.20 G' plotted against the conversion for dynamic experiments performed at γ_0=0.25%, and various combinations of frequencies and heating rates.
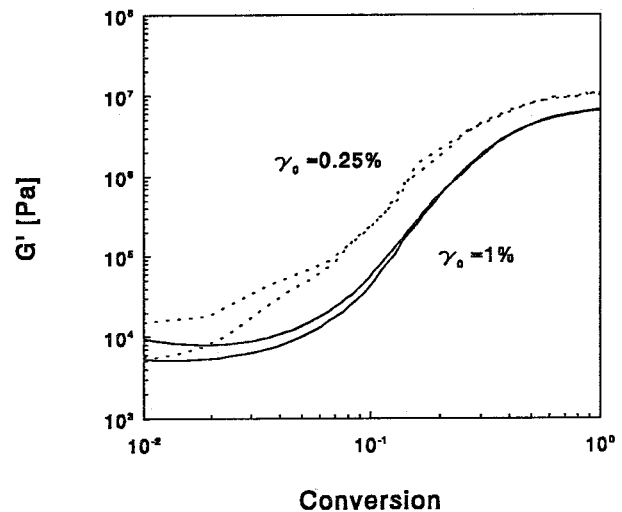
Figure 2.21 G' plotted against the conversion for dynamic experiments performed at γ_0 = 0.25% (..) and 1% (-).

It is known that beyond gelation, in the rubbery state, G' is hardly dependent on frequency and temperature[37]. Before gelation, however, pronounced temperature and frequency dependencies are to be expected. This means that the conversion at which the curves converge corresponds with the gel point. From *Figure 2.20* is appears that the conversion at convergence is in reasonable agreement with the gel point as determined through extraction experiments (α_{gel}=0.18). Unfortunately, the transition is not evident enough to serve as an unambiguous technique to detect the gel point.

The maximum strain however does influence the G' curve as shown in *Figure 2.21*, where G' is plotted against the conversion for experiments performed at different strains. The strain dependency expresses the non-linear behaviour of this crosslinked system.

Neither the G'-G" crossover or the frequency-independency of tan (δ) can be used to determine the gel point of the system studied. However, the curves of G' against conversion for measurements performed at an equal maximum strain appear to converge after a conversion is reached of approximately 0.18, which agrees with the gel point determined through extraction experiments.

2.5 Thermal Properties

For the numerical simulation of flow of the compound it is necessary to know the thermal properties. Thermal diffusivity (α_T) is the property of the material which determines the rate at which the material will gain or lose heat. The thermal diffusivity is given by the relation[38]:

$$\alpha_T = \frac{\lambda}{\rho * c_p} \qquad [2\text{-}9]$$

in which λ is the thermal conductivity coefficient, ρ is the density and c_p is the heat capacity at constant pressure. The density of the compound, used in the visualisation experiments is 1700 kg/m^3. Both the heat capacity and the thermal conductivity coefficient are determined by SWO Polymertechnik (Krefeld,Germany).

2.5.1 Heat Capacity

The heat capacity is measured using Differential Scanning Calorimetry at heating rate of 5 °C/min from 23 to 300 °C. To obtain the absolute value of the heat capacity the instrument is calibrated accurately. The heat capacity appears to be ±1400 [J/kg.K] (Figure 2.22). It shows that not enough data are obtained to determine what influence the degree of reaction has on the heat capacity, so the heat capacity is assumed to be a constant.
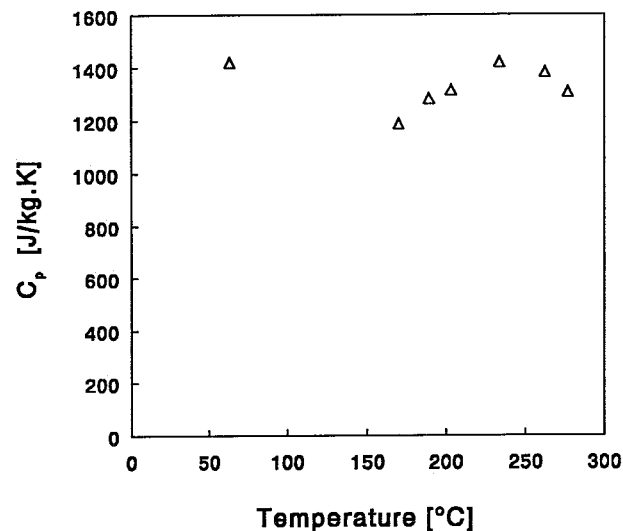
Figure 2.22   The heat capacity plotted against temperature; heating rate of 5 °C/min.

2.5.2　Thermal Conductivity

The thermal conductivity is measured using the "K-system II" which is a transient technique to measure the thermal conductivity of polymers. The thermal conductivity is measured during cure, since cure can have a significant influence on the thermal conductivity of thermosets[38]. However the influence of cure is not expected to be significant for highly filled systems. The experiments are performed at three different temperatures: 80, 90 and 100 °C. The results are shown in *Figure 2.23*. At each temperature the data scatter between 0.6 and 0.8 [W/m.K]. The dispersion of the data is that large that the influence of cure can not be detected. The thermal conductivity coefficient is therefore assumed constant: 0.7 [W/m.K].
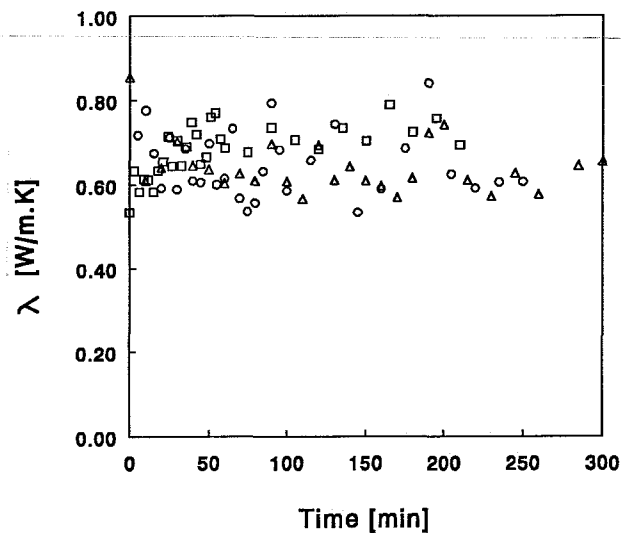
Figure 2.23　The thermal conductivity measured at a constant temperature plotted against time; Temperatures: 80 °C (Δ), 90 °C (O) and 100 °C (□).

3   Reactive Flows

For the development of a technology that allows for IC-encapsulation with two or more components it is, in order to obtain the desired configuration in the mould, necessary to be able to predict the distribution of the materials in the transfer pot. For such a prediction a numerical model for reactive flow is needed. In order to test the predictive capability of the numerical model, the piston driven flow is chosen since this flow meets some important requirements and has some decisive advantages. The initial and boundary conditions are well defined and variables as temperature, velocity and initial configuration are easily controlled. Comparison with numerical results is performed via visualisation of the deformation patterns. The complete deformation history proves to be more discriminating than velocity measurements[39].

In section 3.1 of this chapter the reactive flow of a highly filled epoxy moulding compound is studied in a piston driven flow, using a combination of experiments and numerical analyses. The deformation patterns are experimentally visualised using different coloured slices of the same material.
Another important requirement for the development of a multilayer technique, is the reproducibility and controllability of the transfer moulding process for a given number of cavities per plunger. In section 3.2 the deformation patterns in a two cavity mould geometry, used in the encapsulation process, are experimentally visualised. An improved geometry for a more controlled process is suggested and studied in section 3.3.

3.1   Piston Driven Flow

A piston driven flow is described as a flow of material packed in a cylinder between two pistons, pushed upwards by the piston at the bottom. To study this flow, visualisation experiments are performed by using different coloured slices of the characterized epoxy compound, which show the deformation patterns. Accordingly the finite element method is used to simulate the piston driven flow of the reactive material. The experimental and numerical results are compared, testing the predictive capability of the numerical model.

3.1.1   Visualisation Experiments

Introduction

To perform well defined experiments which visualise the deformation patterns of a reactive material in a piston driven flow, an apparatus is developed which is shown in *Figure 3.1*. Between two pistons a stack of slices ($\emptyset$ 16 mm) is piled. The split barrel allows for preheating of the walls before it is placed around the pistons and the reactive material, without introducing any initial deformation. The setup is mounted in a transfer press. Due to the configuration of the total apparatus the closed cylinder is moved downwards instead of the lower piston moving upwards. It is trivial that the resulting flow is identical with a piston driven flow[39].

The black and white compounds, characterized in chapter 2, are used to provide for the different coloured slices of the reactive material. The compounds are grinded to a fine powder and then pressed into a 16 mm diameter disc with a height of 5 mm. Care is taken not to heat the sample during grinding. The pressure used is such that a density of 1.7 g/cm^3 is obtained, equal to the density of the preforms used in the encapsulation process. Black and white slices are piled up forming a stack with a total height of 50 mm.

Figure 3.1   Apparatus for the visualisation of piston driven flow.

Melting the material gives a spatial and transient distribution of the cure level as occurs in an actual flow of reactive material. To investigate in which way the cure level influences the flow, experiments with clear differences in the cure level have to be performed. To accomplish such discriminating experiments the Damköhler IV number *(Appendix IV)* has to be large (DaIV > 1)[38]:

$$DaIV = \frac{r_0^2 \rho_0 h_r}{\Delta T_{op} \lambda_0 t_r} \qquad [3-1]$$

This number represents the ratio of rates of temperature rise due to reaction and conduction. For a small Damköhler IV number curing takes place rather uniformly across the thickness of the part[38]. Given the experimental setup and the material, the values for r_0, h_r, ρ_0, t_r and λ_0 can not be varied. However the Damköhler IV can be set with the temperature of the walls, T_{wall} ($\Delta T_{op} = |T_{wall} - T_{start}|$). The level of cure can be varied by the delay time t_d; the time between closing the split barrel and moving it.

To define the experimental window, the delay time (t_d) is varied, as well as the temperature of the cylinder (T_{wall}). Wall slip should be avoided since it is not included in the numerical model of the piston driven flow (section 3.1.2). Gelling of a too large amount of material is not desired as well. Within the experimental window experiments are performed, applying various displacements. The influence of the speed of the wall is studied using two speeds.

To investigate the possibility of determining the gel point, experiments are performed in which the cylinder is moved more than once.

At the end of the experiment the material is fully cured at a high temperature (150°C) for ± 15 minutes. The sample is removed and cut through the midplane using a diamond saw to allow for visual inspection of the internal deformation.

Experimental Results and Discussion

Experiments were performed at a velocity of the cylinder of 2 mm/s and a displacement of 20 mm at various temperatures and various time spans between closing and moving of the cylinder (t_d). This way the window of experimental parameters giving useful results was determined. In *Figure 3.2* the results are presented. It shows that at too high temperatures and loo large values of t_d, part of the material at the wall slips at the surface of the cylinder. This becomes more clear when the outer surface of the samples is studied. When the material sticks to the surface of the sample, the outer surface, which is not created at the side of the
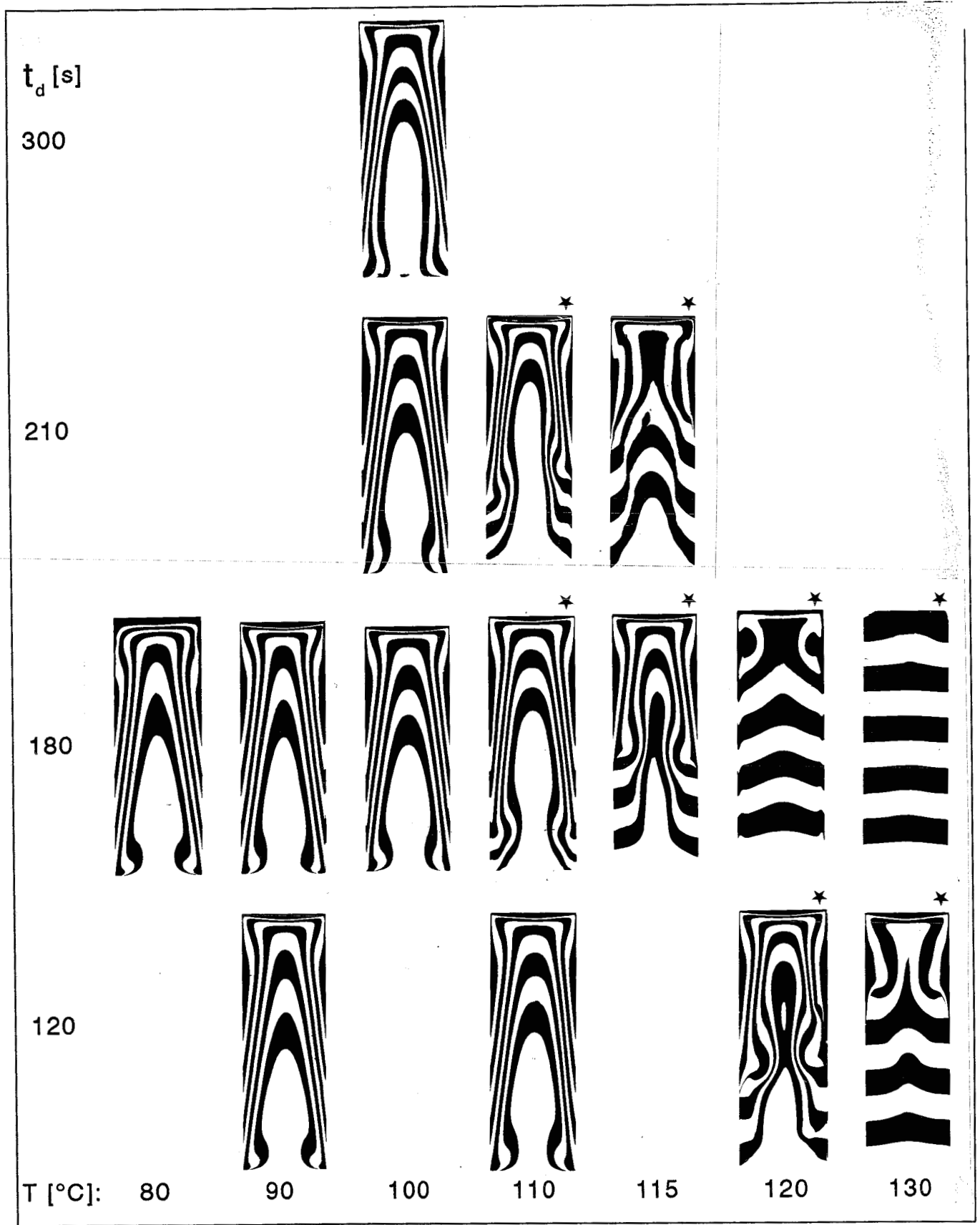
Figure 3.2 Deformation patterns (midplane) resulting from piston driven flow at various temperatures and various delay times (t_d); velocity of the cylinder: 2 mm/s downwards; displacement: 20 mm; (★): slip.

driven piston, or removed by the driving piston, will contain its original configuration *(Figure 3.3: A-E)*. When slip occurs this will not be the case *(Figure 3.3: X)*. Slip appears to take place at the driving piston first.

In *Figure 3.4* the conversion at the cylinder wall is calculated for various temperatures, using the kinetic equation as determined in section 2.2. For different conditions during the visualisation experiments, it is indicated whether slip or no slip occurs. It appears that for conversions higher than ± 0.05 slip occurs, although it was expected that slip would occur at gelation. The gel point was however determined to be 18 % (section 2.4). It may be possible that already at a cure level of 5 % the no-flow condition for the material at the wall holds.

Some experiments are performed with the cylinder moved twice: first 3 mm downwards at $t_{d,1}$ followed by a 3 mm upwards displacement at $t_{d,2}$. The stack of material used in these experiments is composed of mostly white compound with a thin disc (3 mm) of black compound in the middle as well as at the pistons. These experiments were all performed at 100 °C, v = 2 mm/s and $t_{d,1}$=180 s. Under these conditions the conversion at the wall at the first deformation will be lower than 5 %. At $t_{d,2}$ the conversion at the wall will be larger than 5 %.

Figure 3.3   Outer surfaces of samples subjected to the piston driven flow at different displacements; A-E: stick at the cylinder wall; X: slip.

3-5
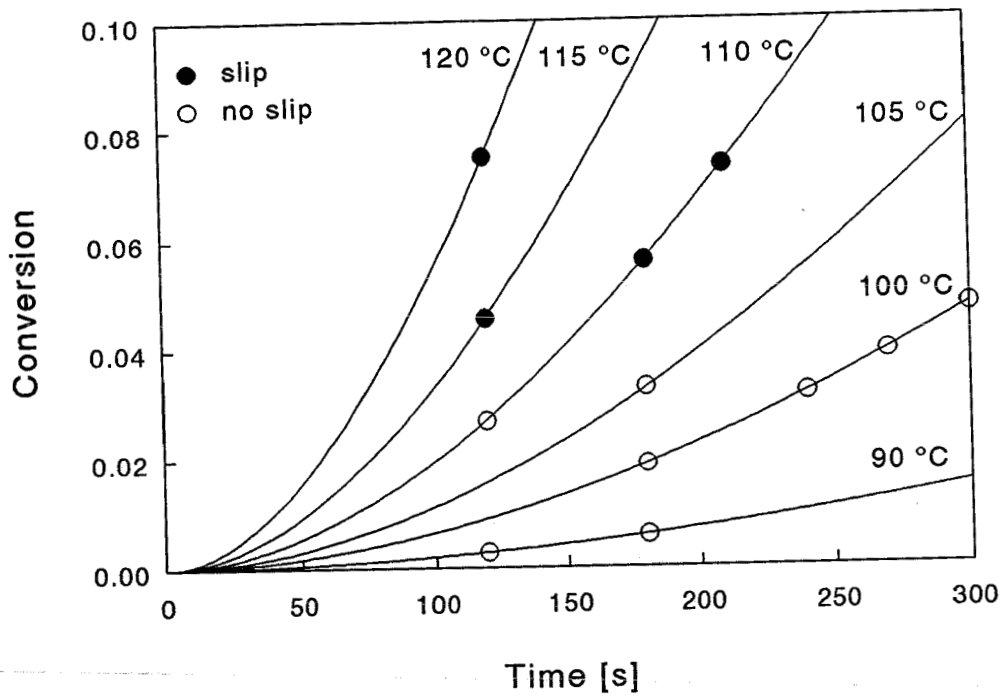
Figure 3.4   Conversion at the cylinder wall calculated for different isothermals.
○: stick ; ●: slip.
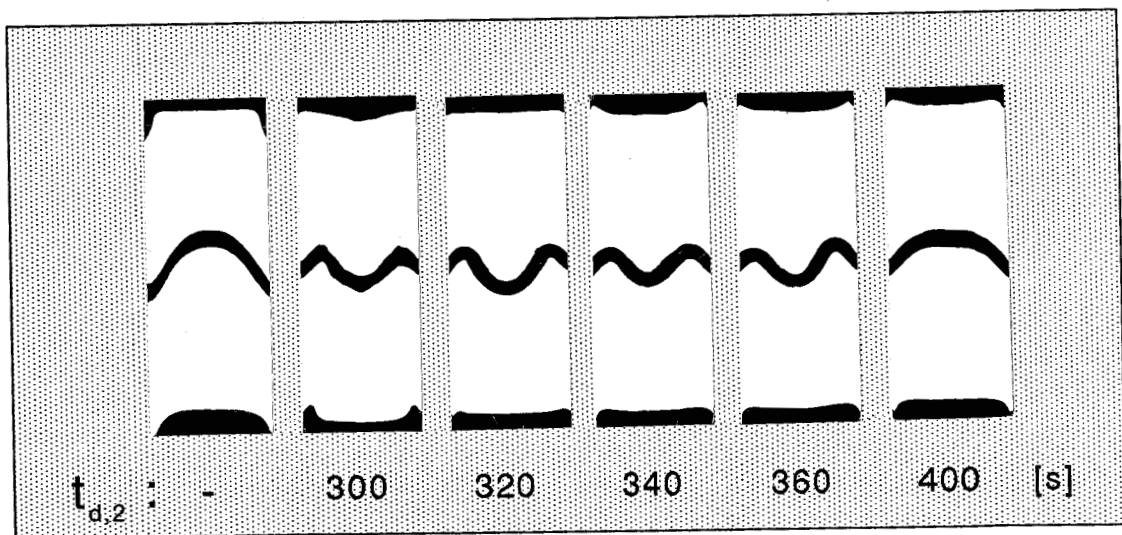
Figure 3.5   Deformation patterns resulting from oscillating piston driven flow experiments.
T_{wall}= 100°C, $t_{d,1}$=180 s, v = 2 mm/s (first down, then up), displacement is 3 mm.
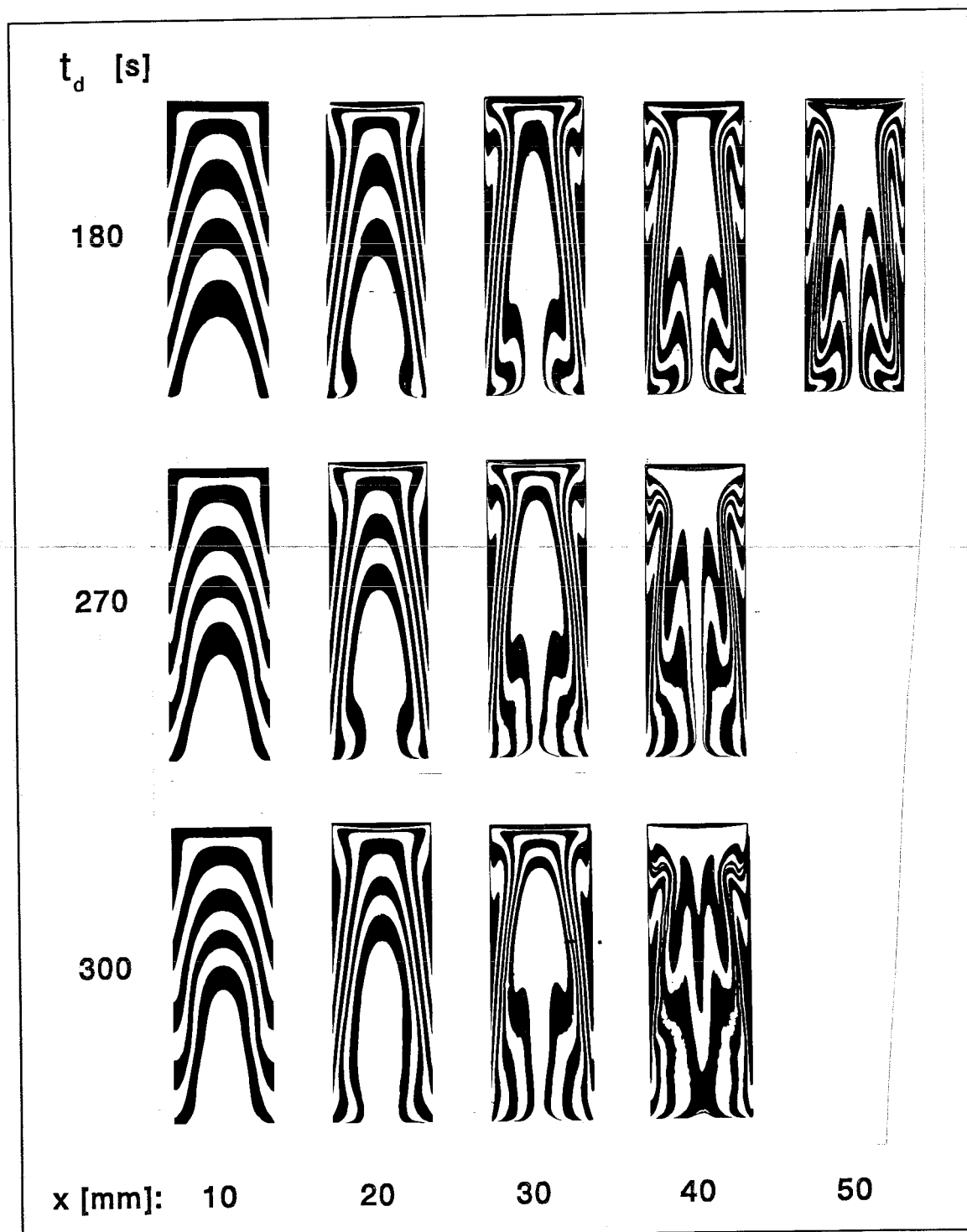
Figure 3.6   Deformation patterns resulting from piston driven flow for various displacements at t_d=180, 270 and 300 s; velocity of the cylinder: 2 mm/s downwards.

The results are shown in *Figure 3.5*. The first sample has only been moved once after 180 s. The other samples differ only in $t_{d,2}$: 300, 320, 340, 360 and 400 seconds.

For $t_{d,2}$=300 s a no flow region is observed near the wall. Increasing this second delay time did not show a clear inward shift of the no flow region as was expected. This is not understood yet. Only for t_d=400 s it seems that any flow of interest is not possible anymore. The results were obscured by wall slip. No further attempt was made to improve these experiments, although it proves to be important to investigate this phenomenon more precise in future. It seems to be meaningful to define a rheological gel point besides the chemical gel point.

Within the experimental window it appears that in the temperature range of 110-115 °C the process is critical, with respect to wall slip. Since time is a better controllable parameter than temperature, several experiments were performed at a temperature of 100 °C and a wall speed of 2 mm/s and heating times ≥ 180 s. These experimental restrictions limit the value of the Damköhler IV number. The resulting deformation patterns are shown in *Figure 3.6*. The patterns for different displacements show the development of a fountain flow near the driven (upper) piston and a reverse fountain flow at the driving (lower) piston. In between a Poiseuille flow arises. The influence of cure is studied by varying t_d. Increasing t_d results in smaller deformations close to the cylinder wall and larger deformations at the centre of the samples. Furthermore the turning point of the reverse fountain flow at the driving piston appears at a larger distance from the piston. Unfortunately, the differences in the deformation patterns at different t_d are not that large since, due to the relative low Damköhler IV number (0.21, *see Appendix IV*), the experiments are not as discriminating with respect to the cure level as wished for.

To study the influence of the wall speed, experiments are performed at T=100 °C, t_d=180 s and a velocity of now 100 mm/s. In *Figure 3.7* the results of these experiments are shown. It appears that the deformation patterns are influenced by the velocity of the cylinder, and thus by the shear rate, indicating that the material is shear rate dependent.

In conclusion the experiments show that the deformation patterns of the piston driven flow for a reactive material are successfully visualised. Due to the occurrence of slip at low levels of cure, the temperature range for experiments showing no slip is limited to relatively low temperatures or short delay times. Consequently, the Damköhler IV number is relatively low. The use of the chemical gel point as a no-flow condition seems to be questionable for this material.

x [mm]:   10   20   30   40
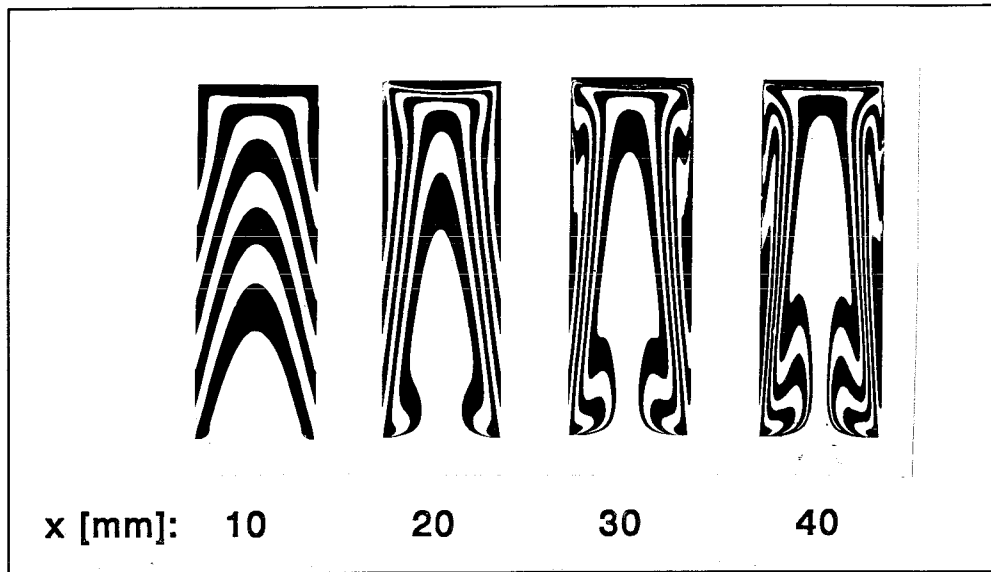
Figure 3.7   Deformation patterns resulting from piston driven flow performed at a velocity of the cylinder of 100 mm/s downwards; T_{wall}= 100 °C, t_d=180 s.

3.1.2   Numerical Simulation

Introduction

To simulate the piston driven flow numerically a standard finite element package for flow simulations (Sepran)[40] is used. The numerical method includes a particle tracking algorithm which is able to predict where a particle will flow in a mould. Deformation patterns can be obtained and directly compared to the experimental visualisation results, thus verifying the numerical model and constitutive equation used.

The advantage of mathematical models is that they can be inverted. In this way the position at which a particle has to start to accomplish a defined final position inside a product can be predicted. In case two materials with different (flow) properties are used, only an iterative method will yield the desired initial configuration. Numerical simulation of reactive flows is therefore a useful tool for the development of a multicomponent transfer moulding process, avoiding too much trial and error in practice every time a different mould geometry has to be used.

For particle tracking each particle is identified by a set of labels[41]. These labels contain information about the position (and thus colour) of the particle in the original configuration.

In case of reactive flow, four equations have to be solved simultaneously[42]. Next to the mass-, momentum- and energy balance equations the conversion of the reactive material yields a fourth balance equation: the mole balance equation. As prediction of the conversion field, which is strongly convection dominated, implies precise knowledge on the "history" of the flow, it is essential to compute an accurate velocity profile.

As shown in chapter 2, the reactive character of the material results in changes in the reaction rates, the heat of reaction and changes in physical properties. Thermally induced polymerization and crosslinking are by nature instationary processes. This results in a system of unsteady equations.

The material is described as an incompressible, heat conducting, reactive viscous fluid. For the description of the reaction kinetics of the epoxy compound the kinetic equation obtained in section 2.2 is used. The material is assumed to behave as a generalized Newtonian fluid for which the viscosity is a function of temperature, conversion and shear rate (section 2.3). Since the Reynolds number for this material is found to be small (Re<<1) a Stokes flow is assumed *(Appendix IV)*. The mass transfer Peclet number involved is very large ($Pe_m = 10^8$), therefore molecular

diffusion can be neglected[42]. In order to approach solid material behaviour, the viscosity for conversions beyond the gel point is set to ten times the value of the zero shear viscosity at the gel point. This method of modelling the no-flow behaviour of the gel, was numerical tested for the desired behaviour by Corbey[42] and was found to be satisfactory.

Numerical method

To solve the system of non-linear coupled partial differential equations, the finite element package Sepran is employed[40]. The velocity field is calculated using enriched quadratic triangles (axisymmetric). The energy and conversion balances are discretized using quadratic triangles. This leaves a system of four coupled equations. The equations are coupled by their right hand sides and the convection terms. Uncoupling is provided by treating these terms explicitly. In order to avoid partial pivoting, the equations of momentum and mass are uncoupled with the penalty function method[43]. To approximate the time derivatives, an Euler implicit method is used[44].

Because of the large mass transfer Peclet number, the molecular diffusion is extremely small and in fact neglected. This may lead to oscillations in the solution. This behaviour can be suppressed by upwinding techniques[42]. By applying streamline upwinding artificial diffusion is introduced in the direction of the streamlines. The justification of such an approach is merely numerical founded and not guided by physical considerations.

Results

The geometry that is dealt with consists of a 50 x $\varnothing$ 16 mm axisymmetric cavity between two pistons with a moving wall. When the wall is moved downwards the upper piston can be considered as the driven piston and the lower piston as the driving piston. A no-slip condition is assumed on all boundaries. Since the conditions are axisymmetric, half the part of a lengthwise cross-section is considered. The mesh that is used consists of 460 elements. The mesh is shown in *Figure 3.8*.

The wall of the cavity is kept at a constant temperature. The pistons are initially assumed to be thermally insulated ($\alpha_{T,steel} = \alpha_{T,compound}$). This is a first approximation of the real situation where the pistons are heated faster than the compound as the thermal diffusivity coefficient of steel is larger than that of the compound.

So boundary conditions are (v_w = velocity at the wall; v_x = velocity in radial direction; v_y = velocity in vertical direction; T_w = temperature at the wall):
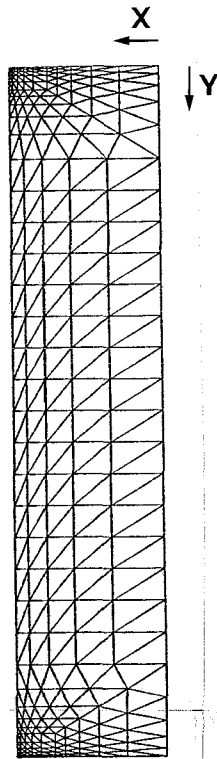
Figure 3.8 Element mesh with y-coordinate along the cavity and x-coordinate in cross direction.
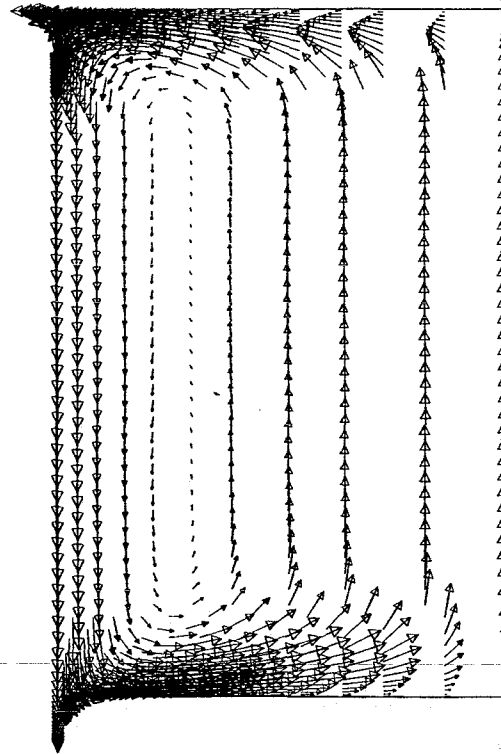
Figure 3.9 Vector plot of velocity at t = 305 seconds (displacement = 10 mm); T_w = 100 °C.

Table 3.1: Material parameters initially used in the numerical simulation.

k_1	$6.84 * 10^5$	[s^{-1}]	c_p	1000	[$J.kg^{-1}.K^{-1}$]
k_2	$1.60 * 10^7$	[s^{-1}]	λ	0.7	[$W.m^{-1}.K^{-1}$]
ΔE_1	$1.02 * 10^5$	[J/mol]	ρ	1700	[$kg.m^{-3}$]
ΔE_2	$7.24 * 10^4$	[J/mol]	α_{gel}	0.18	[-]
n	1.09	[-]	H_r	$-1.02 *10^8$	[$J.m^3$]
m	0.45	[-]	η (T, α, $\dot{\gamma}$)	see App.II	[Pa.s]

Pistons	:	$v_x = 0$	$v_y = 0$		$\partial T/\partial y = 0$
Wall	:	$v_x = 0$	$v_y = 0$	$t < t_d$	$T = T_w$
			$v_y = v_w$	$t \geq t_d$	
Middle cavity:		$v_x = 0$	$\partial v_y/\partial x = 0$		$\partial T/\partial x = 0$

The initial conditions for the whole domain are: T = 293 K, the conversion $\alpha=0$ and all velocities v=0.

In *Table 3.1* the material parameters initially used in the numerical simulations are summarized. The parameters for the kinetic equation and the heat of reaction H_r are determined in section 2.2. The coefficients of the polynomials used in the viscosity model are determined in section 2.3 and summarized in *Appendix II*. To prevent that the viscosity becomes infinite at very low shear rates, a typical powerlaw deficiency, the viscosity for shear rates smaller than 0.01 $[s^{-1}]$ is set to the value of the viscosity at a shear rate of 0.01 $[s^{-1}]$. The experimental values of the heat capacity (c_p) and the thermal conductivity coefficient (λ) are determined in chapter 2 as well. However, at the start of these simulations these experiments were not yet performed so typical values found in literature[3, 13] are initially used. The density (ρ) is obtained from the supplier.

The first simulations are performed under conditions nearly identical to those of the visualisation experiments discussed in section 3.1.1. The simulations are performed for three different temperatures : 90, 100 and 110 °C, and at t_d=180 and 300 seconds. The results for T_w = 90 and 110 °C are presented in order to be able to investigate how sensitive the results are for variations in the wall temperature. For the visualisation the initial y-coordinate is transported. The velocity at the wall is 2 mm/s. In *Figure 3.10* the deformation patterns resulting from the simulations at displacements of 10, 20, 30 and 40 mm are showed. As in the visualisation experiments, the fountain flow at the driven and the reverse fountain flow at the driving piston can be recognized. The black spots along the midplane seen in the same figures are due to material particles with an y-label greater than the maximum of 50 mm and origin from the singular point at the piston corner. They do not influence the deformation patterns elsewhere. In the velocity field *(Figure 3.9)* it is shown that the material approaches the driving piston along the wall, enters the reverse fountain flow region, moves towards the midplane and is directed to the driven piston.

Comparing these results to the visualisation experiments *(Figure 3.6)* it appears that the flow, especially at large displacements, runs behind. It can be concluded that the numerical simulations agree well in a qualitatively sense with the experimental visualisations. This agreement is better for the smaller delay time.
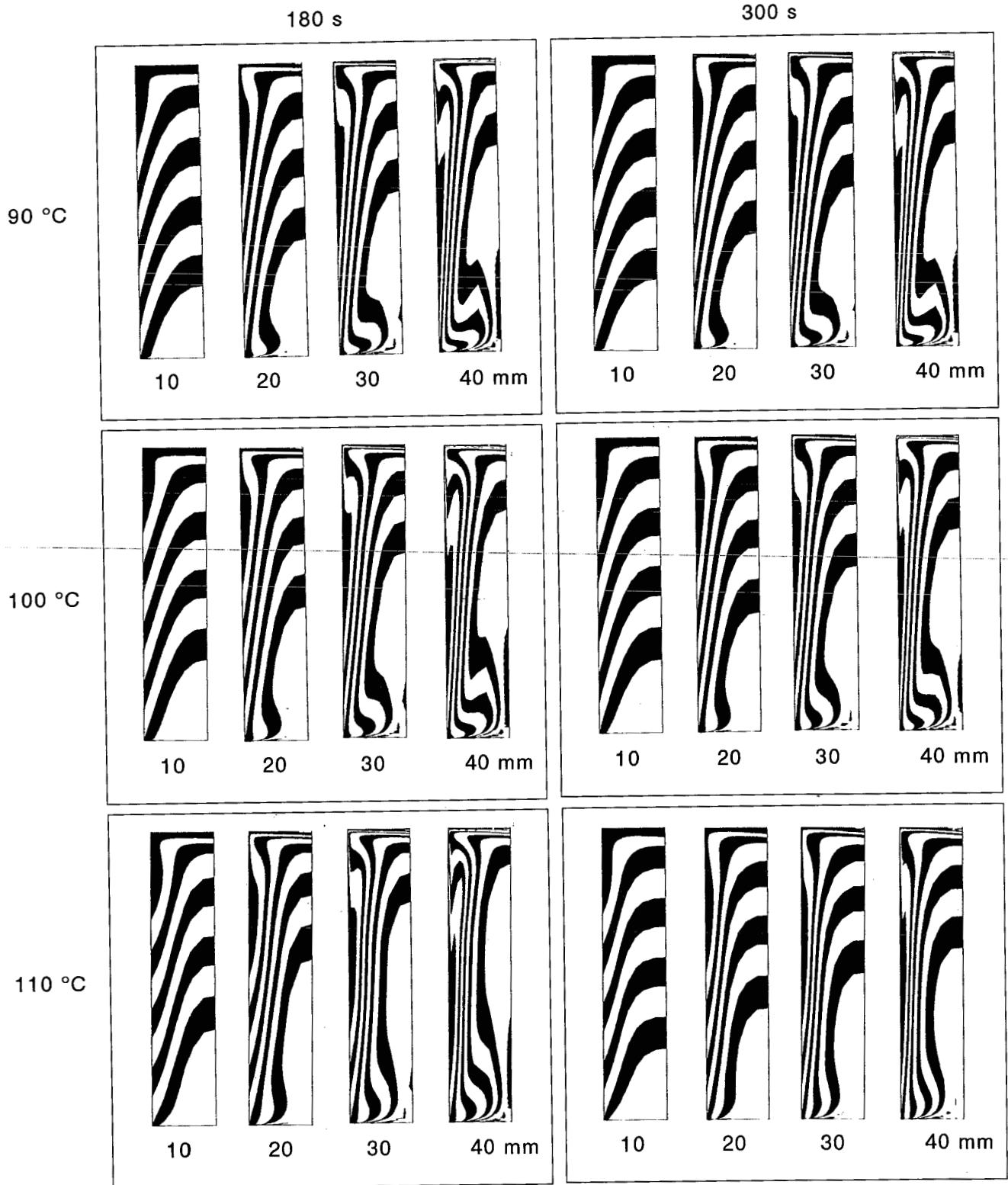
Figure 3.10   Deformation patterns resulting from numerical simulations. T_w= 90, 100 and 110 °C; t_d=180 and 300 seconds; v_w= 2 mm/s; displacements: 10, 20, 30 and 40 mm.

Since the value for the thermal diffusivity coefficient ($\alpha_T = \lambda / \rho.c_p$ [m^2 /s]) used in the previous simulations is based on estimated values for the heat capacity (c_p) and the thermal conductivity coefficient (λ), the influence of this parameter is studied by changing the value of the heat capacity. Simulations varying this coefficient (4c_p and $c_p/4$) are performed for piston driven flow with a wall temperature of 100 °C and t_d = 180 and 300 seconds. The resulting deformation patterns are submitted to *Appendix V*. At first instance the main difference between the numerical and experimental results can be expressed by the distance o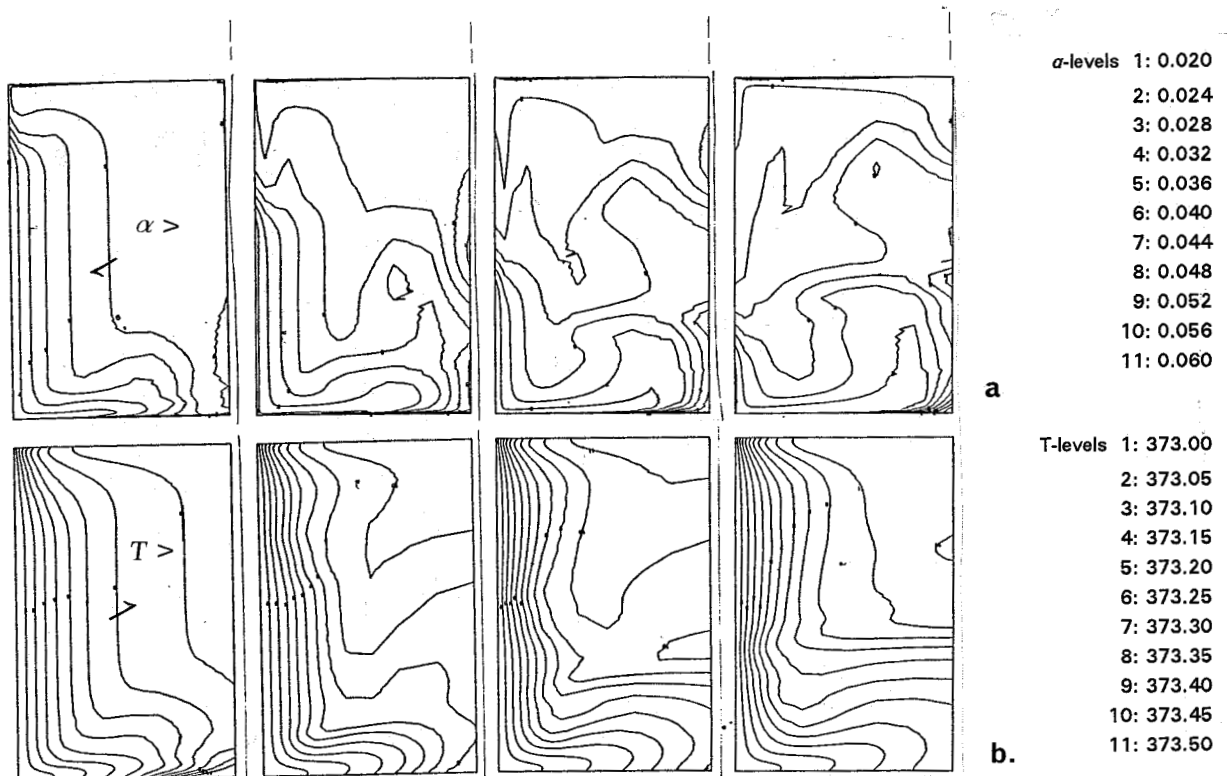ver which the (black) material flows along the midplane. Therefore, in *Figure 3.11* the vertical displacement of the material at the bottom along the midplane is plotted against the displacement of the wall, and compared to the experimental values. The results show that the diffusivity coefficient, has a pronounced effect on the deformation patterns. However, increasing as well as decreasing the coefficient both result in a larger difference with the visualisation experiments. It was therefore desirable to determine the thermal conductivity coefficient (λ) and the heat capacity (c_p) more precisely, and not to be satisfied with values from literature.
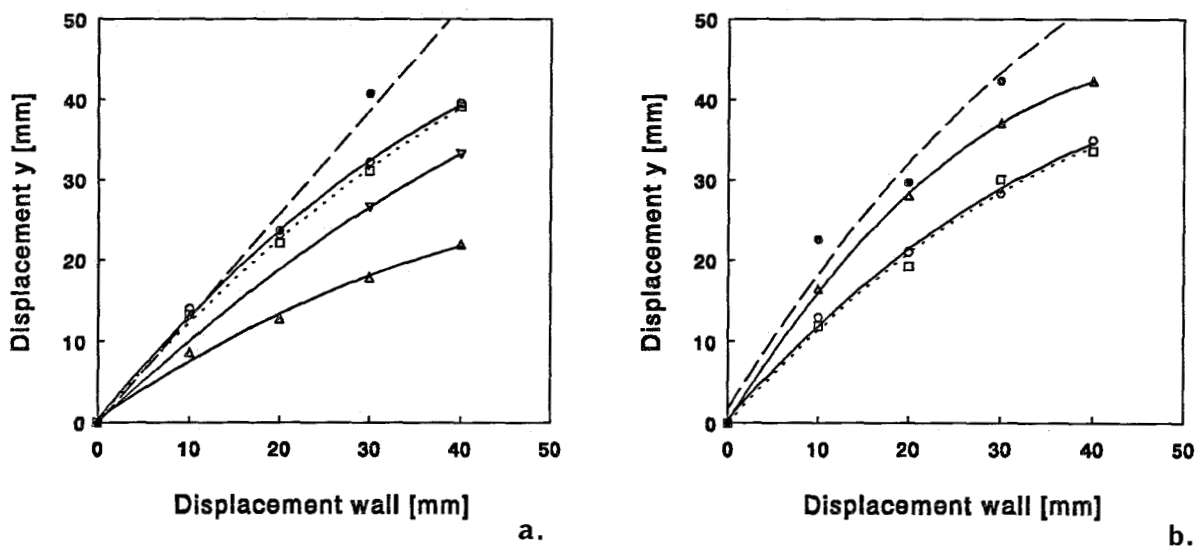
Figure 3.11   The vertical displacement y of the material at the bottom along the midplane plotted against the displacement of the wall; simulations for initial parameters (O), 4c_p (Δ), $c_p/4$ (∇) and $T_p=T_w$ (..) and visualisation experiments (--). a) t_d = 180 s.   b) t_d = 300 s.

Another assumption which certainly does not agree with the experimental conditions is the assumption that the pistons are insulated. To study the influence, the other limiting boundary condition, the temperature of the piston (T_p) equal to the wall temperature (T_w), is examined. The results *(Figure 3.11, Appendix V)* show that there is not much difference for the two limiting boundary conditions and thus this condition is assumed to have only a minor influence on the deformation patterns.

Simulations at larger displacements of the wall (50-100 mm) show *(Figure 3.12)* that the numerical model is able to predict patterns resembling those found in the experiments. It seems however that the influence of cure as seen for experiments performed with t_d=300 seconds, is not that obvious in the simulations.

It may be concluded that the simulations of the piston driven flow of reactive material with the numerical model and current material parameters, show qualitative agreement with the experiments. Furthermore the model is able to describe large displacements. Changing the boundary conditions has only a minor influence on the results. A quantitative agreement with the experimental results, could be achieved by re-examining the material parameters.
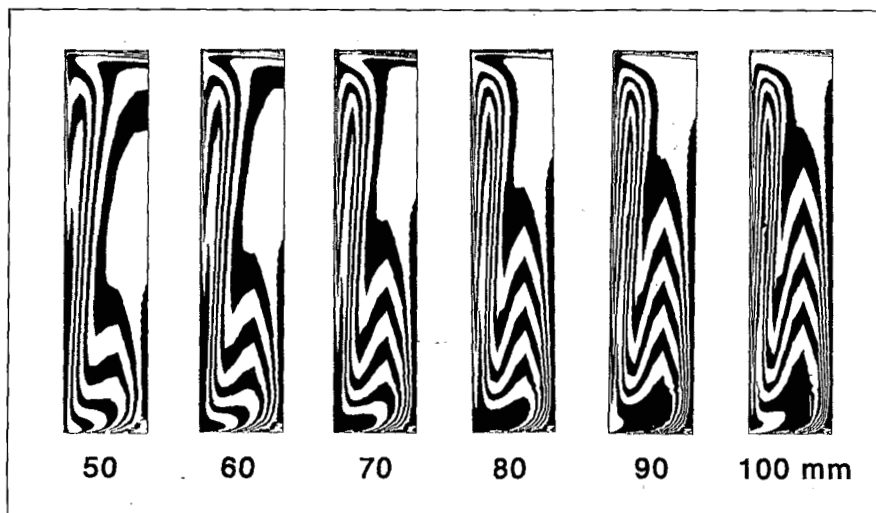
50	60	70	80	90	100 mm

Figure 3.12   Deformation patterns resulting from numerical simulations. T_w=100 °C; t_d= 300 seconds; v_w= 2 mm/s; displacements: 50, 60, 70, 80, 90 and 100 mm.

Re-examination

The rheological model is based on measurements of the dynamic viscosity. It is only assumed, and not yet tested, if the transformation of the viscosity model into a description of the steady state viscosity, is valid. The kinetic model determined for the material could be questioned as well, since no other measurements or techniques (IR-spectroscopy) could be performed to confirm the results. Furthermore, the use of the chemical gel point as a no-flow condition seemed questionable for this material (section 3.1.1). Therefore, in this part the simulations will be extended by varying the questionable material parameters.

In previous simulations the viscosity for shear rates smaller than 0.01 [s^{-1}] is set to the value of the viscosity at a shear rate of 0.01 [s^{-1}] ($\dot{\gamma}_{min}$) to prevent that the viscosity becomes infinite. It should be mentioned however that the measurements on which the description of the powerlaw behaviour is based were performed at a lowest effective shear rate of 0.25 [s^{-1}]. Therefore simulations are performed in which this value is changed to respectively 0.1 and 0.25 [s^{-1}]. All simulations are performed at t_d=300 seconds and a wall temperature of 100 °C.

The resulting deformation patterns of the simulations are submitted to *Appendix V*.

In *Figure 3.13* the vertical displacement of the material at the bottom along the midplane is plotted against the displacement of the wall, for the simulations performed. The simulations in which the Newtonian plateau is enlarged to higher shear rates does improve the resemblance between simulation and experiment. Following the trend in these results, in a rather crude way, simulations are performed (t_d=180, 300 s, T_w=100°C) in which the viscosity is no longer a function of the shear rate: the powerlaw coefficient n=0. This results in a further improved resemblance between simulations and experiments *(Figure 3.13)*. The deformation patterns are shown in *Figure 3.14*. The simulation performed at t_d=180 s shows that the viscosity model used describes too strong shear thinning behaviour for this material. It should be noticed, however, that the effect of shearthinning is observed in the experiments with different piston velocities *(Figure 3.7)*. The influence of cure, as in the visualisation experiments at t_d=300 s, is not found in these patterns.

To increase the influence of cure level, simulations are performed in which the conversion used in the viscosity model is doubled (2α). The resulting deformation patterns are submitted to *Appendix V*. The vertical displacements of the material at the bottom along the midplane, presented in *Figure 3.13* as well, shows that increasing the influence of cure on the viscosity does not result in a better agreement of the simulations with the experiments.
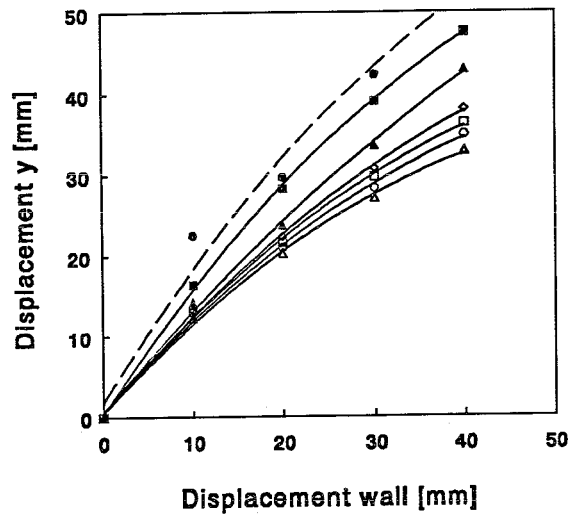
Displacement y [mm]

50
40
30
20
10
0

0   10   20   30   40   50

Displacement wall [mm]

Figure 3.13 The vertical displacement y of the material at the bottom along the midplane plotted against the displacement of the wall; simulations for variations in viscosity model (-): (O) initial viscosity model; (Δ) 2α; (□) $\dot{\gamma}_{min} = 0.1$ s^{-1}; (◊) $\dot{\gamma}_{min} = 0.25$ s^{-1}; (▲) $\eta = 1000$ Pa.s; (■) $n(\alpha)=0$; and visualisation experiments (--,●).

10   20   30   40 mm   10   20   30   40 mm

a.   b.
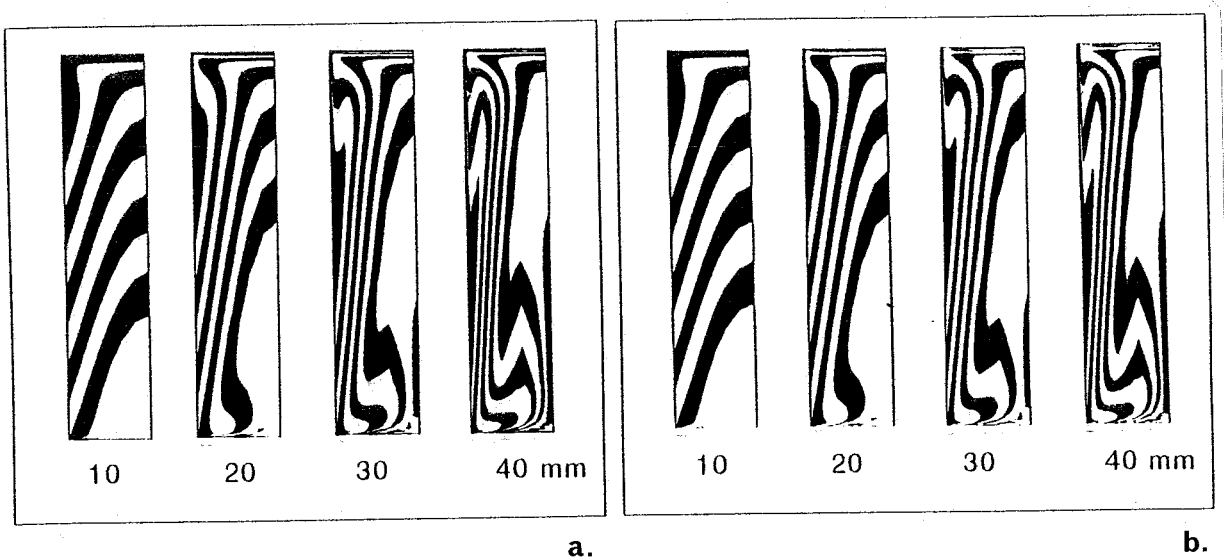
Figure 3.14 Deformation patterns resulting from numerical simulations performed with a viscosity model in which the powerlaw coefficient n = 0. $T_w=100°C$; $v_w= 2$ mm/s; displacements: 10, 20, 30 and 40 mm;(a) $t_d= 180$ s (b) $t_d=300$ s.

α-levels 1: 0.020
2: 0.024
3: 0.028
4: 0.032
5: 0.036
6: 0.040
7: 0.044
8: 0.048
9: 0.052
10: 0.056
11: 0.060

a.

T-levels 1: 373.00
2: 373.05
3: 373.10
4: 373.15
5: 373.20
6: 373.25
7: 373.30
8: 373.35
9: 373.40
10: 373.45
11: 373.50

b.
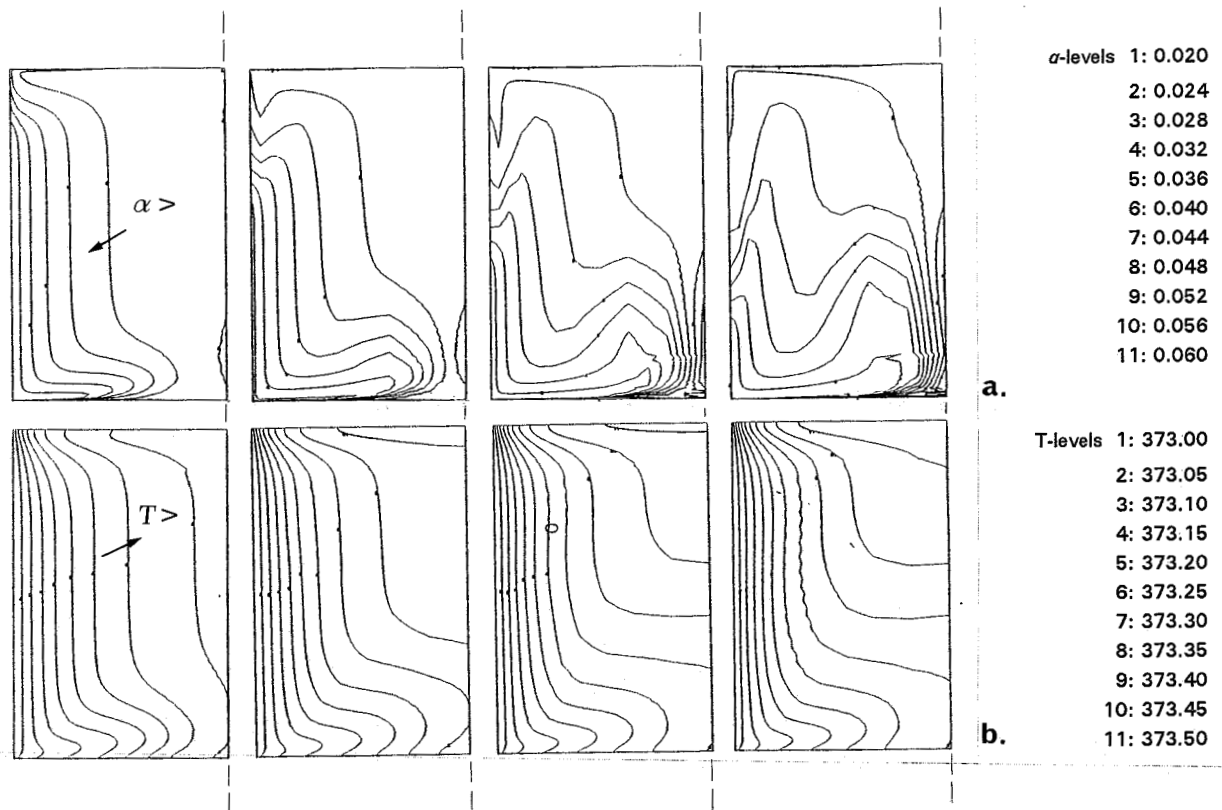
Figure 3.15   a) Conversion profiles b) Temperature profiles for the simulation performed at T_w=100°C; v_w= 2 mm/s; t_d=300 s; α_{gel}= 0.18; displacements of 10, 20, 30 and 40 mm.

α-levels 1: 0.020
2: 0.024
3: 0.028
4: 0.032
5: 0.036
6: 0.040
7: 0.044
8: 0.048
9: 0.052
10: 0.056
11: 0.060

a

T-levels 1: 373.00
2: 373.05
3: 373.10
4: 373.15
5: 373.20
6: 373.25
7: 373.30
8: 373.35
9: 373.40
10: 373.45
11: 373.50

b.

Figure 3.16   a) Conversion profiles b) Temperature profiles for the simulation performed at T_w=100°C; v_w= 2 mm/s; t_d=300 s; α_{gel}= 0.04; displacements of 10, 20, 30 and 40 mm.

3-19

Since it proved important to know the thermal conductivity coefficient (λ) and the heat capacity (c_p) more precisely, these coefficients are experimentally determined (section 2.5). The estimation of thermal conductivity coefficient (λ) appeared to be in agreement with the experimental value (0.7 [W/m.K]). The estimated value for the heat capacity (1000 [J/kg.K]) differed from the experimentally determined value: c_p=1400 [J/kg.K]. Simulations are performed using the measured values for these coefficients. Since the resulting deformation patterns show an improved resemblance *(Appendix V)*, the folllowing simulations are performed, using the experimentally determined value of the heat capacity.

From the visualisation experiments it was concluded that the use of the chemical gel point as a no-flow condition seems to be questionable for this material (section 3.1.1). Furthermore, in the conversion plot for the simulation performed with a delay time t_d=300 s, and T_{wall} = 100 °C, it is shown that the conversion at the wall does not reach the chemical gel point of 18 % *(Figure 3.15)*. In the corresponding visualisation experiments, however, the material at the wall seems to have reached the no-flow condition. Therefore, simulations are performed using a rheological gel point of 4% *(Figure 3.17)*.

The deformation patterns show that using the rheological gel point as a no-flow condition results in a more quantitative agreement between the simulations and the experiments. At the wall the material, that has reached the gel point does not flow, resulting larger displacements of the material at the centre of the cylinder.
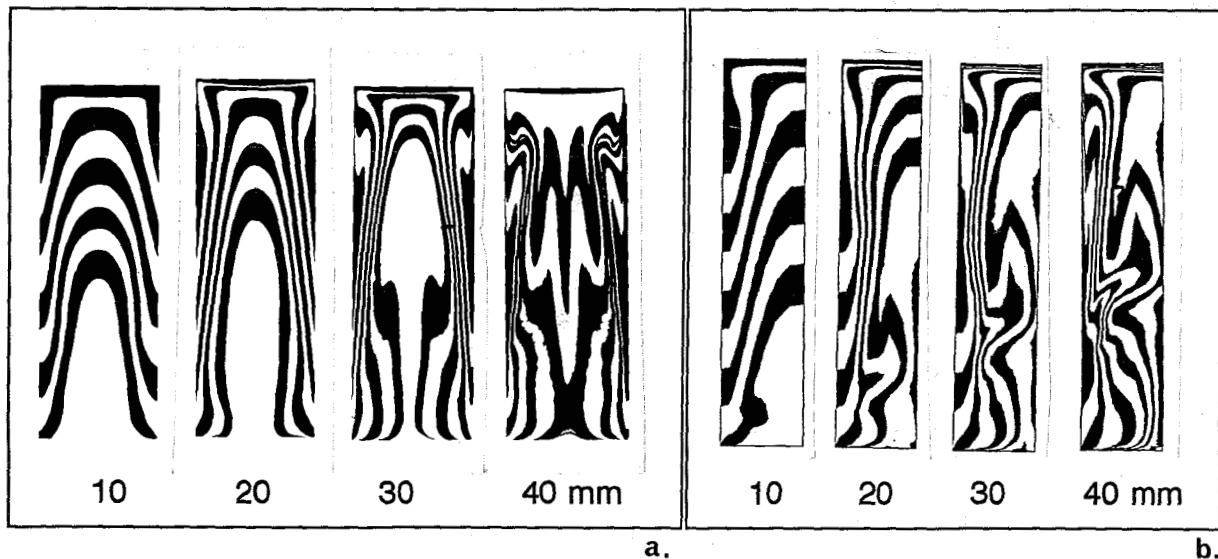
Figure 3.17   Deformation patterns : a) visualisation experiment b) numerical simulation; T_w=100°C; v_w= 2 mm/s; displacements: 10, 20, 30 and 40 mm; t_d=300 s.

Furthermore, the reverse fountain flow region at the driving piston is broadened, which agrees well with the experimental results. The patterns resulting from these simulations are disturbed by a division of the first material (white coloured) that flows into the reversed fountain flow, into two regions (in *Figure 3.17*: 1,2).

The conversion- and temperature profiles resulting from the simulations performed with α_{gel}=0.18 and 0.04, are compared in *Figure 3.15* and *Figure 3.16*. The conversion profiles from simulations performed with α_{gel}=0.04 show much larger gradients which can result in numerical problems. This is confirmed by simulations performed which could not be completed. The temperature profiles with α_{gel}=0.04 show locally larger gradients as well. Due to higher viscosities the Brinkman number is increased *(Appendix IV)*. Viscous dissipation becomes more important, leading to a temperature rise which causes an acceleration of the reaction, and thus a further increase of the temperature. It should be mentioned however, that the temperatures found at the pistons will be decreased when more realistic boundary conditions are chosen.

3.1.3   Conclusion

The experiments show that the deformation patterns of the piston driven flow for a reactive material are successfully visualised. Due to the occurrence of slip at low levels of cure, the temperature range for experiments showing no slip is limited to relatively low temperatures or short delay times. Consequently, the Damköhler IV number is relatively low. The use of the chemical gel point as a no-flow condition seems to be questionable for this material.

The numerical simulations performed with a first set of material parameters show a good qualitative agreement with the experiments. More precise determination of the parameters lead to a more quantitative agreement, although improvement is still needed. It appears that the shearthinning behaviour, determined by dynamic measurements, is too strong. The combination of visualisation experiments and numerical simulations seems to be useful for an iterative determination of the rheological behaviour of the reactive material. The definition of a rheological gel point proved to be important towards a more quantitative description of the flow.

3.2 The Moulding Process

The goal of this section is to study the performance of a commercial multiplunger process, used for IC-encapsulation, by means of visualisation of the flow. In this process each plunger provides two cavities with reactive material. The flow is visualised by using different coloured slices of the same material. In section 3.2.1 the flow in an empty two-cavity mould is studied (no leadframe is present). The flow into a one-cavity mould containing a leadframe is studied in section 3.2.2. Therefore, in a two-cavity geometry one of the cavities is closed. In section 3.2.3 concluding remarks are made and some suggestions for an improved process design given.

3.2.1 Two Cavities without a Leadframe

The experiments to visualise the flow in a two-cavity mould are performed in the laboratory transfer moulding press at ASM-Fico (Herwen). In *Figure 3.18* the geometry of the mould and the transfer pot is given. A stack of epoxy moulding compound ($\varnothing$ 14 mm) with a height of 35 mm is put in the transfer pot automatically and heated for 3 seconds at a temperature of 180°C. The diameter of the transfer pot is larger than 14 mm so the stack can slide easily into the pot. After the mould is closed the compound is forced through the runners into the cavities by moving the plunger upwards at a velocity of 3 mm/s.
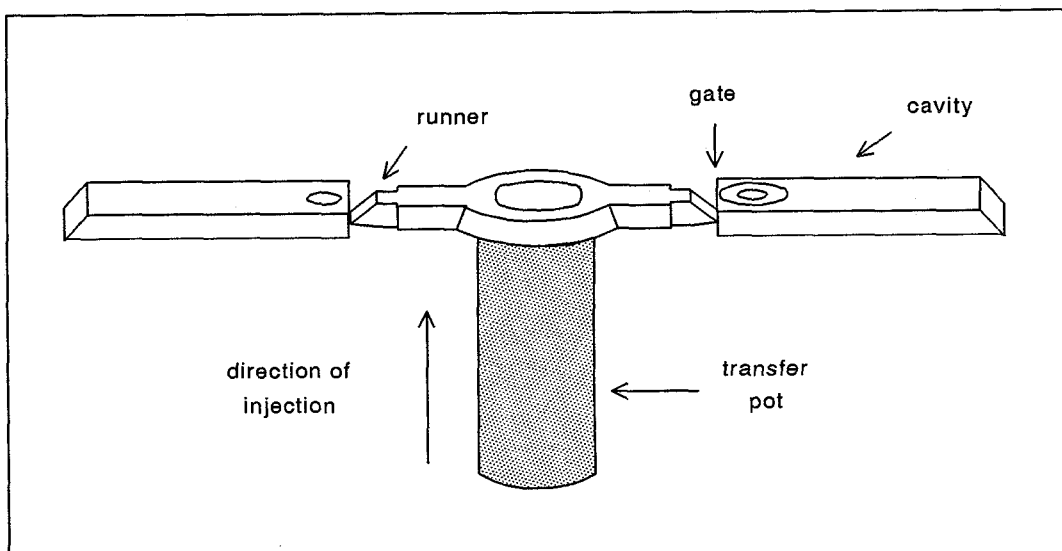
Figure 3.18   Geometry of two-cavity mould and the transfer pot.
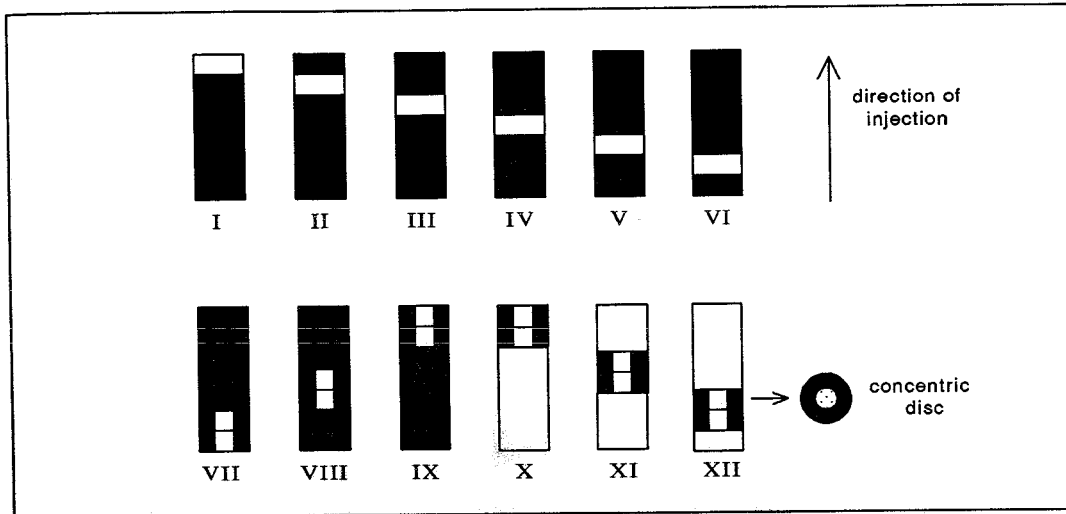
Figure 3.19 Composition of black/white stack, used in the visualisation experiments.

The position of the black and the white compound in the stack is different for each experiment performed *(Figure 3.19)*. For experiment VII-XII some concentric discs were used. Short shot experiments are performed, using the same amount of material, but a smaller displacement of the plunger. These experiments showed that, for the given process conditions, no jetting occurred during filling.

For the evaluation of the experiments the product in one cavity is examined by studying the cross sections in the direction of the flow. The product in the other cavity is examined by studying the cross sections perpendicular to the flow direction. In *Figure 3.20* the cross sections are indicated.

a. Lengthwise cross-section   b. Cross-section
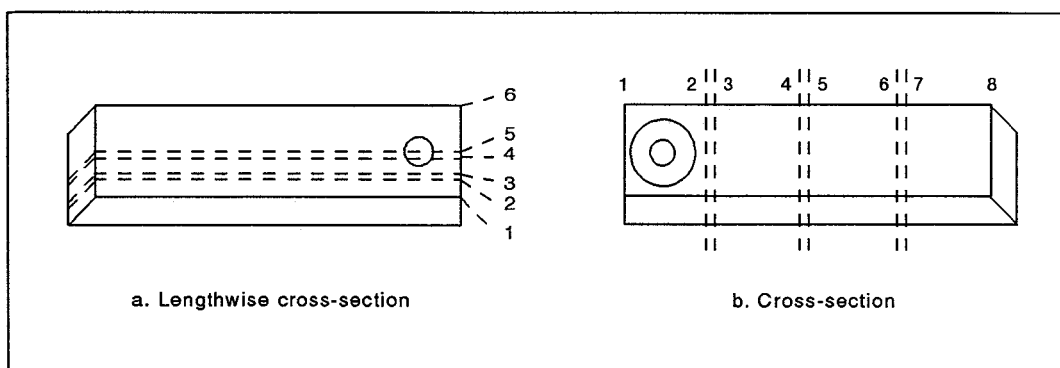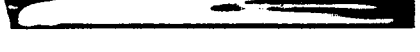
Figure 3.20 Cross sections of the products studied.

IV 6 5 4 3 2 1 ←

III 6 5 4 3 2 1 ←

II 6 5 4 3 2 1 ←

I 6 5 4 3 2 1 ←
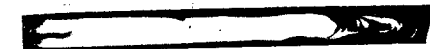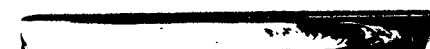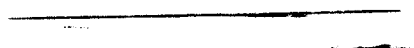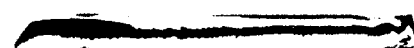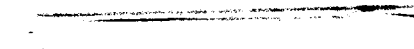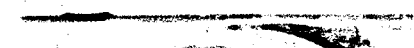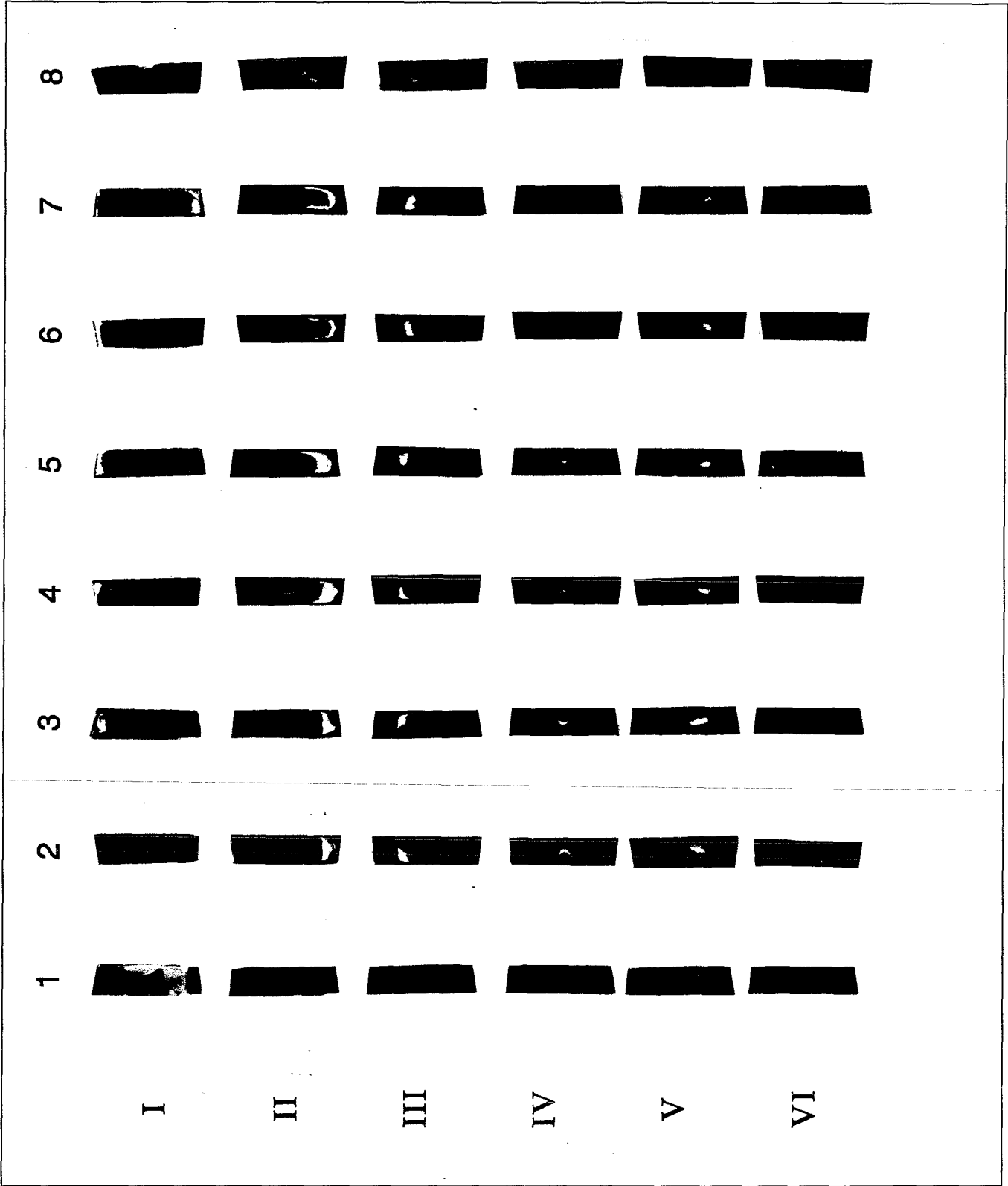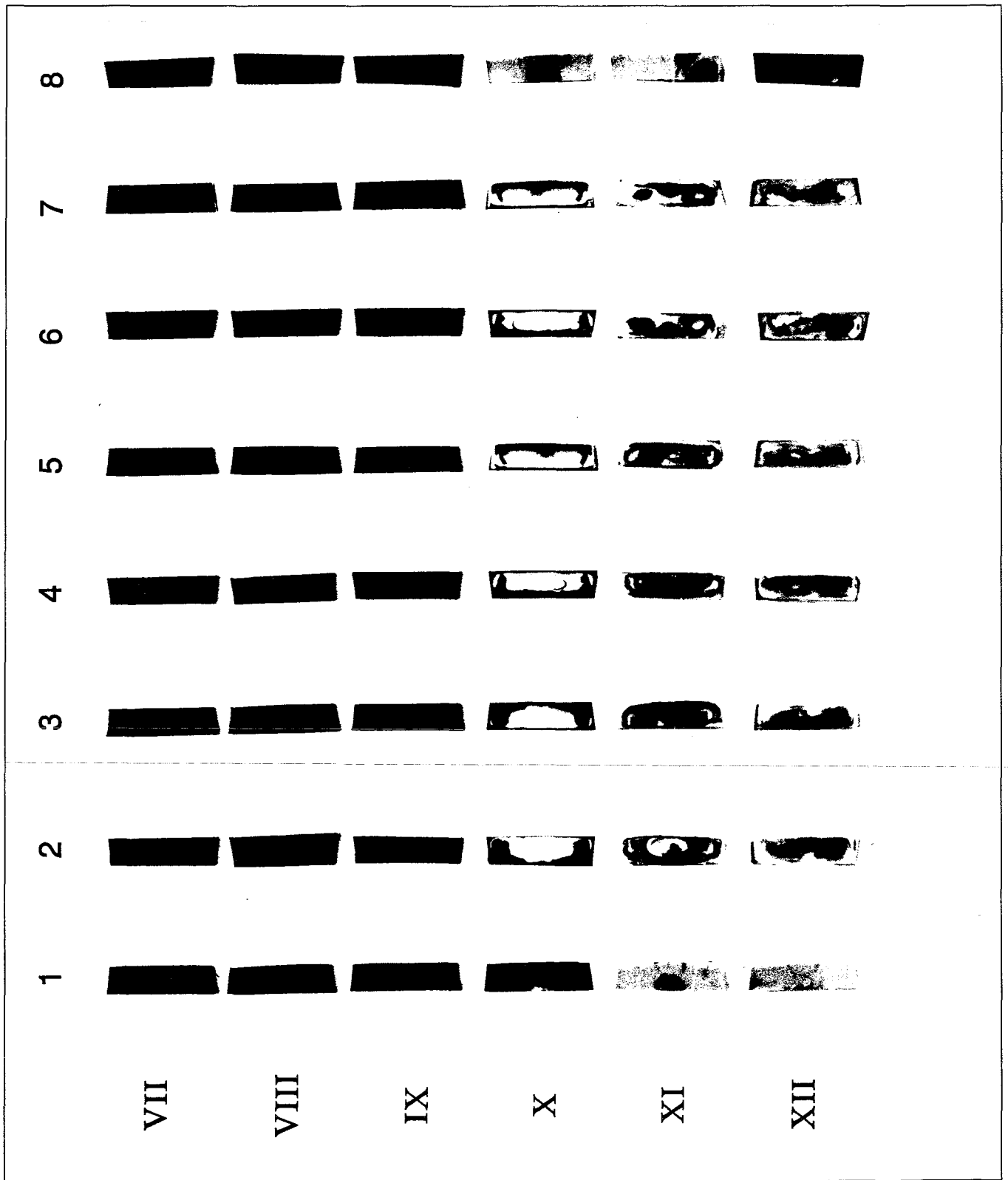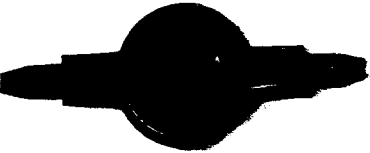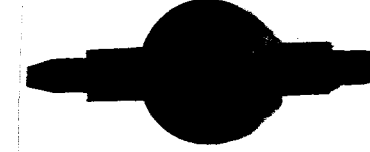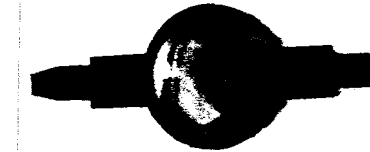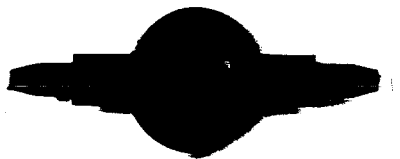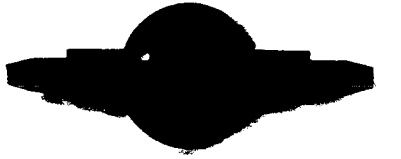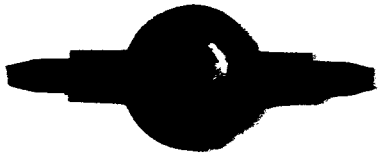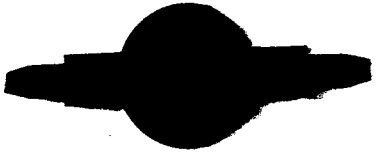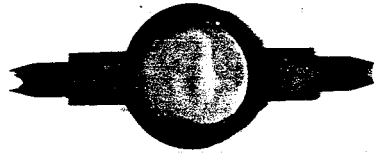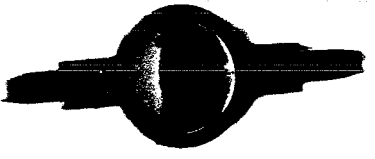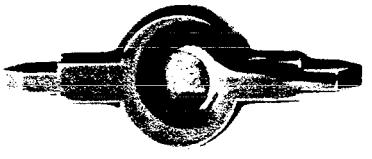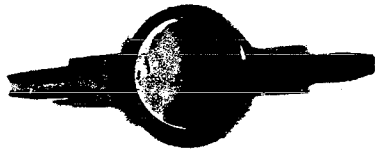
upper side　　　　　　　　　plunger side

I		I	
II		II	
III		III	
IV		IV	
V		V	
VI		VI	

upper side   plunger side

VII		VII	
VIII		VIII	
IX		IX	
X		X	
XI		XI	
XII		XII	

A-24

Appendix VII : Visualisation Experiments: One Cavity with a Leadframe

In this Appendix the cross sections are given for the experiments XIII to XVII (Figure AVII). The numbers correspond to those in these figures.

a.

b.
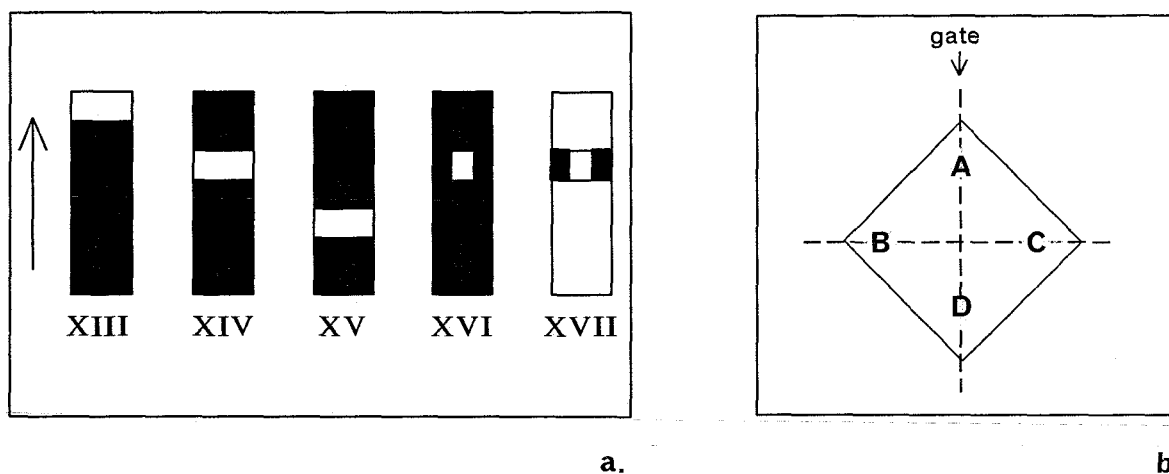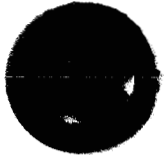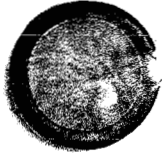
Figure AVII   a) Composition of the stacks of black and white compound.
b) Cross sections.
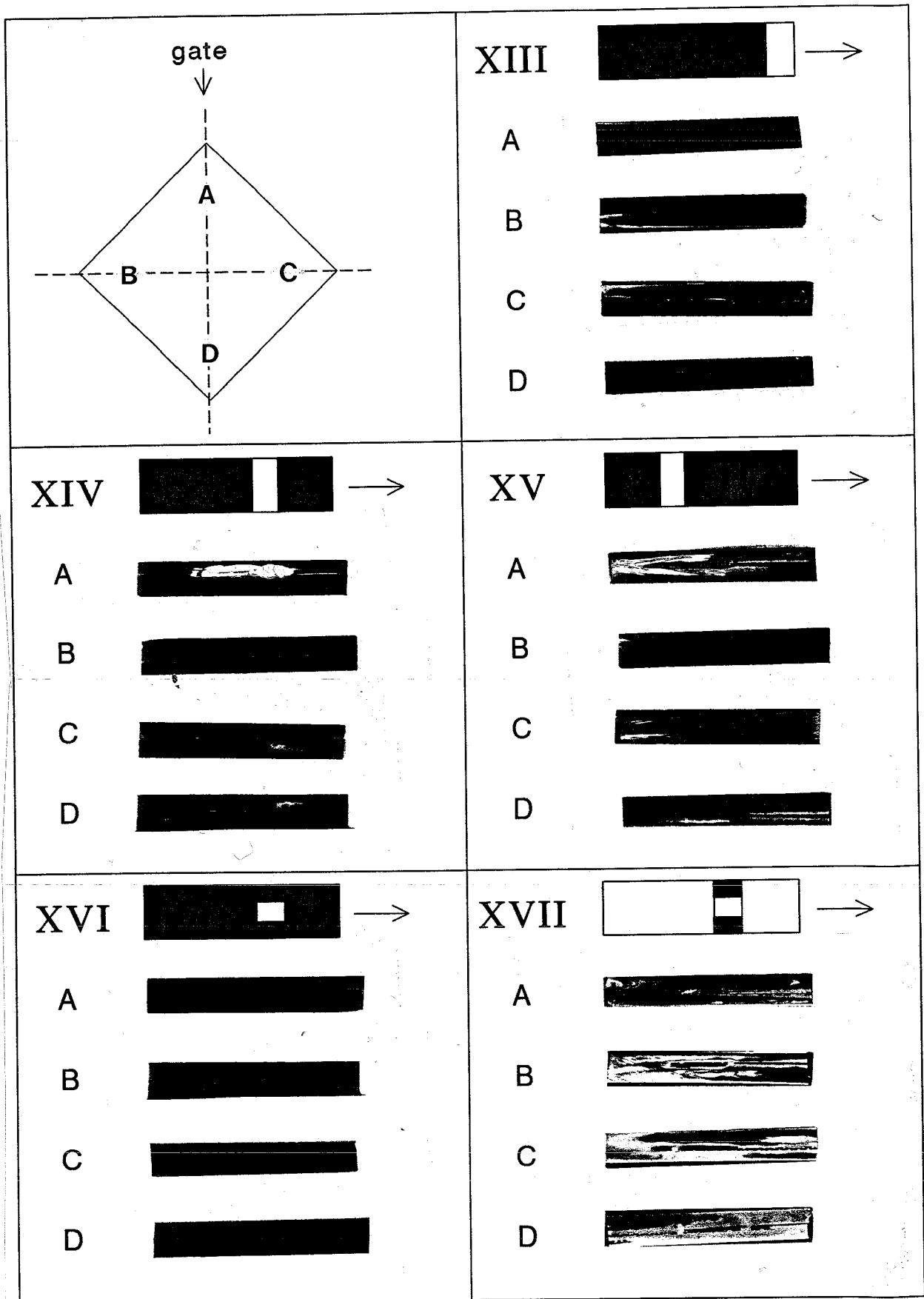
The cross sections are positioned with the middle of the product at the right side.

upper side   plunger side

XIII		XIII	
XIV		XIV	
XV		XV	
XVI		XVI	
XVII		XVII	
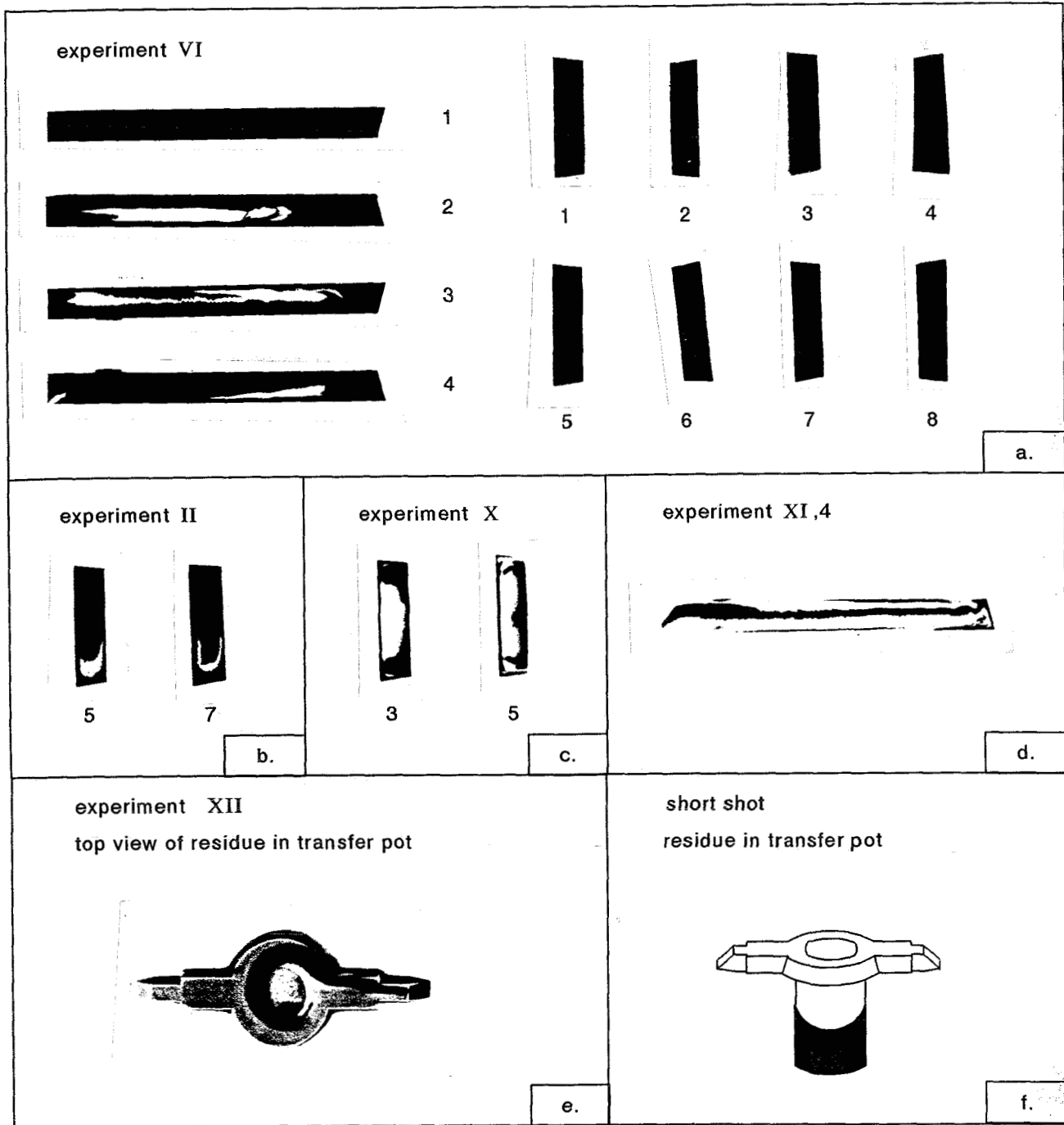
Figure 3.21 Resulting deformation patterns, for a one pot/two cavity configuration. (a): Asymmetric filling shown by experiment VI. (b): Asymmetry in experiment II. (c): Symmetry and asymmetry in experiment X. (d): Asymmetric patterns in the vertical direction in the cavity in experiment XI. (e): Asymmetry in the short shot residue in transfer pot.

The results of the experiments are submitted to *Appendix VI*. It is shown that generally the first material entering the cavity, is positioned at the outer side of the product. It appears however that the left and the right cavities are not filled identical. An example of the asymmetric filling is given in experiment VI. The lengthwise cross sections of the left product show clearly white material within the product while in the cross sections of the right product no white material is detected *(Figure 3.21a)*. Symmetry as well as asymmetry occurs in the direction perpendicular to the flow direction. Examples are given in *Figure 3.21b,c* showing the cross sections of experiment II and experiment X, thus questioning the reproducibility of the experiments. Asymmetric patterns in the vertical direction in the cavity are expected since the position and shape of the gate is asymmetric as well. These asymmetric are indeed detected as for example in experiment X and XI *(Figure 3.21c,d)*. The asymmetric filling in the direction perpendicular to the flow direction, and the non-identical filling of the cavities can be seen as well in the flow patterns found in the residue of material in the transfer pot and runners. It appears that the transfer pot is decisive for the filling of the cavities. The material heated at the walls of the transfer pot and piston can enter the mould earlier than the material in the middle of the pot. Furthermore when short shots are performed injecting first white and then black material, the material left in the transfer pot is deformed asymmetrically *(Figure 3.21e,f)*. It is thought that the filling behaviour of this process is mainly not controllable due to badly defined heating of the material in the transfer pot, mainly caused by the initial space between material and the wall of the transfer pot, and not due to the division of the flow over the two cavities. Visualisation of the flow in one pot / one cavity configuration, as described in the next section, may support this idea.

3.2.2 One Cavity with a Leadframe

As a consequence of these experiments, the visualisation of the flow into a mould containing a leadframe, are performed with a two-cavity mould in which only one cavity is used by blocking one gate *(Figure 3.22)*.

The geometries of the stacks, consisting of the black and white compound, used in the experiments are given in *Figure 3.23*. Short shots are performed, using a smaller amount of material. The square products are studied by examining the cross sections in flow direction and perpendicular to the flow direction *(Figure 3.24)*.
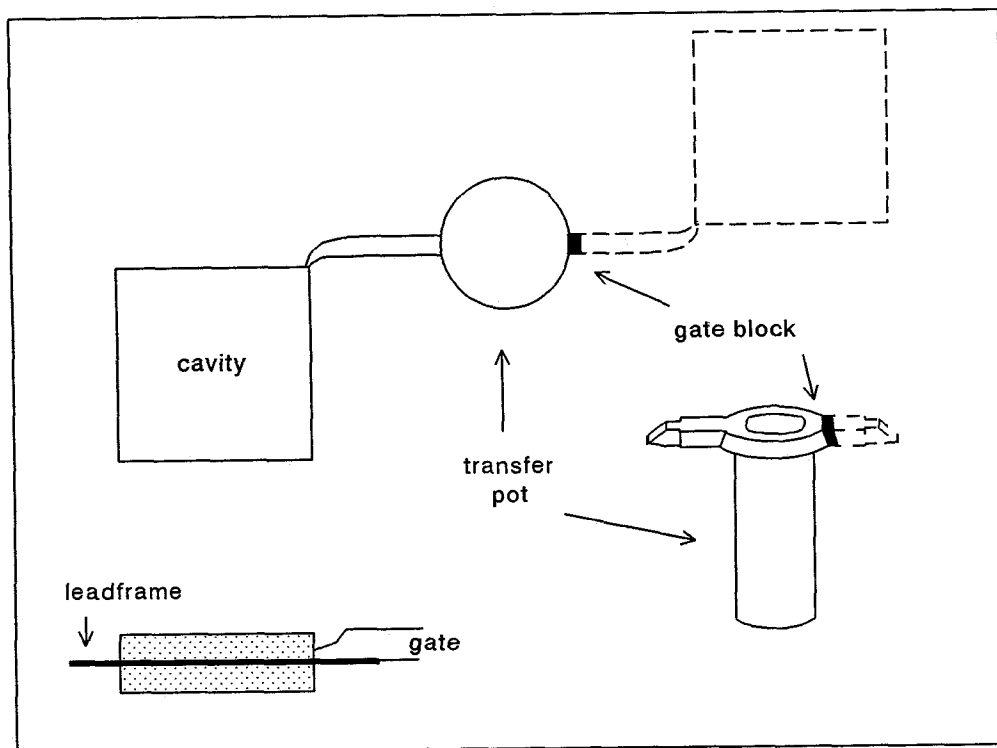
Figure 3.22 Geometry of the two-cavity mould with one cavity blocked.

The results of all experiments are submitted to *Appendix VII*. From the short shot experiments it appeared that the flow front below the leadframe runs ahead of that above the leadframe *(Figure 3.25a)*. Experiment XIII confirmed that the cavity is filled earlier below the leadframe since the white material is found at the upper outside of the cavity and not at the other side. This is not surprising since the geometry of the gate is asymmetric. This is however not a desirable phenomenon since it leads to forces on the leadframe which can cause large leadframe displacements or even severe damage (section 1.3). Usually these flows are

balanced by changing the design of the gate. These experiments show that no flow through the leads occurs during filling, given a specific geometry of the leadframe. The spaces above and below the leadframe are filled separately until one side is completely filled.

Comparison of the cross sections B and C of experiment XVII *(Figure 3.25b)* shows that the cavity is filled asymmetric in the direction perpendicular to the flow direction. The residues in the transfer pot of experiment XV shows asymmetry as well *(Figure 3.25c)*. Furthermore, repeating the experiment with stack geometry XIV, shows that the experiment is not reproducible *(Figure 3.25d)*. It appears that the heating in the transfer pot is uncontrollable, leading to asymmetric patterns and no reproducible products.

It should also be noticed that the material particles supplied to the cavity have very different histories and thus very different rheological properties. This also reduces the controllability of the process.
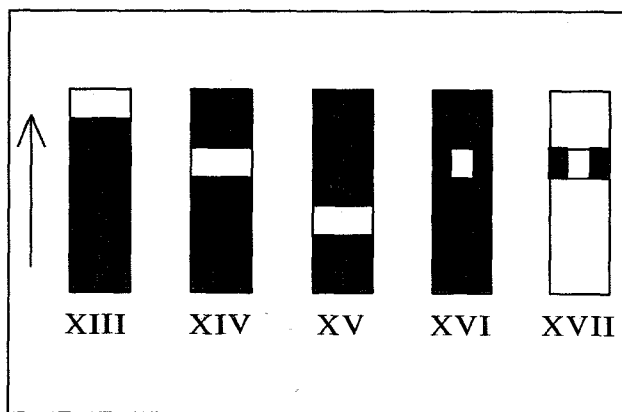
Figure 3.23 Composition of black/white stack, used in the visualisation experiments.
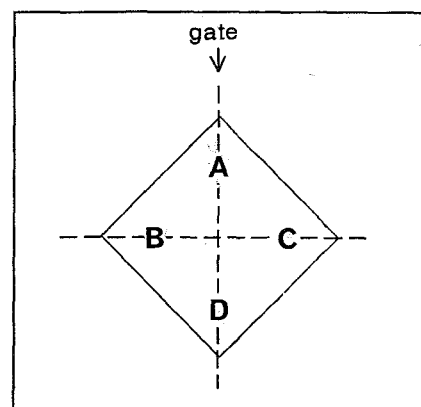
Figure 3.24 Cross sections of the products studied.

3.2.3 Conclusion

The results show that for both configurations asymmetry is found in the products in all directions. The asymmetric patterns in vertical direction, leading to unbalanced flows above and below the leadframe, should be controlled by the design of the gate. Asymmetric filling of the two cavities, and in the direction perpendicular to the flow (horizontal) appears to be caused by asymmetric heating in the transfer pot. This could be due to the fact that the diameter of the stack is smaller than the

diameter of the pot to allow for easy supply of material. The material is therefore, initially, not fully in contact with the wall in the transfer pot.

Furthermore it is shown that heating the material at the wall of the transfer pot allows material at the wall to flow into the mould before material which is positioned in the middle of the stack. This flow process seems to be difficult to control.

To obtain reproducible products a more controlled process is desired. To use this process for a multilayer concept control of the process is even a necessity. The reproducibility of the process can be improved when only one transfer pot is used to supply one cavity. A more controlled process could be obtained by heating the material only at the mould, keeping the transfer pot cold, and decreasing the (short) preheating time to zero. Following this procedure it is guaranteed that the material entering the mould is keeps constant in temperature and degree of reaction.
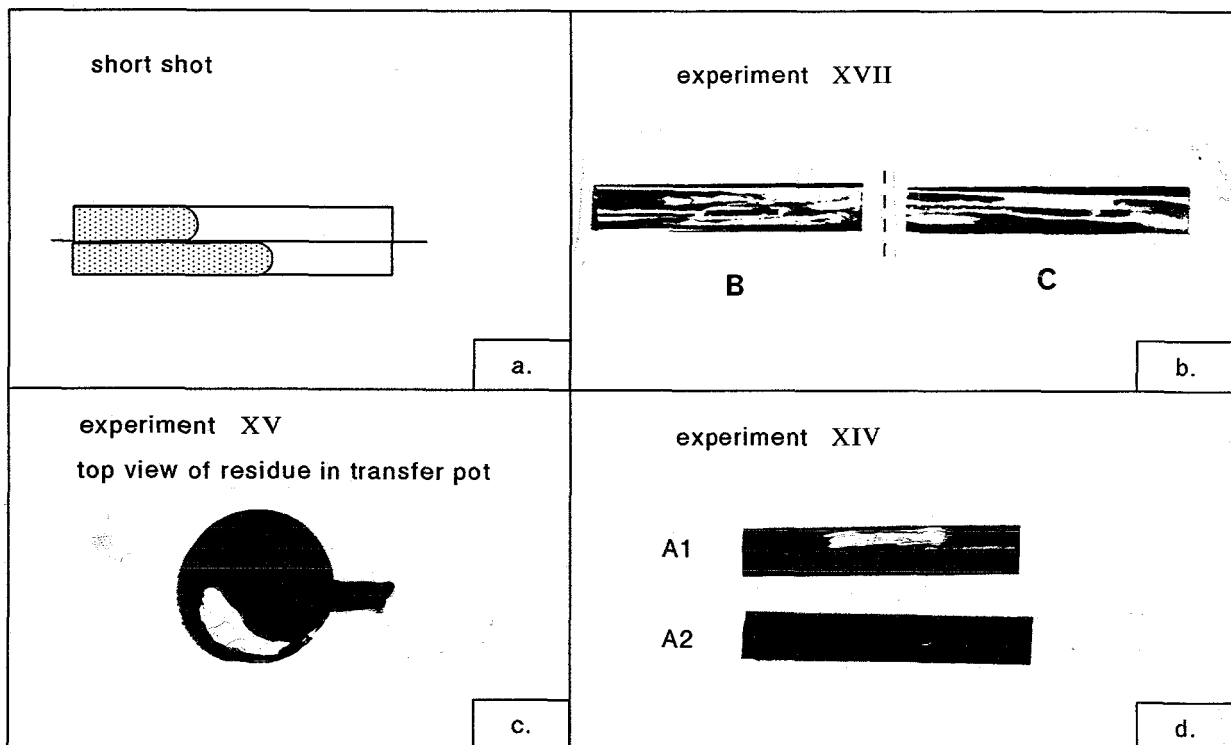
Figure 3.25   Results of visualisation experiments with one cavity. (a): Side view of product obtained using short shot. (b): Asymmetry above and below leadframe showed by experiment XIII. (c): cross sections B and C of experiment XVII. (d): residues in the transfer pot of experiment XV. (e): repeated experiment with stack geometry XIV.

3.3 Improved Moulding Process

The visualisation experiments performed in a practical moulding process (section 3.2) showed that a more controlled process is desired to obtain reproducible products. In this section an improved process is described and experimentally tested.

3.3.1 The Improved Process Design

For the improved process the one pot / one cavity concept is chosen, to prevent problems of balancing the two flows over different cavities. The transfer pot is designed with a diameter equal to that of the stack of material to be supplied, to avoid asymmetric heating in the transfer pot.

The transfer pot is kept cold, so heating of the material takes place only at the mould. This has the important advantage that the material entering the mould is constant in temperature and conversion.

The mould used in this process is cylindrical with a rectangular cavity in the centre *(Figure 3.26)*. The mould is heated, using eight heating elements placed in vertical direction around the cavity. To record temperature and pressure during filling, a thermocouple and a pressure gauge is placed at the runner. Closing the mould, the cavity is blocked on the dumbar of the leadframe. The closing pressure is provided, using a eccentric clamp *(Figure 3.27)*. The temperature of the mould is controlled by a thermoregulator, connected to a thermocouple which can be placed at different positions in the mould. On top of the mould, around the heating surface, insulation material is mounted, to avoid excessive heating of the pot during the filling stage of the process.

The mould, the transfer pot and the plunger are mounted in a transfer press *(Figure 3.28)*. The plunger and the mould can be moved up- and downwards. At the start of the moulding process, the heated mould is not in contact with the transfer pot, to prevent heating of the transfer pot. The stack of material is placed in the pot. The mould is then placed against the transfer pot. The material is pressed against the heated mould and the melted material is directly transferred into the mould by moving the plunger downwards *(Figure 3.29)*. During the curing time, the mould is moved away from the pot, allowing to supply the pot of new material for the next product.

Figure 3.26   Open mould with an improved geometry, showing the cavity, the leadframe, the
               runner and the heating surface.

Figure 3.27   Closed mould with an improved geometry.

Figure 3.28 Set-up before transferring the material into the mould.

Figure 3.29 Set-up after transferring the material.

3.3.2 Visualisation Experiments

Experiments are performed with the improved process to encapsulate a commercial leadframe, using two compounds which only differ in colour. The temperature of the mould is set to 170 °C. The plunger speed used is 2 mm/s.

A short shot experiment was performed to assure that no jetting occurred for the given process parameters. The configuration of the stacks of material used in the experiments are given in *Figure 3.30*. The choice of configurations was a first trial, based on minor experience, aimed at a multilayer encapsulation of the leadframe (black on the outside; white at the leadframe surface). Both configurations are applied twice; the first product is examined by studying the middle cross section in direction of the flow, the second product by studying some cross sections perpendicular to the flow direction.

The resulting flow patterns arising along the midplane *(Figure 3.31)*, show that the flow above and under the leadframe is not identical. This is probably caused by the position of the die pad of the leadframe, which is not centred.

Examination of the cross sections perpendicular to the flow direction shows that in that direction a symmetric pattern is obtained *(Figure 3.31b, 3.32)*.

From the results of experiments performed with configuration A, it appears that the first material entering the mould (black) is situated in the product at the outer surface as well as at the leadframe surface. The results from experiments using configuration B show that a multilayer encapsulation is almost achieved. In future the encapsulation configuration should be improved through a prediction of the stack configuration in the transfer pot by means of numerical simulations (section 3.1).
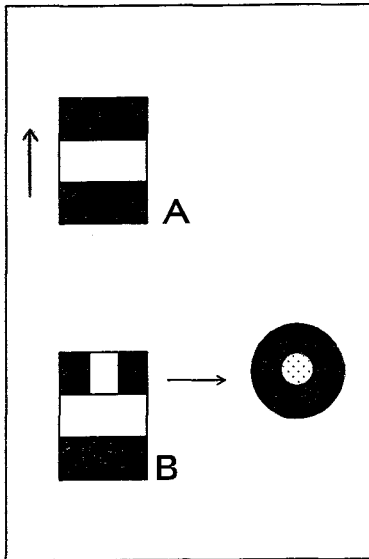
Figure 3.30 The configuration of stack, composed of black and white material, used for flow visualisation.

Figure 3.31 a) Cross sections along the midplane for stack configuration A (above) and configuration B (below). b) Symmetric pattern in cross section perpendicular to the flow direction.

Figure 3.32 Cross section perpendicular to the direction of flow for stack configuration A (left) and B (right).

3.3.3   Conclusion

A controllable encapsulation process is designed, that proved to result in a symmetric filling (in cross direction) of the cavity. More experiments are necessary to confirm the reproducibility of the process. With such a controllable process it should be possible, with slight adjustments to the configuration of the stack of material, to achieve a multilayer encapsulation.

A major advantage of the designed process is the fact that the material entering the mould is constant in temperature and conversion, resulting in constant rheological properties. For the transfer moulding process studied in sections 3.2.1 and 3.2.2 the material particles entering the mould differed greatly in their history and thus their rheological properties. In such a process there is the need of a broad processing window, with respect to viscosity. For the improved design a much smaller processing window would be convenient, allowing the use of faster reaction compounds.

4 Conclusion

This study served the development of a technology that allows for IC-packaging with two or more components, in order to obtain a multilayer encapsulation. The predictive capability of numerical tools for the simulation of reactive flow of an epoxy compound, used in the encapsulation of IC's, was tested by using a combination of experiments and numerical analyses. The results showed a good qualitative agreement, and lead to new insight in the rheological properties of the used compound.

Since an adequate description of the chemorheological behaviour of the moulding compound is of the utmost importance, the reaction kinetics and the viscosity as a function of temperature, shear rate and conversion were determined with great care.

For the realisation of a multilayer technique a reproducible and controllable transfer moulding process should be available. Therefore the process was studied in a practical two cavity mould by visualisation experiments. Since the process proved to be uncontrollable, an improved design is suggested and studied.

The highly filled fast curing epoxy compounds were characterized to obtain the material properties needed for the numerical simulations.

A description of the reaction kinetics is obtained by fitting the parameters of a autocatalytic kinetic equation on data obtained by dynamic DSC experiments. Recalculations to check the fit gave satisfactory results.

Since it was impossible to measure the steady state viscosity of these compounds, a strategy was proposed, based on measurements of the dynamic viscosity, to find an expression relating viscosity to temperature, shear rate and degree of reaction. An equivalence is assumed between the steady state viscosity, measured at a certain shear rate, and the dynamic viscosity measured at an effective shear rate (i.e. the product of frequency and strain) equal to that shear rate. It appeared that at a constant value of the effective shear rate the dynamic viscosity is identical over a wide range of frequencies and strains. To study the influence of cure on the viscosity the conversion during the DMTA-experiments was calculated, using the kinetic equation. The effective shear rate dependence is described with a powerlaw with an exponent that depends on the conversion. The effect of temperature is described with an Arrhenius-type with conversion dependent parameters. The description of the viscosity gave a good prediction of the measured viscosity in the region between melting and gelling of the compound.

The gel point of the epoxy compound is studied using extraction experiments, and

by examining the viscoelastic properties near the gel point. The extraction of the soluble content of samples, cured for different times, resulted in a gel point of 18 % conversion. Examining the theories proposed in literature to detect the gel point from dynamic experiments, it is observed that neither the G'-G" crossover (Tung and Dynes) or the frequency-independency of tan(δ) (Winter) can be used to determine the gel point of the given material. However, the curves of G' against conversion for measurements performed at an equal maximum strain appear to converge at a conversion of approximately 18 %, which agrees with the gel point determined through extraction experiments.

In order to test the predictive capability of the numerical model, the piston driven flow was chosen since this flow meets some important requirements and has some decisive advantages. The deformation patterns were experimentally visualised using different coloured slices of the same material. Due to the occurrence of slip at relatively low levels of cure, the temperature range for experiments showing no slip was limited to relatively low temperatures or short delay times. Consequently, the Damköhler IV number was relatively low, leading to experiments which were not as discriminating with respect to the cure level as wished for.
These experiments showed that the use of the chemical gel point as a no-flow condition seems questionable for this material.
The piston driven flow of the reactive material was numerically simulated, using a finite element package which includes a particle tracking algorithm, enabling a direct confrontation of numerical results with the visualisation experiments.
With a first set of material parameters, a good qualitative agreement was obtained with the experiments. More precise determination of the parameters lead to a more quantitative agreement, although improvement is still needed. It appeared that the shearthinning behaviour, determined by dynamic rheological experiments, is too strong. The combination of visualisation experiments and numerical simulations seems to be useful for an iterative determination of the rheological behaviour of the reactive material. The definition of a rheological gel point proved to be important towards a more quantitative description of the flow.

A practical transfer moulding process with a two cavity mould was studied by visualisation experiments. The results showed that a non-reproducable asymmetry is found in the products in all directions. One of the main reasons is the asymmetric heating in the transfer pot, due to the initial space between the material and the walls of the transfer pot. Furthermore, it is shown that heating of the material at the walls results in material entering the mould with strongly varying, unknown properties. Therefore an improved process was designed and studied in which the material is only heated at the mould, keeping the transfer pot cold.

Following this procedure, the material entering the mould is kept constant in temperature and degree of reaction. Since the rheological properties of the material can be controlled in this way, it is possible to use a narrow processing window, allowing the use of faster reacting compounds.

Since the modelling of the viscosity by means of a powerlaw is the most simple one, in future work other, more complex viscosity models should be examined. It would be desirable to find a method to validate the transformation of the model for the dynamic viscosity into a model for the steady state viscosity. Capillary viscometry combined with numerical simulations could be used to test this transformation.

More insight is needed with respect to the definition of a rheological gel point. Dynamic measurements did not show the occurrence of such a gel point, therefore other experiments should be developed to examine this phenomenon.

Visualisation experiments of the piston driven flow should be performed using conditions and a geometry that allows for more discriminating experiments. The numerical simulation of the piston driven flow should be extended, using more realistic boundary conditions.

Since wall slip appeared to occur at a low level of cure, it would be useful to implement slip into the numerical model. Piston driven flow might be a useful experimental method to quantify the wall slip phenomenon.

Since the simulations in the piston driven flow give satisfactory results, the simulation of the reactive flow into a mould should be performed, providing a first estimate of the stack configuration in the transfer pot, in order to obtain a multilayer encapsulation of an integrated circuit.

5 References

1 D.S. Soane and Z. Martynenko, Polymers in Microelectronics: Fundamentals and Applications, Elsevier Amsterdam (1989)

2 A. Hale, Epoxies Used in the Encapsulation of Integrated Circuits: Chemistry, Rheology, Glass Transition and Reactive Processing, PhD thesis, Univ. Minnesota (1988)

3 L.T. Manzione and D.J. Lando, Polymers in Electronics Packaging, AT&T Techn. J., nov/dec, p.60 (1990)

4 I.C. Noyan and L.T. Nguyen, Residual Stresses in Polymeric Passivation and Encapsulation Materials, Pol. Eng. Sci., 28, 1026 (1988)

5 F. van Eldijk, Optimization of IC packaging, Nat.Lab. report 6490, (1990)

6 N. Kinjo, M. Ogata, K. Nishi and A. Kaneda, Epoxy Moulding Compounds as Encapsulation Materials for Electronic Devices, in Advances in Polymer Science 88, Springer-Verlag (1989)

7 Dubois, Encyclopedia of Plastics Equipment, Ed. H.R. Simonds (1964)

8 D. Rosato and D.V. Rosato, Plastics Processing Handbook, Nostrand Reinhold, New York (1989)

9 L.L. Blyler Jr., H.E. Bair, P. Hubbauer, S. Matsuoka, D.S. Pearson, G.W. Poelzing, R.C. Progelhof and W.G. Thierfelder, A New Approach to Capillary Viscometry of Thermoset Transfer Moulding Compounds, Pol. Eng. Sci., 26, 1399 (1986)

10 L.T. Nguyen, Wire Bond Behavior During Molding Operations of Electronic Packages, Pol. Eng. Sci., 28, 926 (1988)

11 L.T. Nguyen and I.C. Noyan, X-Ray Determination of Encapsulation Stresses on Silicon Wafers, Pol. Eng. Sci., 28, 1012 (1988)

12   T. Hattari, S. Sakata, T. Hatsuda and G. Murakami, A Stress Singularity Parameter Approach for evaluating Adhesive Strength, JSME Int. J., Ser.I, Vol.31, No.4, p718-723 (1988)

13   A. Hale, M. Garcia, C.W. Macosko and L.T. Manzione, Spiral Flow Modelling of a Filled Epoxy-Novolac Molding Compound, Proc. ANTEC, 796 (1989)

14   T.H. Hsieh and A.C. Su, Cure Kinetics of an Epoxy Novolac Molding Compound, J. Appl. Polym. Sci., 41, 1271 (1990)

15   M.E. Ryan and A. Dutta, Kinetics of Epoxy Cure: A Rapid Technique for Kinetic Parameter Estimation, Polymer, 20, 203 (1979)

16   M.R. Kamal and S. Sourour, Kinetics and Thermal Characterization of Thermoset Cure, Pol. Eng. Sci., 13, 59 (1973)

17   R.B. Prime, in Thermal Characterization of Polymeric Materials, E.A. Turi, Ed., Academic, New York (1981)

18   W.P. Cox and E.H. Merz, J. Polym. Sci., 28, 619 (1958)

19   M.B. Roller, Rheology of Curing Thermosets: A Review, Pol. Eng. Sci., 26, 432 (1986)

20   T. Kitano, T. Nishamura, T. Kataoka, T. Sakai, Correlations of Dynamic and Steady Flow Viscosities of Filled Polymer Systems, Rheol. Acta, 19, 671 (1980)

21   D.M. Bigg, Rheological Behavior of Highly Filled Polymer Melts, Pol. Eng. Sci, 23, 206 (1983)

22   D. Doraiswamy, I.-L. Tsao, S.C. Danforth, A.N. Beris, A.B. Metzner, The Rheology of Ceramic Suspensions, Proc. Xth Int.Congress on Rheology, 1, 300 (1988).

23   B.J. van den Brule, J.F. Dijksman and P.J. Zander, Rheometry of Viscoplastic Dispersions, Rheol. Acta, 26, 186 (1988)

24   G.C. Martin, A.V. Tungare and J.T. Gotro, Modeling the Chemorheology of Thermosetting Resins During Processing, Pol. Eng. Sci., 29, 1279 (1989)

25   A.V. Tungare, G.C. Martin and J.T. Gotro, Chemorheological Characterization of Thermoset Cure, Pol. Eng. Sci., 28, 1071 (1989)

26   S.D. Lipschitz and C.W. Macosko, Rheological Changes During a Urethane Network Polymerization, Pol. Eng. Sci., 16, 803 (1976)

27   C.W. Macosko, Rheological Changes During Crosslinking, Brit. Pol., 17, 239 (1985)

28   J.M. Castro and C.W. Macosko, Kinetics and Rheology of Typical Polyurethane Resin Transfer Molding, Proc. ANTEC, 26, 434 (1980)

29   R.L. Frutiger, The effect of Flow on Cavity Surface Temperatures in Thermoset and Thermoplastic Injection Molding, Pol. Eng. Sci.,26, 243 (1986)

30   L.T. Manzione, G.W. Poelzing, R.C. Progelhof, Experimental and Mathematical Treatment of Transfer Pot Temperatures for Thermosets, Pol. Eng. Sci., 28,1056 (1988)

31   S.A. Bidstrup, Structure-Property Relations for Model Epoxy Networks, Ph.D.Thesis, Univ. Minnesota (1986)

32   C.Y.M. Tung and P.J. Dynes, J. Appl. Pol. Sci., 27, 569 (1982)

33   H.H. Winter, Can the Gel Point be Detected by the G'-G" Crossover?, ANTEC, 300 (1987)

34   H.H. Winter and F. Chambon, Analysis of a Crosslinking Polymer at the Gel Point, J. Rheol., 30, 367 (1986)

35   F. Chambon and H.H. Winter, Linear Viscoelasticity at the Gel Point of a Crosslinking PDMS with Imbalanced Stoichiometry, J. Rheol., 31, 683 (1987)

36   D. Harran, A.C. Senhaji and G.Marin, Rheological Study of the Gelation in a Thermosetting Resin, Proc. Xth Int.Congress on Rheology, 1, 300 (1988).

37   J.D. Ferry, Viscoelastic Properties of Polymers, John Wiley & Sons, New York, (1978)

38   A.I. Isayev, Injection and Compression Molding Fundamentals, Marcel Dekker Inc., New York (1987)

39   E. Vos, H.E.H. Meijer and G.W.M. Peters, Multilayer Injection Moulding. Part I: The Piston Driven Flow, Int.Pol.Proc. VI, p42-50 (1991)

40   A. Segal, Sepran Manual (1989)

41   P.J.L. van der Velden, Particle Tracking in Reactieve Stromingen, Internal report Technical University of Eindhoven: WFW91.106 (1991)

42   R.M. Corbey, A Finite Element Analysis of 2D Reactive Flow, Internal report Technical University of Eindhoven: WFW91.015 (1991)

43   C. Cuvelier, A. Segal and A.A. van Steenhoven, Finite Element Methods and Navier-Stokes Equations (1986)

44   F.N. v.d. Vosse, A.A. van Steenhoven, A. Segal and J.D. Jansen, Int. J. Num. Meth. Fluids, 6 (1986)

Appendix I : Plots of Measured Dynamic Viscosities

In this appendix all experiments performed to model the dynamic viscosity are presented *(Table AI)*. Accordingly, for each heating rate plots are given of the measured dynamic viscosities and the powerlaw coefficient as a function of the conversion. For each effective shear rate plots are presented of the dynamic viscosities and the flow activation energy and pre-exponential factor as a function of the conversion.

Table AI: Experiments performed to model the dynamic viscosity.

Heating rate [°C/min]	Frequency [rad/s]	Maximum Strain [%]	Effective Shear Rate [s^{-1}]
2	1	0.25	0.25
2	10	0.25	2.5
2	100	0.25	25
5	1	0.25	0.25
5	10	0.25	2.5
5	100	0.25	25
5	4	0.25	1
5	1	1	1
5	100	1	100
5	50	2	100
5	200	0.5	100
10	1	0.25	0.25
10	10	0.25	2.5
10	100	0.25	25
10	100	1	100
10	50	2	100
20	1	0.25	0.25
20	10	0.25	2.5
20	100	0.25	25
20	100	1	100
20	50	2	100
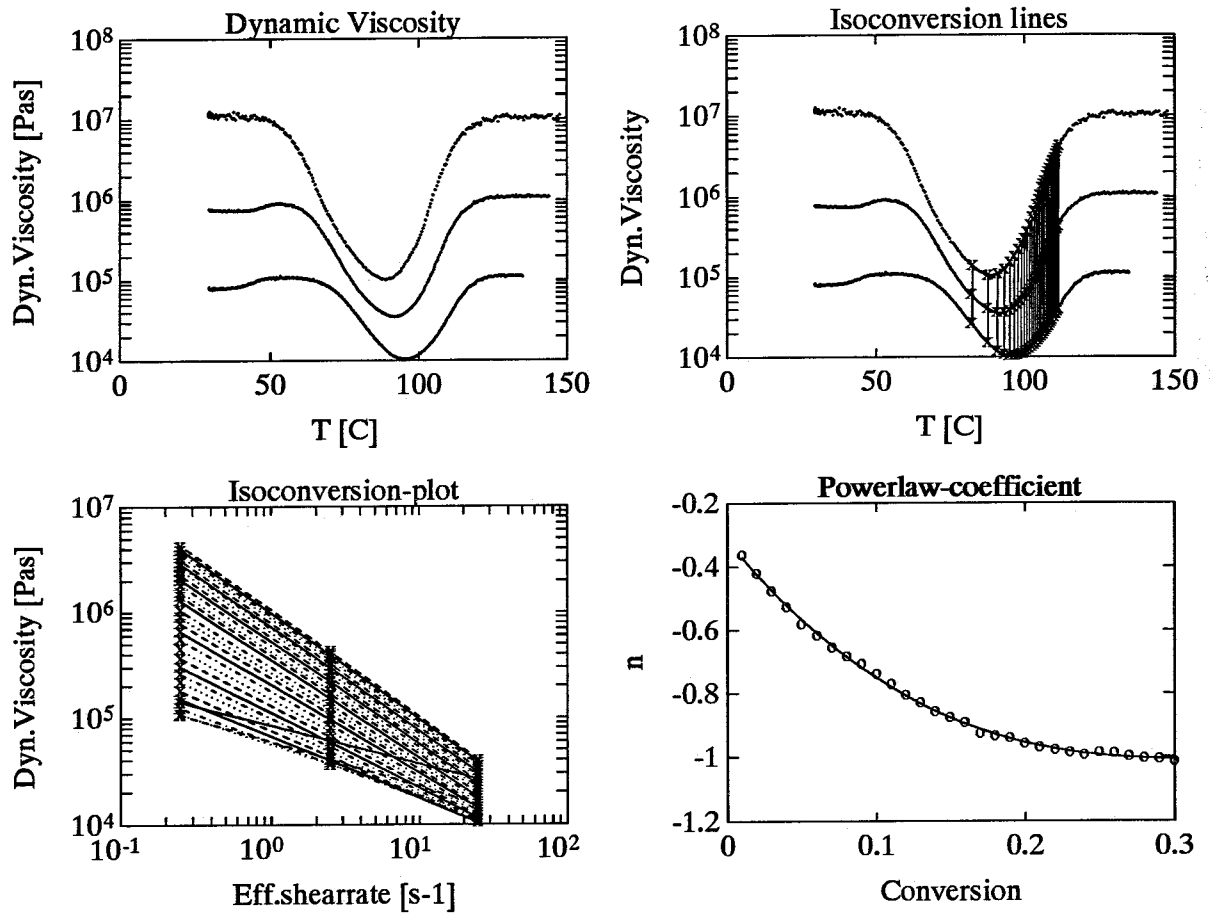
Figure AI.1   Experiments performed at 2 °C/min and various effective shear rates.
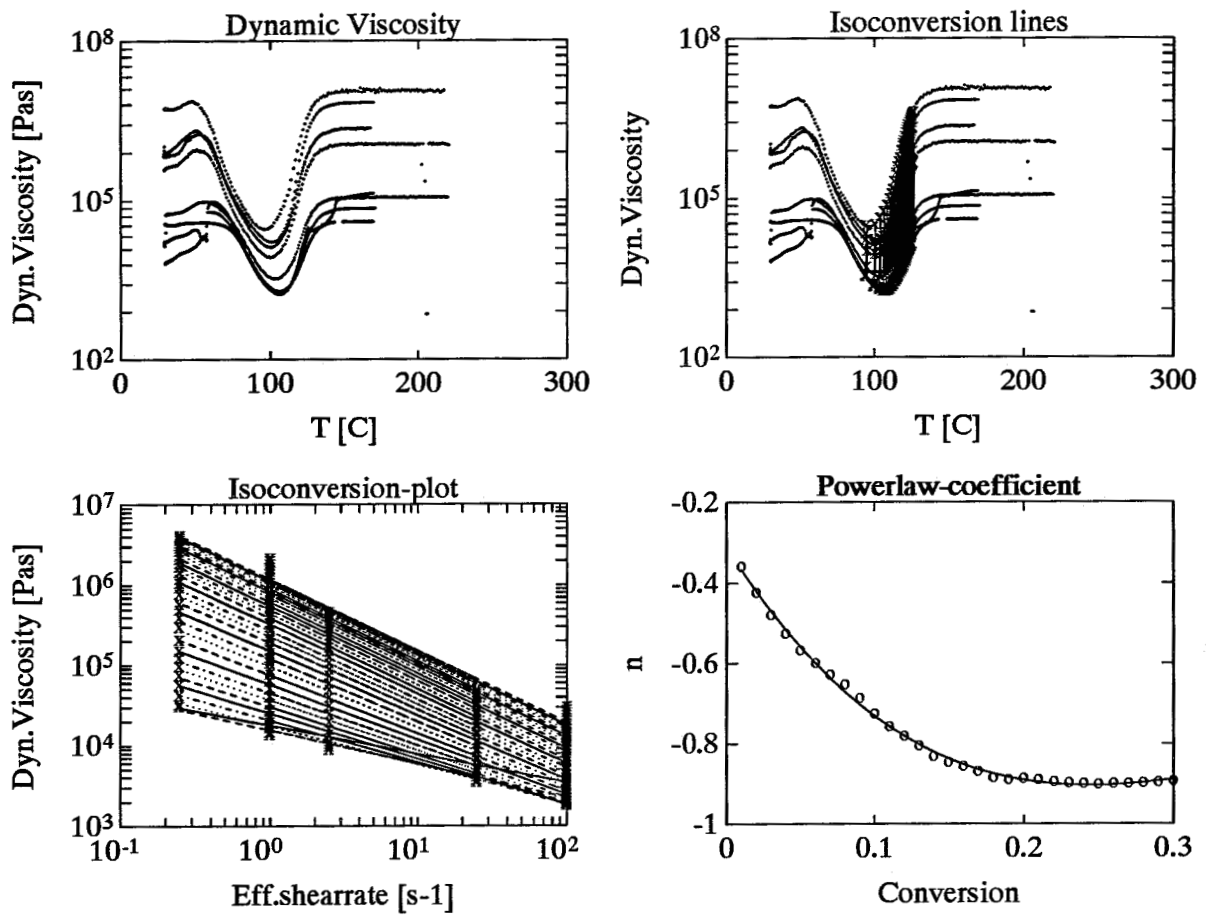
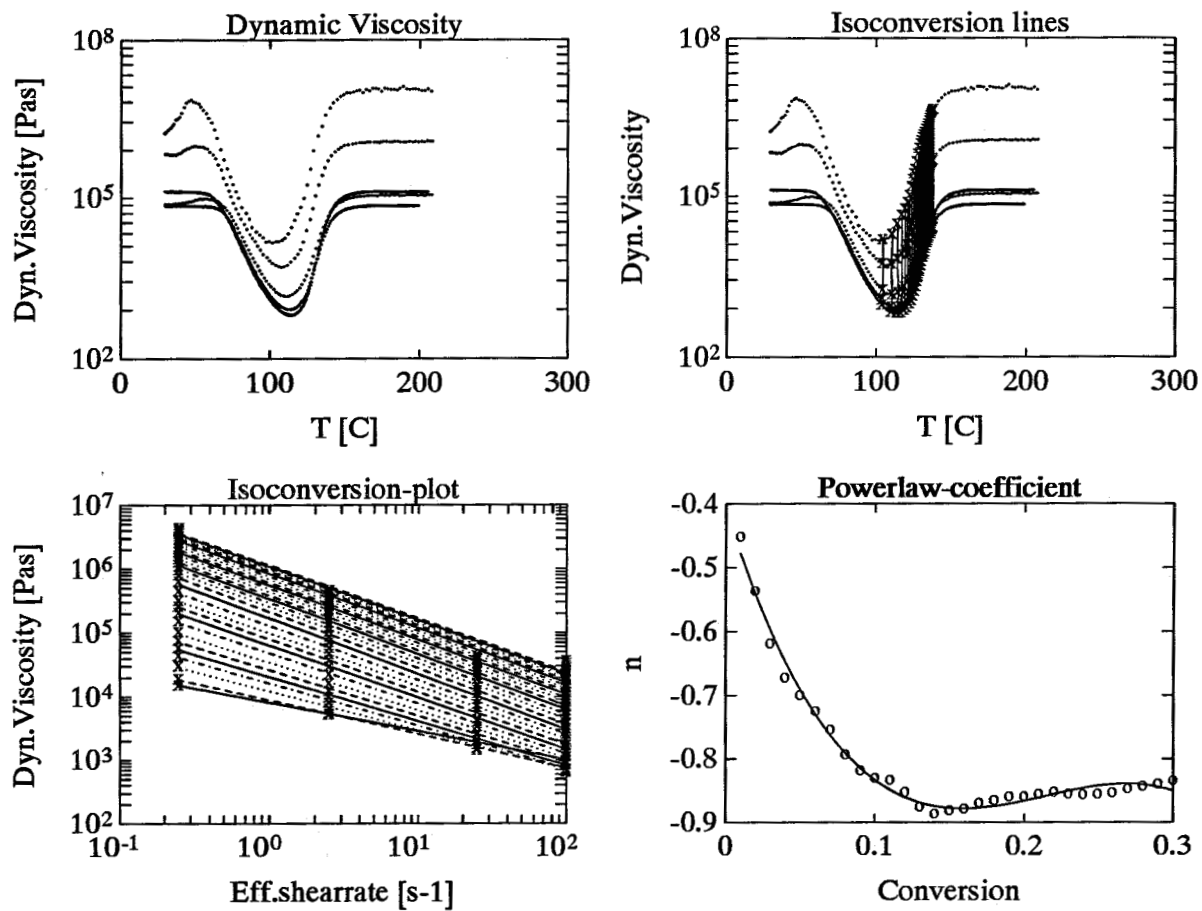Figure AI.2   Experiments performed at 5 °C/min and various effective shear rates.

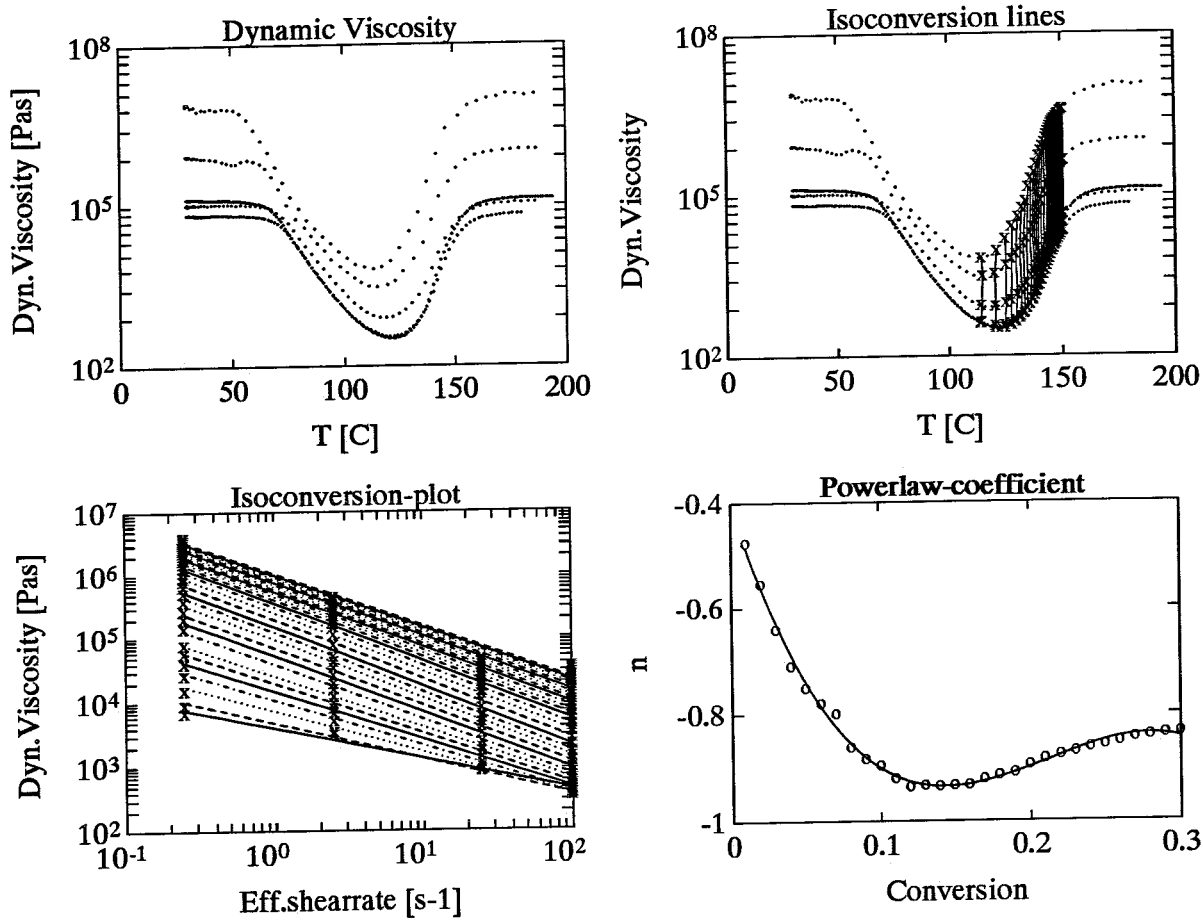Figure AI.3 Experiments performed at 10 °C/min and various effective shear rates.

Figure AI.4 Experiments performed at 20 °C/min and various effective shear rates.
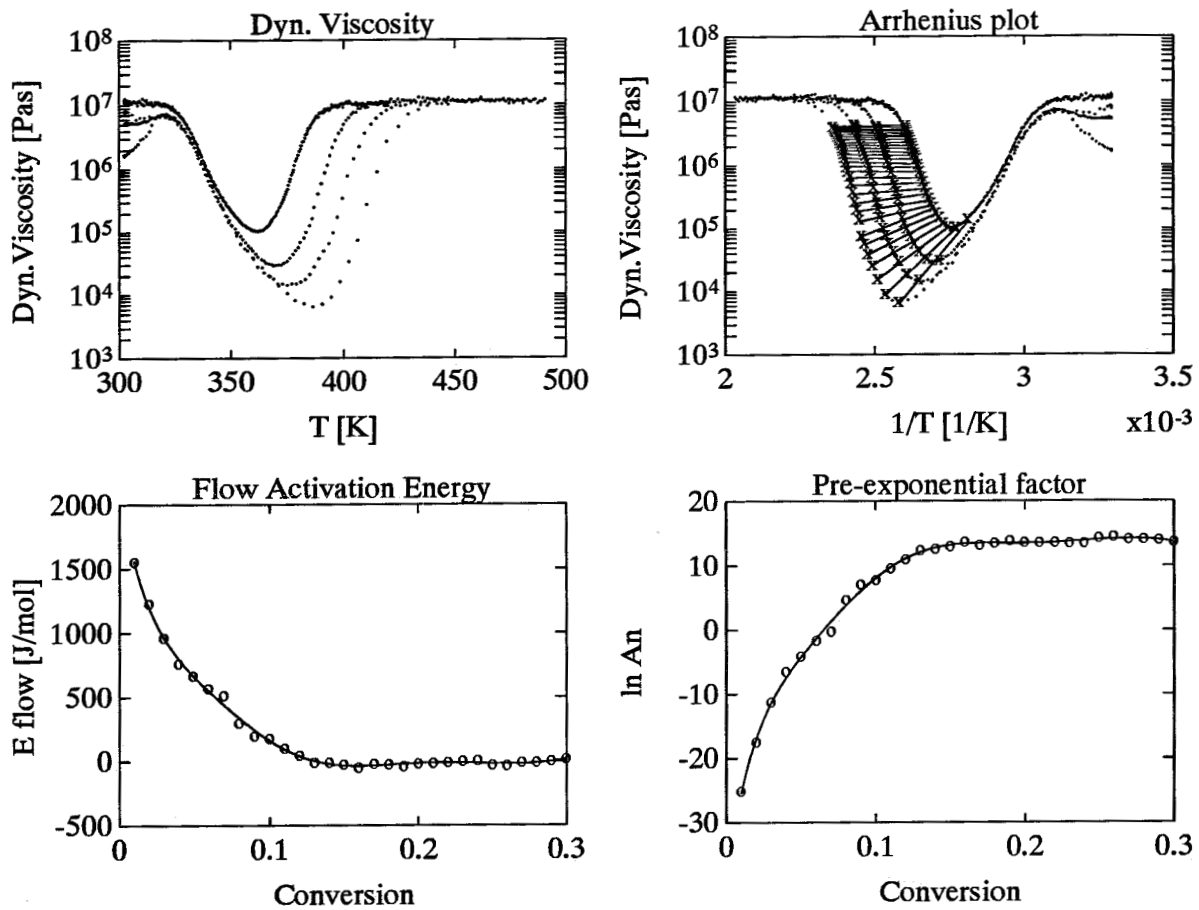
Figure AI.5   Experiments performed at an effective shear rate of 0.25 s^{-1} and heating rates of 2, 5, 10 and 20 °C/min.
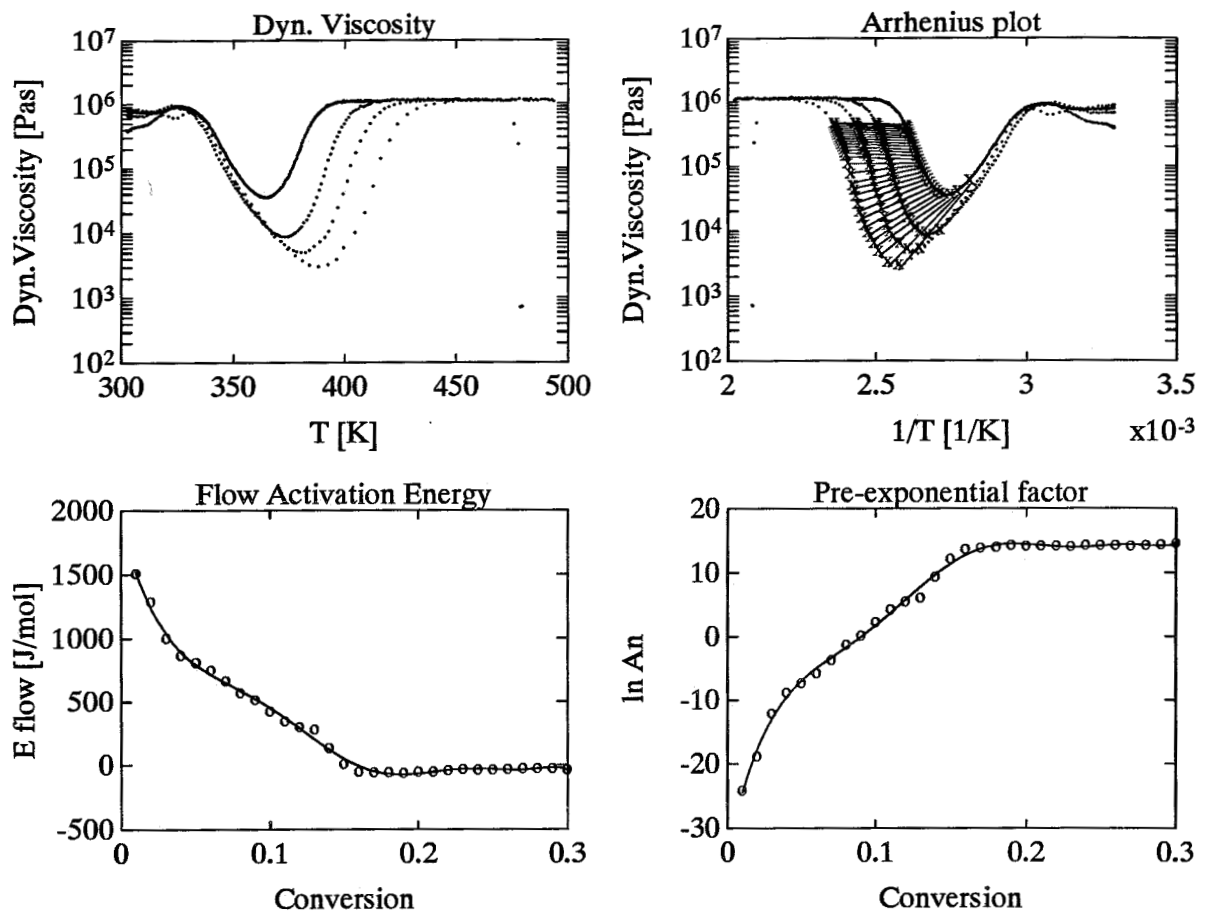
Figure AI.6 Experiments performed at an effective shear rate of 2.5 s^{-1} and heating rates of 2, 5, 10 and 20 °C/min.
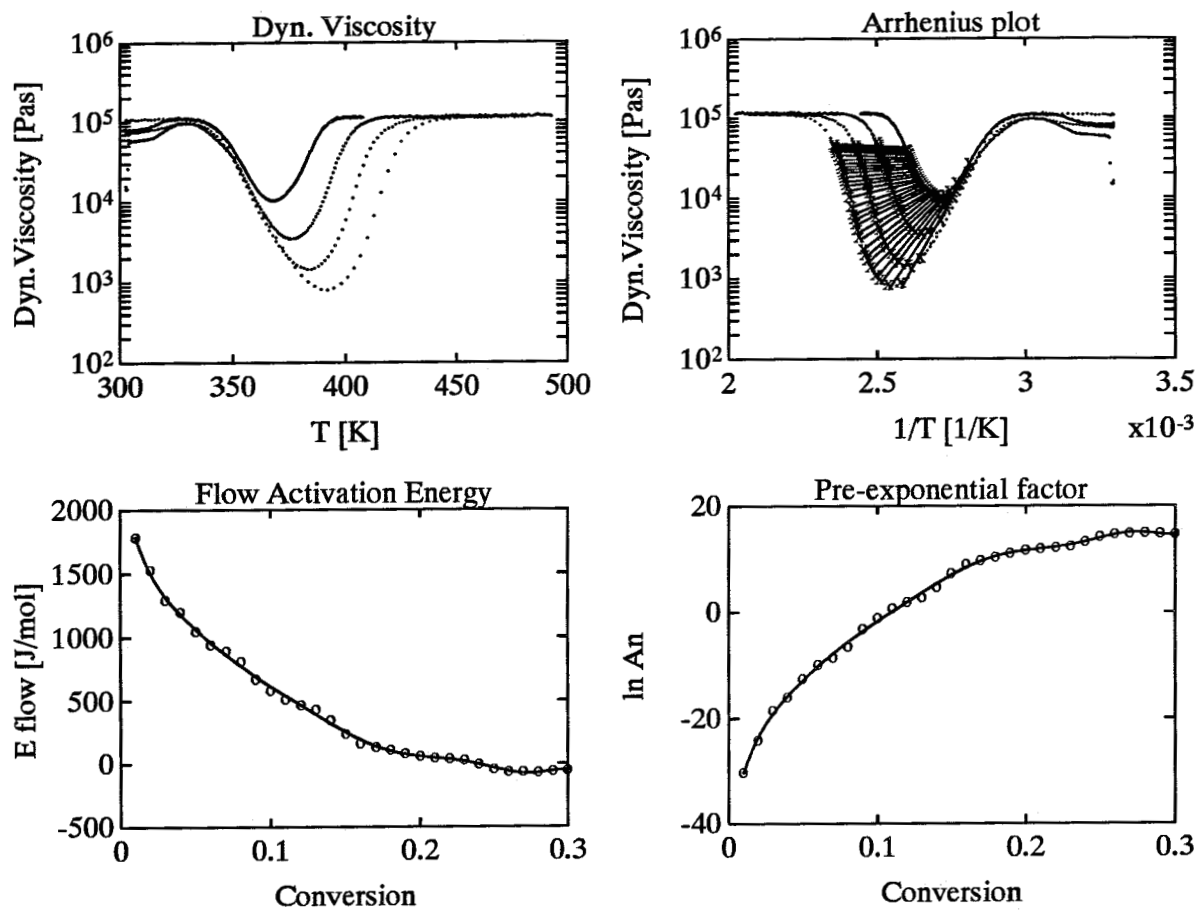
Figure AI.7 Experiments performed at an effective shear rate of 25 s^{-1} and heating rates of 2, 5, 10 and 20 °C/min.
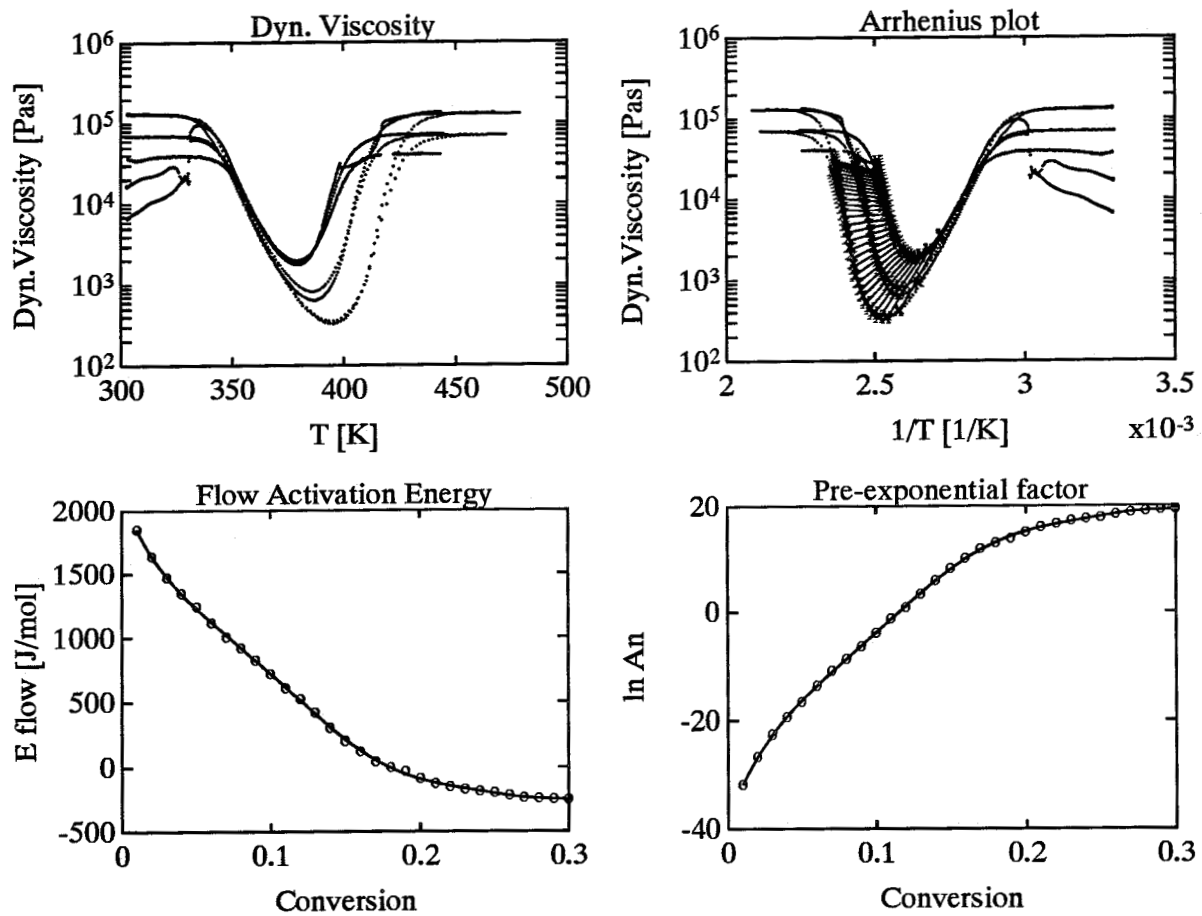
Figure AI.8 Experiments performed at an effective shear rate of 100 s⁻¹ and heating rates of 5, 10 and 20 °C/min.

Appendix II : Parameter Values of the Viscosity Model

Viscosity Model:

$$\eta(\alpha, T, \dot{\gamma}) = \eta_0(\alpha) * e^{\frac{E_\eta(\alpha)}{RT}} * \dot{\gamma}^{\,n(\alpha)}$$

The parameters $E_\eta(\alpha)$, $\ln \eta_0(\alpha)$ and $n(\alpha)$ are described by polynomials with the coefficient presented in *Table AII*.

$$P(\alpha) = c_0 + c_1\alpha + c_2\alpha^2 + c_3\alpha^3 + c_4\alpha^4 + c_5\alpha^5 + c_6\alpha^6 + c_7\alpha^7 + c_8\alpha^8 + c_9\alpha^9$$

Table AII: Coefficients of polynomial fits on the parameters $E_\eta(\alpha)$, $\ln \eta_0(\alpha)$ and $n(\alpha)$ in the viscosity model.

coefficients	E_η	$\ln \eta_0$	n
c_9	-2.8944736e+11	7.7970068e+08	0
c_8	3.85088790e+11	-1.0439793e+09	0
c_7	-2.1489223e+11	5.8797321e+08	0
c_6	6.6218237e+10	-1.8352803e+08	0
c_5	-1.2642624e+10	3.5610406e+07	0
c_4	1.6141442e+09	-4.6181142e+06	0
c_3	-1.4453929e+08	4.1683219e+05	-4.2140983e+01
c_2	9.0527915e+06	-2.6059090e+04	3.0273505e+01
c_1	-4.2472636e+05	1.2246353e+03	-7.1070750e+00
c_0	1.7367610e+04	-3.7808040e+01	-3.5431100e-01

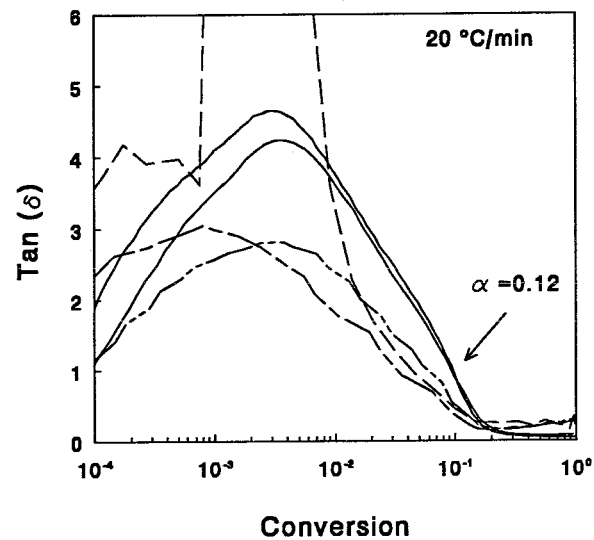# Appendix III : Plots of Tan (δ) versus conversion
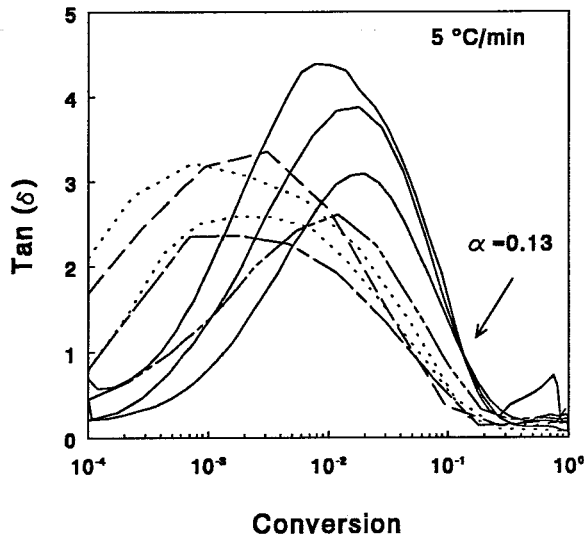
Figure AIII.1   Tan (δ) plotted against conversion; heating rate of 5°C/min, various effective shear rates: 0.25(--), 1(..), 2.5(-.), 25(-..), 100(-).
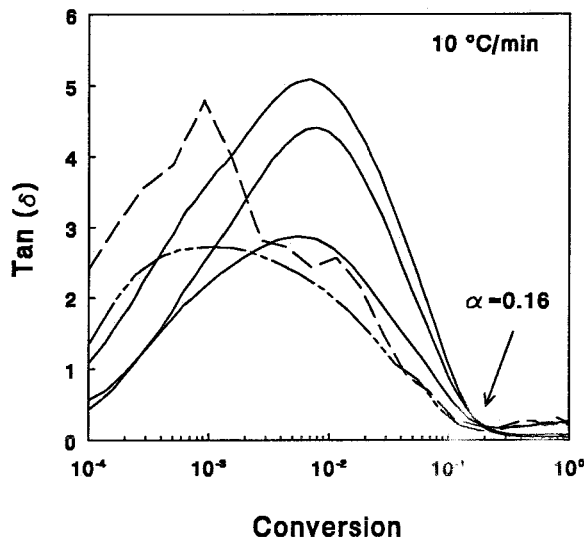
Figure AIII.2   Tan (δ) plotted against conversion; heating rate of 5°C/min, various effective shear rates: 0.25(--), 2.5(-.), 25(-..), 100(-).

Figure AIII.3   Tan (δ) plotted against conversion; heating rate of 5°C/min, various effective shear rates: 0.25(--), 2.5(-.), 25(-..), 100(-).

Appendix IV   :   Balance Equations

The four balance equation used in the numerical model are reduced[42], using dimensionless numbers:

Energy balance:

$$\rho^* c_{p_0}^* \ Gz \ \dot{T}^* = (\vec{\nabla}\cdot\lambda \ \vec{\nabla}T) + Br \ \eta^* \ II - DaIV\rho^* R^*$$

If the Graetz number >> 1 conduction is dominated by convection. The Brinkman number reflects the ratio of heat produced by viscous dissipation and by heat conduction with respect to the viscosity . The Damköhler IV number indicates the ratio of the reaction heat and conduction.

Mole balance:

$$\frac{dC^*}{dt^*} = \frac{1}{Pe_m} \ (\vec{\nabla}^{*^2} C^*) - DaI \ R^*$$

In the case of a large mass transfer Peclet number the molecular diffusion can be neglected. The Damköhler I number gives the reaction rate to flow rate ratio.

Mass balance:

$$(\vec{\nabla}^* \cdot \vec{v}^*) = \frac{1}{Ga}\alpha^* T^* - \frac{Ca}{Re}\kappa^*\dot{p}^* - \frac{\beta_0}{C_0}\beta^* \dot{X}$$

The reciprocal Gay Lussac number reflects change of volume by temperature change. The ratio between the Cauchy number and the Reynolds number reflects the volume change by pressure change.

Momentum balance:

$$Re \ \rho^* \dot{\vec{v}}^* = 2\vec{\nabla}^* \cdot \eta^* D^{d^*} - \vec{\nabla}^* p^* + \frac{Re}{Fr}\rho^* g^*$$

The Reynolds number gives the ratio of inertia forces to viscous forces. The Froude number gives the ratio of inertia forces to gravity forces. It is reasonable to neglect the gravitational forces and inertia forces, because they are very small compared to pressure and viscous forces.

Dimensionless numbers: estimation

Graetz number	Gz	$= (\rho_0 r_0^2 C_{p0}) / (\lambda_0 t_0)$	10^2
Brinkman number	Br	$= (\eta_0 V^2) / (\Delta T_{op}\lambda_0)$	10^{-2}
Damköhler IV number	DaIV	$= (r_0^2 \rho_0 h_r) / (\Delta T_{op}\lambda_0 t_r)$	0.21
Mass Peclet number	Pe_m	$= (r_0 V) / D$	10^8
Damköhler I number	DaI	$= r_0 / (V t_r)$	0.02
Gay Lussac number	Ga	$= 1 / (\alpha_0 (T_1 - T_0))$	10^7
Cauchy number	Ca	$= \rho_0 V^2 \kappa_0$	10^{-12}
Reynolds number	Re	$= (\rho_0 V r_0) / \eta_0$	10^{-6}
Froude number	Fr	$= V^2 / (g r_0)$	10^{-5}

In view of the piston driven flow simulated the following characteristic values are estimated:

ρ_0	: characteristic density	10^3 [kg/m^3]
r_0	: characteristic radius	10^{-1} [m]
C_{p0}	: characteristic heat capacity	10^3 [J/(kg.K)]
λ_0	: characteristic thermal conductivity	10^{-1} [J/(mKs)]
t_r	: characteristic reaction time	10^3 [s]
η_0	: charateristic viscosity	10^5 [Pa s] at T=393 [K]
V	: characteristic velocity	10^{-3} [m/s]
ΔT_{op}	: difference in temperature of wall and initial melt	100 [K]
h_r	: characteristic heat of reaction	-10^4 [J/kg]
D	: molecular diffusion coeficient	10^{-13} [m^2/s]
α_0	: characteristic volume expansion coefficient	10^{-9} [1/°C]
κ_0	: characteristic isotherm compressibility factor	10^{-9} [m^2/N]

A-13
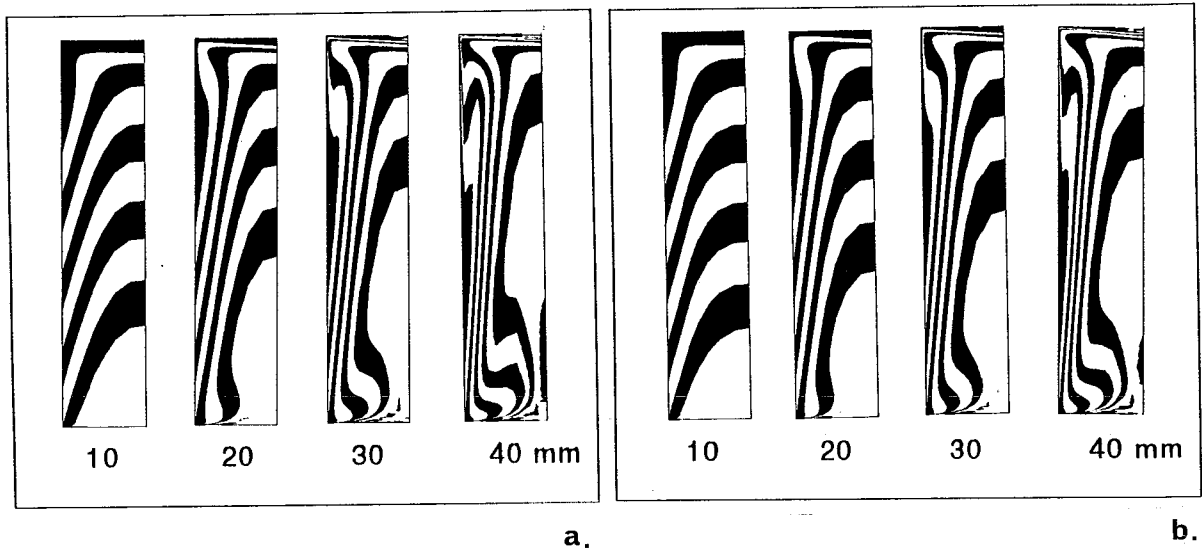
Figure AV.1   Numerical simulations with $T_{wall} = T_{piston} = 100$ °C
a) $t_d = 180$ s. b) $t_d = 300$ s
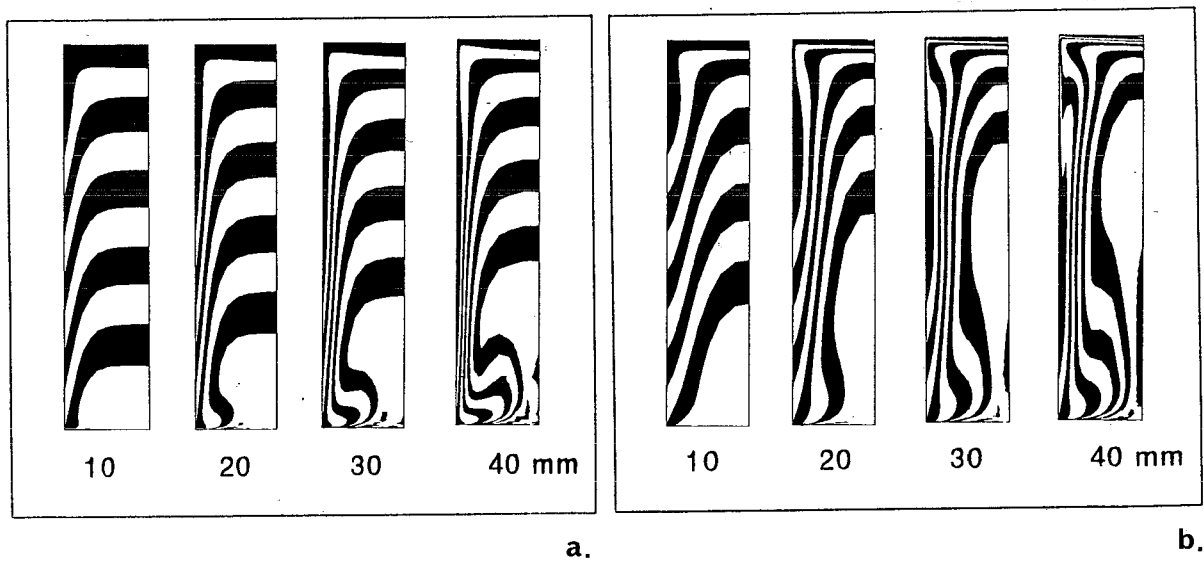
Figure AV.2   Numerical simulations with $c_p = 4c_p$, $T_{wall} = 100$ °C
a) $t_d = 180$ s. b) $t_d = 300$ s
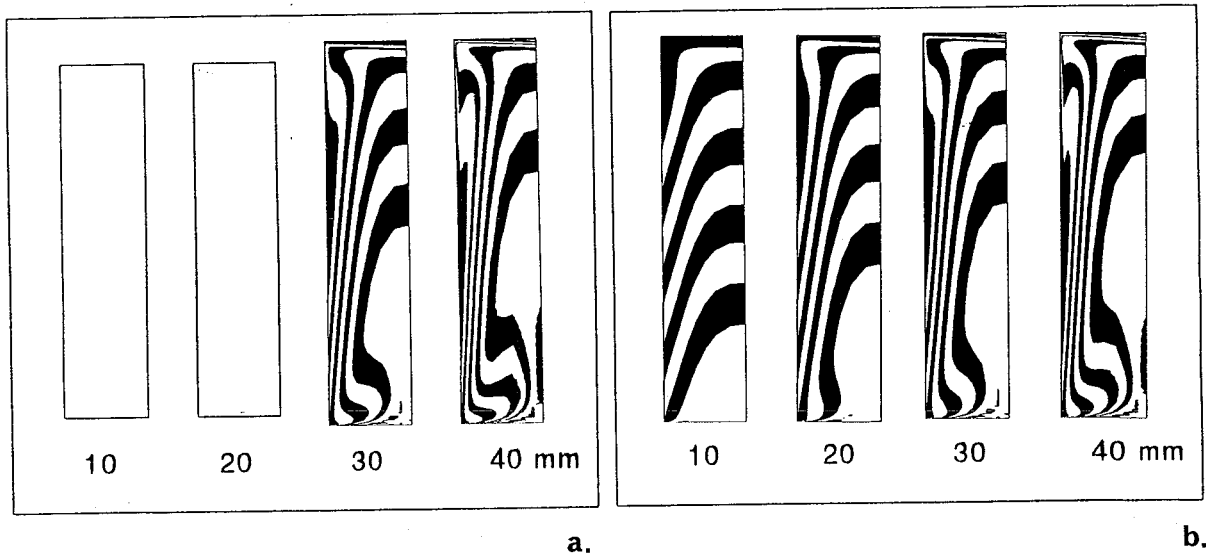
Figure AV.3 Numerical simulations with T_{wall} = 100 °C, t_d = 180 s
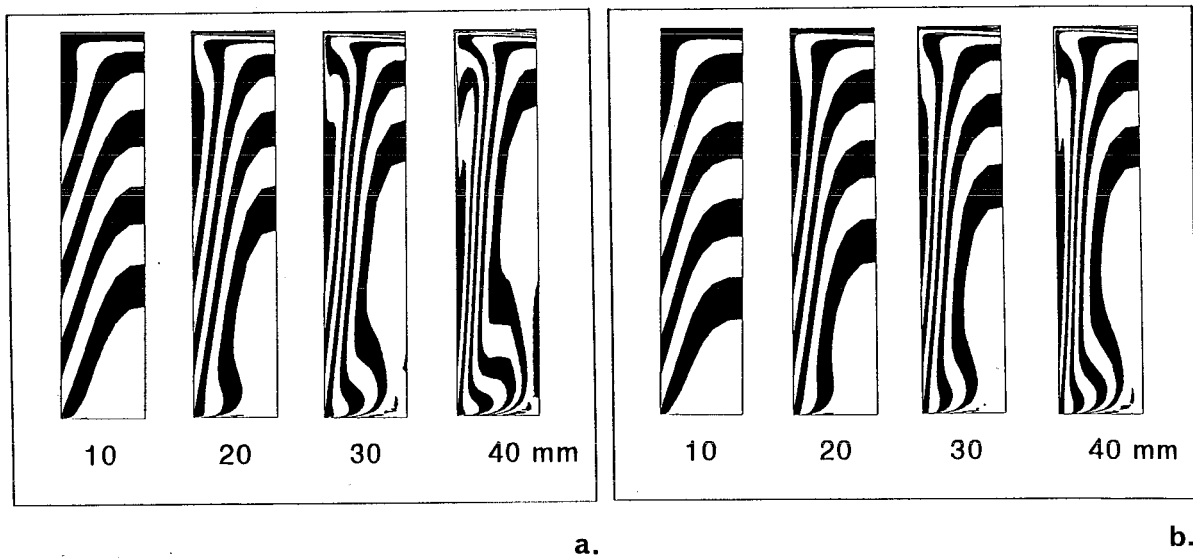
a) c_p = c_p/4. b) Δt = Δt/4

Figure AV.4 Numerical simulations with the viscosity calculated with 2α ;

T_{wall} = 100 °C

a) t_d = 180 s b) t_d = 300 s

A-15
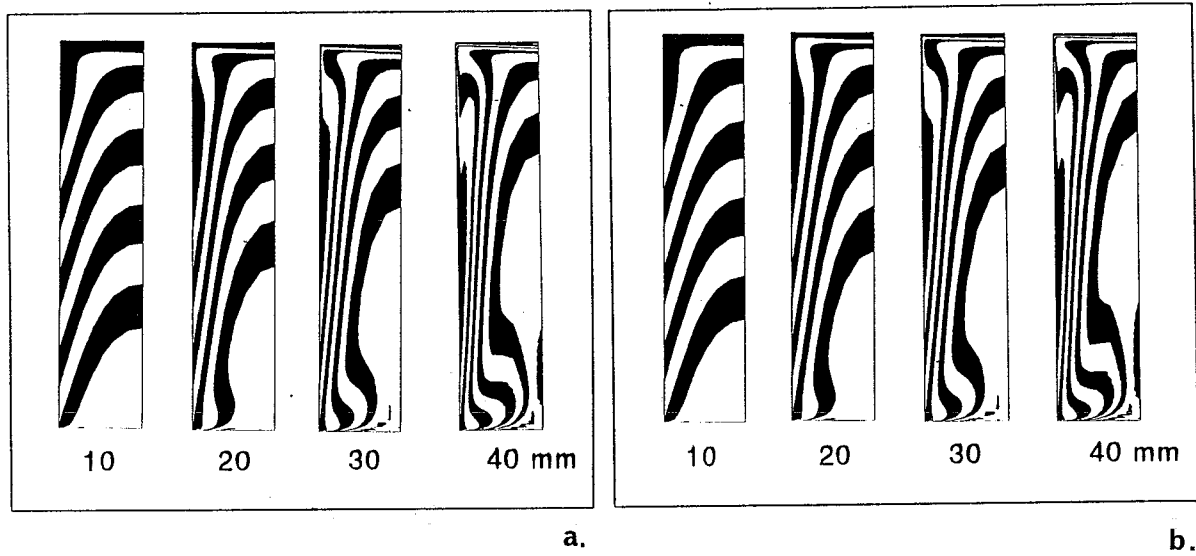
Figure AV.5   Numerical simulations with T_{wall} = 100 °C, t_d = 300 s

a) $\dot{\gamma}_{min}$ = 0.1 s^{-1} b) $\dot{\gamma}_{min}$ = 0.25 s^{-1}
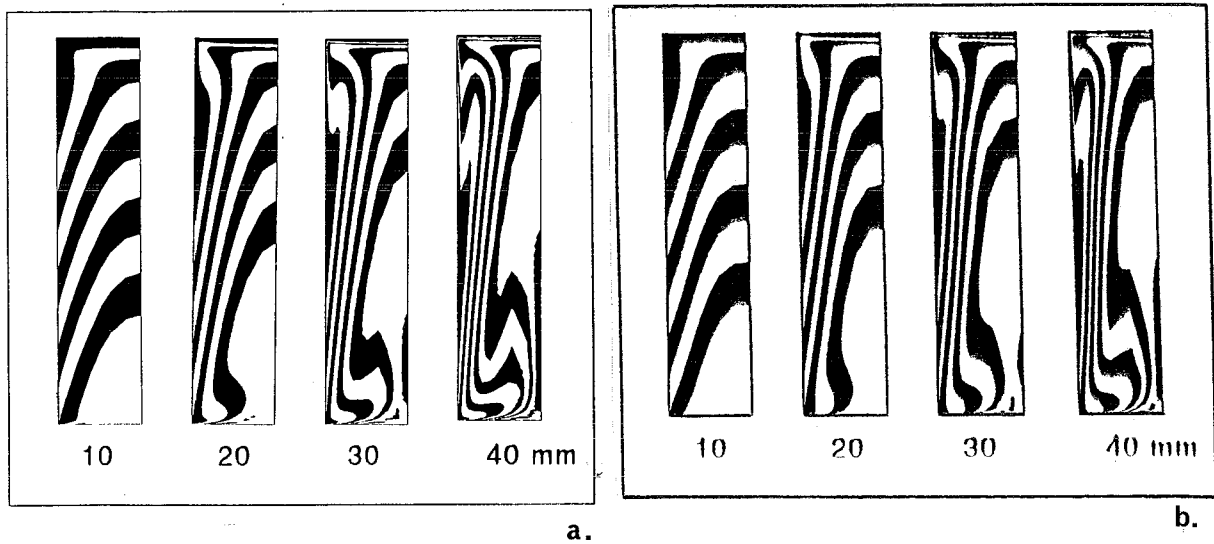
Figure AV.6   Numerical simulations at T_{wall} = 100 °C ;

a) t_d = 300 s; constant viscosity : η = 10^3 Pa.s

b) t_d = 180 s; c_p = 1400 J/kg.K

A-16

Appendix VI : Visualisation Experiments: Two Cavities without a Leadframe

In this Appendix the cross sections (Figure AVI.1) are given for the experiments I to XII (Figure AVI.2). The numbers correspond to those in these figures.
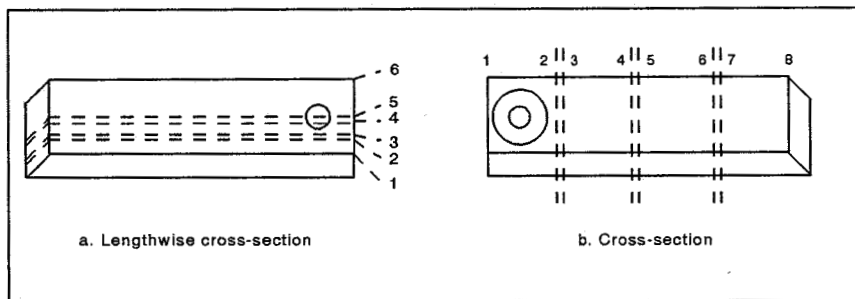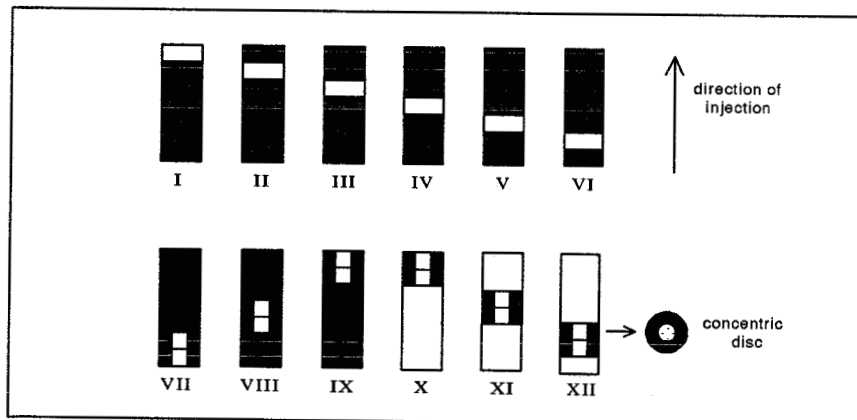

Figure AVI.1   Cross sections.

Figure AVI.2   Composition of the stacks of black and white compound.